Modeling and Control of a Magnetic Drug Delivery System

by

Sepideh Afshar

A thesis
presented to the University of Waterloo
in fulfillment of the
thesis requirement for the degree of
Master of Applied Science
in
Mechanical Engineering

Waterloo, Ontario, Canada, 2012

I hereby declare that I am the sole author of this thesis. This is a true copy of the thesis, including any required final revisions, as accepted by my examiners.

I understand that my thesis may be made electronically available to the public.

Abstract

Therapeutic operation risk has been reduced by the use of micro-robots, allowing highly invasive surgery to be replaced by low invasive surgery (LIS), which provides an effective tool even in previously inaccessible parts of the human body. LIS techniques help delivering drugs effectively via micro-carriers. The micro-carriers are divided into two groups: tethered devices, which are supported by internally supplied propulsion mechanism, and untethered devices. Remote actuation is the critical issue in micro-device navigation, especially through blood vessels. To achieve remote control within the cardiovascular system, magnetic propulsion offers an advantage over other proposed actuation methods.

In the literature, most research has focused on micro-device structural design, while there is a lack of research into design and analysis of combined structure and control. As the main part, integrating the principle of electromagnetic induced force by feedback control design will lead to the desired automatic movement. An actuator configuration should thus first be designed to initiate the desired force. The design is basically defining the type and placement of a set of coils to achieve an operational goal.

In this project, the magnetic actuation is initiated by a combination of four electromagnets and two sets of uniform coils. Preliminary studies on 2D navigation of a ferromagnetic particle are used to show the effect of actuator structure on controller performance. Accordingly, the performance of the four electromagnets combination is compared to the proposed augmented structure with uniform coils. The simulation results show the improved efficiency of the augmented structure. In more general cases, the arrangement and number of electromagnets are unknown and should be defined. An optimization method is suggested to find these variables when the working space is maximized.

Finally, the problem of robust output regulation of the electromagnetic system driven by a linear exosystem, is also addressed in this project. The exosystem is assumed to be neutrally stable with unknown frequencies. The parallel connection of two controllers, a robust stabilizer and an internal model-based controller, is presented to eliminate the output error. In the latter one, an adaptation is used to tune the internal model frequencies such that a steady-state control is produced to maintain the output-zeroing condition. The robust regulation with a local domain of convergence is achieved for a special class of decomposable MIMO nonlinear minimum-phase system. The simulation results show the effectiveness and robustness of this method for the electromagnetic system when two different paths are considered.

Acknowledgements

This work would not have been completed without help and support of many individuals. I would like to thank everyone who has helped me along the way, particularly Dr. Behrad Khamesee and Dr. Amir Khajepour, for providing me with the opportunity to conduct my master's research under their supervision. I am grateful to all the people who helped me in my research, especially Dr. Christopher Nielsen for his valuable suggestions. Furthermore I appreciate the love, patience, and support of my family and my parents, especially my husband, Mehrdad.

Table of Contents

List of Figures

List of Notations

$\boldsymbol{M}$	The magnetization vector
$\boldsymbol{B}$	The magnetic field vector
$\boldsymbol{R}$	The MRI scanner duty cycle
$\boldsymbol{F_{magnetic}}$	The magnetic force vector
$\boldsymbol{A}$	The magnetic vector field
μ_0	The free space permeability
$\boldsymbol{i}$	The volume current
I	The current per unit length
N	The number of coil' turns
L	The length of coil
a_1	The inner radius of each coil
a_m	The mean radius of each coil
a_2	The outer radius of each coil
μ	The magnetic permeability
χ	The magnetic susceptibility
$\boldsymbol{H}$	The magnetic field density
$\boldsymbol{i_m}$	The current surface density
$\boldsymbol{i_{ms}}$	The current volume density
$\boldsymbol{X}$	The position representation in Cartesian coordinates
$\boldsymbol{\rho}$	The position representation in Cylindrical coordinates
C_D	The drag coefficient
U	The relative velocity of particle to the fluid velocity
Re	The Reynolds number

ρ_m	The particle density
ρ_f	The fluid density
$\boldsymbol{Z}^*$	The zeroing submanifold

Chapter 1
Introduction

The evolution of micro-robotics has brought substantial risk reduction to interventional therapeutic operations. The replacement of highly invasive surgery with low invasive surgery (LIS), which is an outcome of robotic technology, provides effective tools in previously inaccessible parts of the human body. For instance, LIS makes digestive tract therapies and endovascular operations much easier. To accomplish the former, a wide range of capsule robots with various propulsion mechanisms have been designed, with the contact forces between the tract tissue and the capsule robot playing an important role in their design procedure. However, in the latter case (i.e., endovascular operations), the robots are focused more on self-propulsion capabilities as a carrier device. In fact, the synergy of carrier and blood flow is prominent when mechanical contact is replaced by fluidic interactions. The carriers are divided into two major groups: tethered devices and untethered devices. While the tethered devices are supported by an internally supplied propulsion mechanism, untethered devices have been mainly developed according to three different designs: magnetic beads pulling, biomimetic flagellated robots, and magnetotactic bacteria [1]. Since the magnetic force is not strong enough to pull the nano/micro-sized particles, augmenting nano/micro-navigators with swimming capability in blood vessels is inspired by naturally alive nano-swimmers.

In practice, the remote actuation is a critical issue in micro-device navigation through the human body, especially while traveling in blood vessels. Indeed, magnetic propulsion offers an advantage over other proposed actuation method. Although various electromagnetic actuators have been designed for required applications, the Magnetic Resonance Imaging (MRI) device is utilized in most research activities. Compared to other apparatuses, MRI systems are widely available in clinics and are ideal platforms for providing enhanced soft tissue imaging. They also initiate magnetic gradients in three directions. In this context, imaging and actuation capability commanded by user interfaces are the main characteristics of MRI platforms [2]; nonetheless, assigning simultaneous tracking and actuation commands is inaccessible. Thereafter, a software protocol has been introduced to eliminate this complication.

Magnetic actuation may also be accomplished by different arrangements of coils and electromagnets (in this paper, we refer to a coil as insulated wires wrapped around a non-ferromagnetic core or an air-core while an electromagnet uses a ferromagnetic core) to produce electromagnetic stimulation via field shaping. Due to pulsatile blood flow, controlling a device in the human cardiovascular system is quite challenging. The environmental complexity necessitates a proper time setting in the controller architecture to sustain stable controller and guarantee real-time operation. In addition, the appropriately applied magnetic gradient at each time step, which differs among micro-robot designs, will improve navigation efficiency. In the literature, most of the efforts have been directed towards micro-device structural design; thus, more studies are needed into automatic navigation. In fact, since the magnitude and sign of the magnetic gradient over the working space is defined by the actuator design, it may vanish at some area, and the optimal design of actuator is required. Combining the principle of magnetic induced force by feedback control design produces

the desired performance inside the blood vessels.

The possibility of controlling micro-carriers for medical applications has roots in 1965, when aneurysm embolization studies were being carried out. Other applications were also being considered, such as magnetic drug delivery using magnetic carriers. These methods rely strongly on either external magnets or magnetized needles and catheters; however, as the employed magnet cannot be implanted close to the target spot such as the tumoral lesion, targeting efficiency is reduced. Moreover, the deeper the targets are located in the human body, the greater the targeting efficiency is required. Targeting efficiency is reduced further when the release site is being left toward the tumor spot. Because of the actual reach limitations of catheterization, efficiency reduction can be quite vital in most cases [3]. In order to overcome this problem, externally computerized magnetic actuation of micro-device to follow a predefined path to the target area has been introduced.

As mentioned previously, MRI scanners are widely employed to achieve magnetic remote actuation. Nevertheless, most efforts are directed towards the verification of MRI scanners to be applicable in real-time actuation. PID controllers are the most frequently used controller employed to close the control loop. In fact, PID gain scheduling for nonlinear systems is acquired by trial and error. More studies have been conducted to consider nonlinearity of the system in which a magnetic field model is considered to some extent, such as particle movement control by a set of electromagnets. However, nonlinear controllers specially designed and used for 2D stimulation still encounter some limitations. Thus, a new platform composed of an electromagnetic actuator and control unit is required to improve navigation performance while eliminating the previous controllers' drawbacks.

The actuator structure affects the control efficiency applied to a magnetic particle in the domain of interest. A configuration composed of different electromagnets and coils located with appropriate orientation is studied in this research. The designed configuration has to provide any assigned forces on a magnetic particle traveling inside the working space. With respect to this fact, each configuration admits a working space where the particle can be driven in any direction. An optimized structure should initiate the maximum possible working space. Afterwards, a dynamical model of the moving magnetic particle in the working space stimulated by electromagnets is required to optimize the structure and design a controller. First, the magnetic field of each electromagnet is studied separately to investigate the efficient design for electromagnets orientation and location in the final structure. Then, the working space produced by the combination of electromagnets has to be optimized. At this level, any magnetic force vector needs to be supported by the electromagnets. In the meantime, it is assumed that the field of electromagnets can be summed up to calculate the total magnetic field. The assumption of superposition is shown to be reasonable within the experimental measurement in the case where currents to the electromagnets are limited.

Indeed, the representation of the traveling object dynamical model in the actuator working space is of great importance as long as it defines the controller design procedure. In this project, the state space representation is extracted for the proposed actuator configuration. The introduced model is proved to be controllable under some mild conditions which can be easily checked. In fact, the area where the controllability and observability conditions are satisfied is also defined by the coils arrangement. In order to expand this area, a new structure is proposed that adds a uniform magnetic field vector to the dynamical model. In this case, preliminary studies are done to test the capability of

the initially offered actuator in controlling the magnetic particle. The primary structure is composed of four horizontal electromagnets and two uniform coils; subsequently, the optimal control suggested by Arash Komaee and his group, [35, 38], is applied for the augmented structure. The simulation results depict an efficient satisfaction of the concerned conditions. In addition, the reduction in input current value is observed, which is critical when neither the superconducting electromagnets are utilized nor the structure scale is limited.

The main purpose of this project is to move a ferromagnetic particle along a predefined path in a fluidic environment. This problem can be broken down into two parts: the actuator design and the control design. A robust output regulation control composed of the parallel connection of two controllers, a robust stabilizer and an internal model-based controller, is presented to eliminate the output error. This method is the extension of the semiglobla output regulation method proposed in [42] for a special class of nonlinear single-input single-output (SISO) systems. The simulation results indicate a precise path following with a constant velocity while the current vector is remained bounded.

This report is organized as follows. In Chapter 2, a brief literature review on previous work is presented, showing how the drawbacks of current methods necessitate a new design. Preliminary studies on control design of the produced stimulation by a potential actuator structure are done in Chapter 3, followed by the optimization of the actuator configuration and new actuator design in Chapter 4. The output regulation problem is addressed in Chapter 5. Finally, conclusion and suggestions for future work are presented in Chapter 6.

Chapter 2
Literature Review

Replacing highly invasive surgeries by minimally invasive surgeries (MIS) has been at the forefront of modern medicine research [1]. The first efforts on MIS were commenced when the 1966 science fiction movie "Fantastic Voyage" released. While these early 'fantastical' medical interventions resulted in a variety of therapies and diagnostic methods, these methods are challenging when the operative sites were inaccessible or high risk. In recent years, MIS methods have substantially improved and are now applicable in both blood vessels and digestive tract therapies. The main idea is to conduct a micro-robot within the digestive tract or blood vessel along a pre-defined path, either to deliver a drug or apply the therapies at the target spot. Therefore, the micro-robots lay in different categories and have mission-adjusted structures to sustain the required performance.

2.1 Capsule robots

Capsule robots are the carriers designed to be implemented in large scale MIS applications. For instance, a capsule Micro-Electromechanical System is applied to diagnose gastrointestinal diseases. In addition, several endoscopic capsules are improved to reach areas inaccessible by hand-operated tools. The M2A pill called a capsule robot (which was an early disposable design 26 mm in length, and 11 mm in diameter, and with a weight of 3.7 grams) was introduced and passed experimental tests from 2000 to 2004 [2]. The idea of a capsule robot able to take pictures inside the small bowel traces back to the 1980s. However, due to high power consumption of charged couple device (CCD) image sensors, these robots seemed to be inapplicable. In the early 1990s, complementary metal oxide semiconductor (CMOS) technology introducted the Wireless Capsule Endoscopy (WCE) improvement.

Recently, the given diagnostic platform is composed of the PillCam SB, a data recorder, the RAPID_R 3 software and also a workstation to implement the test procedure. The next version of PillCam is PillCam ESO. Both PillCam versions cause some side effects, like GI obstruction, strictures, or fistulas, swallowing disorders and cardiac pacemakers. In October 2005, studies on removing the potential disorders led to a disposable pill offered for small bowel endoscopy by Olympus Corporation.

Active capsule robots actuated by magnetic field were introduced by Mosse et al. in 2001, Sendoh et al. in 2003, and Woo et al. and Swain et al. in 2005. Olympus extended the capsule design towards the self-propelled capsule, and the robot was given the added capability of being externally controlled by an external magnetic field. In the sense of externally been powered, the Norika Project Team offered WCE, an externally powered capsule attached to a CCD image sensor [3]. In general, the complete medical platform was equipped with proper actuators for active locomotion, sensors for diagnosis and therapy, and tools to employ MIS inside the digestive tract [2].

Thereafter, active locomotion control methods were improved, such as the controller suggested in [13]. A system proposed by Stereotaxis (Stereotaxis, Inc., St. Louis, USA) was used to drive the catheter tip orientation. The system, composed of two permanent magnets attached to a controllable robotic arm and a magnet on either side of the patient table, is the same approach studied in [14]. The M2A was chosen to pass an experimental test by the Niobe magnetic navigation system developed by Stereotaxis. This actuation provided the robot maneuverability in frictional contact between the capsule and GI tissue, which is considered and modeled in [15, 16]. The experimental results show the feasibility of robotic actuation when a uniform magnetic field is shaped by a robotic arm in both cases.

Legged capsule robots were also suggested, to add an active locomotion feature to the endoscopy capsules. The peculiar movement of such a micro-robot inside a tubular, deformable and slippery substrate is considered in [4] for the first time. Achieving contact with the tissue and displacing the contact points are necessary to initiate and transmit the locomotive forces. A type of legged capsule robot was also introduced by Sukho Park et al. and passed experimental tests in 2006 [5].

In addition, rotational movement of a spiral capsule is another alternative to producing controllable locomotion. In this case, an externally generated rotational magnetic field plays an important role as a part of the locomotion actuator. The control mechanism proposed in [6] contains two magnet bars embedded into the spiral surface of a spiral-type capsule robot stimulated by a circumferential magnet array. The designed and fabricated capsule is tested experimentally through a pig intestine when it is outside of the body. Furthermore, the active locomotion sensing of a spiral capsule robot is proposed in [11], and the calculated position is utilized to control a spiral type capsule in [12].

The capsbot, a two-mass endoscopic capsule robot, is yet another capsule robot design first introduced by H. Li and K. Furuta [7]. Namkon Lee et al. presents the development of the test system for the Capsubot, which has been studied theoretically using mathematical model and simulation. The Capsubot consists of two parts: a capsule shell and cylinder mass. By moving the cylinder backward or forward, the outer shell also moves in opposite directions. **T**he active control command is determined through optimizing a cost function. Capsubot tracking control is considered in [8]. It should be noted that capsubot is an underactuated system, as it has one control input, generated by a piezoelectric element, and two degrees of freedom, the shell and inner mass position. There is additional research on the improvement of control strategies for capsbot trajectory control, such as the Iterative Learning Control Scheme utilized in [9] and the sliding mode control suggested in [10].

2.2 Swimming robots

As endoscopic capsules are inappropriate in blood vessel applications, a new category of nano/micro-robots has been introduced to carry out the therapies and diagnosis tasks in inaccessible parts of the body and through the blood veins. In blood flow, swimming micro-robots are efficient self-propelled agents. Magnetically controlled swimming micro-robots feature non/micro-scale navigation while providing high reliability and safety. Tao Mei et al. are among the first researchers to advance the development of swimming micro-robots [17]. In their design, a pair of ferromagnetic

polymer fins mounted on a boat-shaped plastic body is used as the propulsion micro-actuator. Accordingly, the robot navigation is tested while generating an alternating magnetic field by a wounded solenoid around the robot working place. The fin-type swimming micro-robot has also been suggested by Shuxiang Guo et al. [18].

In the context bio-inspired propulsion, Breder introduced swimming movements into body and/or caudal fin (BCF) locomotion and median and/or paired fin (MPF) locomotion [19]. With respect to the low Reynolds number in medical application, the BCF movement was followed by a fin-type micro-robot in [20]. The main purpose of this research was to resolve the drawback of the known swimming micro-robots which provide efficient swimming only in one direction. Mathematical modeling and experiment reveal that installing two Giant magnetostrictive thin films with different second order natural is an efficient way to produce a bidirectional swimming movement.

Observation of bacterial navigation via the spirochaeta and flagella brought about a swimming micro-robot consisting of a helix-type head and an elastic tail [21]. The spiral head drives the elastic tail when the rotational magnetic field is fired. The prevalence of this spiral design over the capsule-like body with flagellum proposed in [22, 23] involves replacing a stepper motor with an external rotational magnetic field. The bifurcation phenomenon, which occurs when the driving torque increases, plays an important role in the movement process. The point where bifurcation occurs is proved to be a function of geometrical and material properties. It is shown that the linear and angular velocity increase linearly by exerted torque.

2.3 Nano-particles

To date, employing the magnetizable nano-particles as drug carriers is one of the most popular applied methods, with biological polymers, liposomes, hydrogels, viruses, etc., being used to achieve this aim. These vehicles release therapeutic agents under the influence of ultrasonic, PH, temperature, or chemical interaction. The magnetic nano-particles are guided toward the target area by a magnetic field which is often produced by superconductor coils mounted outside the body.

Several methods have been applied to increase the efficiency of magnetic particle drug delivery, since the externally generated magnetic field applies relatively small and insufficient local forces on micron and submicron sized particles. Moreover, a single source cannot simultaneously maximize both the particle magnetizing field and the field gradient in all space. Making use of either implanted magnetic stent or magnetic anchors to produce local gradient helps trap the magnetic seeded drug at the desired location. In addition, nano-tubes and nano-discs are suggested to originate efficient magnetic forces.

2.4 Nano/Micro-carriers

Controlled drug delivery with accurate targeting and precise speed of drug release is critical to optimizing the effects of a drug. In other words, the drug's side effects as well as its stability during

the delivery process need to be considered in the controller design procedure [24]. In most of the research, the micro carrier is modeled by a homogeneous spherical to study the automated navigation of micro carriers. The reported mathematical model includes magnetic force and drag force applied by the blood flow. Being much smaller than the drag force, the micro device weight and buoyancy can be neglected in small blood vessels [25]. Now that MRI scanners generate both magnetic actuation and imaging modality, it has become the most commonly used platform to initiate a displacement force on a ferromagnetic core. The technique in which an MRI scanner provides magnetic force is referred to as magnetic resonance propulsion, or MRP.

In order to actuate untethered micro- or nano-robots without the need for propulsion external hardware, self-propulsion is still offered. For instance, Drexler has suggested an artificial molecular propelling mechanism. Nano-motors already exist in nature and have been studied by many researchers who mimic their propulsion mechanism. Bell et al. present the idea of artificial flagellum in the form of nano-coils stimulated by applying a rotating magnetic field. Nonetheless, the technological constraints, especially for embedding a power source, make this configuration contingent on external propulsion hardware. Martel et al. proposed a novel strategy in 2005 in which the combination of Magnetotactic Bacteria, MTB, and their molecular motors is suggested as a means of bio-actuation for nano-robots. Magnetically driven MTB can propel a load in blood flow with various forms, from nano/micro-particles to larger objects. Loading magnetic MTB was also implemented by the Martel group for the first time [26]; nonetheless, the orientation control of the naturally inspired micro-robot is completed by its core model.

2.5 Navigation control

According to the literature, applied controllers that navigate the carrier to the target area are mostly designed by a PID controller approach employed on an MRI scanner. When an MRI scanner is used as the external actuator, the propulsion and tracking events should be appropriately integrated by controlling software. On this subject, the proposed control software deals with the commands time sequencing as well as the real-time, physiological and technological constraints. The MRI scanner control software architecture is made of synchronization, propulsion phase and tracking acquisition events [34]. The feasibility of control architecture with a synchronization event lasting for 0.6 ms, and propulsion phase and tracking acquisition events for lasting 41 ms is investigated for in vivo navigation. The experiment is arranged by a ferromagnetic 1.5 mm chrome steel sphere with magnetization $M_{1.5\,T} = 1.35 \times 10^{-6}\ A/m$. [27,28].

Clinical MRI systems provide 3D magnetic gradient in the order of mT/m magnitude for imaging purposes, which are also usable for producing a magnetic force. The induced force to move an untethered particle in the scope of MRI scanner can be depicted as below [25]:

$$\boldsymbol{F_{magnetic}} = RV_{ferro}(\boldsymbol{M}.\nabla)\boldsymbol{B} \qquad 2\text{-}1$$

where $\boldsymbol{F_{magnetic}}$ is the magnetic force (N), $\boldsymbol{M}$ is the magnetization of the material (A/m), V_{ferro} is the volume of the ferromagnetic body, and $\boldsymbol{B}$ is the magnetic field (T). The term R is the duty cycle

representing the time during which the magnetic gradients are applied in each cycle. When considering the limitations in boosting magnetic force amplitude, magnetic materials with strong magnetization are required for a strong induced force; therefore, ferromagnetic materials are good options. Their magnetic saturation value, where no more magnetization occurs, is also higher than other materials. Typically, 1.5 T valued magnetic fields induced in most clinical MRI systems are strong enough to saturate a ferromagnetic core.

The nature of real-time propulsion and control constraints arising due to an MRI structure is studied in [29] using step response of the system closed by a discrete PID controller. Here, the micro-device moves in a physically constrained environment, where the blood vessel size varies and the pulsatile behavior of blood flow must be taken into account. MRI-actuated feedback control strategy involves some limitations. The feasibility of 2D real-time control of path tracking in the xz-plane using a simple PID controller is investigated in [30], where the pre-planned path is divided into rectilinear segments traveled by a particle core. In fact, a polar coordinate system is used to run the navigation along line segments applying discrete PID controller. The experimental results show that the particle attains the target point along an x direction before a z direction. The DC magnetic field oriented along the z axis causes particle rolls along the x-axis and slides along the z-axis; thus, the friction force is much higher along the z-axis than the x-axis.

The application of a PID controller in real-time navigation of a magnetic bead along a pre-defined path via the clinical MRI system is improved in [31]. Unlike in previous methods, environmental boundary effects such as frictional forces and blood pulsatile flow are specifically taken into account more. The experiment with steady flow is repeated in a 2D environment at the first step, followed by a 1D pulsatile flow experiment. The experimental results indicate that the particle is likely to show conspicuous oscillation in 2D navigation along the path with intermediate waypoints. The problem is claimed to arise due to the large delay time as well as the operation of a main normal PD controller. It can be also detected that a particle meets significant drift along the x-axis when it leaves the first waypoint for the next target. As the authors suggest, the much higher friction coefficient along the z-axis relative to the x-axis leads this phenomenon. Additionally, instabilities and important oscillations around the equilibrium points are detectable from experimental results when the blood stream is modeled as a pulsatile flow. It is also indicated that there is a lack of robustness to noise and un-modeled dynamics.

The MRI-based computerized platform is also proposed to manipulate magnetic micro-device carriers in a 3D volume by integrating the same PID controller into the closed-loop navigation system [34]. A 2D experiment is set to apply the controlled navigation under quiescent flow within an MR human carotid replica. The flow rate changes from 6 to 11 cm/s by a mechanical pump and a valve controlled by a flow meter device. In addition to the limitation on minimum control delay, the results show that the controller is not robust to environmental noise.

In order to improve the performance of navigation control, a nonlinear controller respecting the system mathematical model is presented in [32]. At this stage, the system uncertainties are handled more efficiently, since there is analytical design of both controller and observer. A backstepping feedback design combined with a high gain observer ensures stability along the controlled trajectory.

Like the previous methods, the particle is bound to move in 2D space within an xz-plane. The simulation includes 1D trajectory tracking within a tube along the x-axis with known wave form of flow, and 2D Y-shaped reference trajectory wherein uncertainties are added. Simulation results show good operation in position tracking, yet the velocity tracking does not meet the performance of position tracking. An optimal control method is suggested in [34] to navigate a ferromagnetic particle actuated by a set of four horizontal electromagnets. Like previous simulations and experiments, the ferromagnetic particle is assumed to move in a 2D plane along a predefined path. By assuming the position to be precisely measurable, a quadratic algebraic equation has to be solved to obtain input currents. Experimental results show good tracking of the desired trajectory while the actual trajectory has relative time lag.

To overcome the raised drawbacks, a nonlinear controller scheme is introduced wherein more studies are conducted to consider system nonlinearity. A proposed back-stepping controller that uses a Lyapunov stabilizing function resolves some of the problems, especially when the particle is navigating through pulsatile flow. This approach shows better simulation results as well as robustness to environmental noise and system uncertainty. Nonetheless, the nonlinearity of the magnetic field is disregarded and the magnetic field gradient is taken to be an input control command. Above all, the magnetization direction is assumed to have no effect on magnetic force direction. The ordered arrangement of electromagnets is also proposed to control the particle trajectory. In this case, the utilized controller divides the system into series cascade form. Nonlinearity of the dynamical system comes before the linear part respectively, making the controller design easier. The experimental test of protocol performance reveals good results when the precise position of the particle is known. However, complete knowledge of the particle's position is not available while it is travelling within the human body. This drawback, enhanced by entered measurement noise, makes the method in appropriate in medical applications.

A complete actuator structure was proposed by R. G. McNail and his group in [39] and constructed by three perpendicular coaxial pairs of cylindrical electromagnet. This instrument is called the Magnetic Stereotaxis System. The magnetic field and gradient within the working space induced by the electromagnets are studied in the next papers by the same group [40], and the mathematical model of an implanted permanent magnet under three different movement conditions is defined in [41]. Similarly, the control commands of the electromagnets are calculated using the extracted model when a cost function is aimed to be minimized. Mathematical calculations show the requirement of large currents in the case of antiparallel alignment for the magnetization vector and the induced force vector.

As stated, a protocol taking into account the analytical optimization and modeling of magnetic actuator is required, to be then followed by the final controller design. Although an analytical study on magnetic actuation was accomplished by A. Komaee and his group [34, 38], it has to be modified to be applicable for either 3D path following or trajectory tracking. Moreover, this approach relies on numerical calculations, increasing the time delay, which is an important issue in magnetic actuation. In addition, the actuator structure should be evolved, since in most of the previous applications, large currents are necessary. The improper structure leads to inefficient path following, even if the current

values are not limited. As a result, both the actuator configuration and the applied controller have to be considered.

In general, the aim of this project is to navigate a micro-device along a predefined path in a fluidic environment by magnetic field actuation. From the outset, designing a magnetic actuator to eliminate previous actuator shortcomings is a chief goal. To achieve this end, the analytical analysis of produced magnetic fields is required to evaluate the controllability of the whole system in working space. The evaluated results will then help improving the actuator design by maximizing the working space while minimizing the input currents. In the next step, the induced force on the moving micro-device is calculated, provided that the micro-device is assumed to be a ferromagnetic particle. In the modeling course, the applicability of super position law is also assumed reasonable. The validity of this assumption is proved by some experiments when the currents are limited (Appendix). Eventually, the controller design will be considered to provide good navigation performance in the existence of disturbance and uncertainties.

In practice, the automatic navigation can be performed by two different approaches: the path following control and the trajectory tracking control. These control methods are discriminated with respect to the assigned timing rule. In other words, the path following controller is addressed when no timing rule is regarded for the defined path, while the trajectory tracking controller deals with a timed path. Set stabilization theory, and sliding mode control are two methods employed to solve the path following problem. Besides, the sliding mode control can also be used for tracking applications as well as the regulation methods. However, the regulation methods offer the advantage of continuity over the sliding mode scheme. Let assume that the ferromagnetic particle is supposed to follow a specific path with a constant velocity; thus, the automatic navigation is converted to a trajectory tracking problem.

2.6 Output Regulation control

The problem of asymptotically tracking (rejecting) a desired trajectory (unwanted disturbances), is one of the challenging concept in control theory. In fact, the problem of tracking a reference signal is called servo problem while forcing the system output to converge to zero is called regulation problem. Since the servo problem can be interpreted as regulating the output to track the reference signal, it is categorized as regulation problems. It is often assumed that, a dynamical system generates the reference and/or the disturbance signal which must be tracked and/or rejected called exosystem. For linear multivariable systems, this problem was introduced by Davison, Francis, Wonham in [43-45]; the geometric approach was addressed to construct the regulator control. In Francis and Wonham's work, the regulator solving the regulation problem via error feedback controller is shown to incorporate a model of the exosystem which is commonly known as the internal model principle [46]. According to this principle, the output regulation property is robust to the variation of the plant parameter if the controller integrates a suitably reduplicated model of the dynamic structure of the exogenous signals in the error feedback [52].

Afterwards, the nonlinear extension has been considered by several authors. Hepburn and Wonham extended the internal model theory to a class of nonlinear systems defined on differentiable manifolds [47]. Then the conditions for the existence of regulators were investigated by Anantharam and Desoer in the case of constant reference signals [48]. An extension of the introduced conditions by Francis for linear systems in [44, 46] was presented by lie and Rugh to the constant reference signals or slowly time varying signals [49]. This extension is applied by linearizing the system around the operating points. Later on, the results were extended to the general case in which the exosystem generates time-varying reference signals, including the periodic signals by Isidori and Byrnes [50].

In fact, Isidori and Byrnes introduced a class of nonlinear equations to achieve a locally defined manifold annihilating the tracking error which is rendered invariant by a certain control feedback. It was shown that if the plant is exponentially stabilizable, the solvability of the state feedback regulator problem is provided by the solvability of these equations as long as the reference signals are bounded and non-convergent to zero. They also demonstrated that the existence conditions are the special properties of the zero dynamics of a composite system, the combination of the plant dynamics and the exosystem dynamics [50]. This analysis is based on the center manifold theory developed by Kokotovic.

More details on solving an output regulation problem were presented by Byrnes et.al for a nonlinear system whose reference signals are generated by an exosystem [51]. In this work, the control signal is designed to incorporate the constructed internal model of the exosystem and is an integration of two parallel connected components, the servocompensator and the stabilizing compensator. While the former component generates the control signal needed to impose the prescribed asymptotic tracking (rejecting), the latter one stabilizes the final closed loop system. Moreover, the robust regulation problem in the presence of parametric uncertainties ranging within a compact set is addressed.

In general, the problem of output regulation in the presence of unknown modeling parts is solved depending on the dominant type of uncertainty. For instance, if the reference signals to be followed or rejected are defined, but the parameters of the plant mathematical model are varying within a certain tolerance bounds, the “certainty equivalence principle” is employed to design the feedback control law. An online adaptation is used to update the parameters of the control law with a fixed structure. Moreover, if the plant uncertainties also include neglected dynamics, the robustness to uncertainties is successfully achieved using an improved adaptive scheme.

On the other hand, the reference signals might be unknown. In this case, the control strategy must reconstruct this information which is usually done via the internal model principle. This problem is well known for linear systems since a long time and for nonlinear systems, dates back about ten years. The reference signals are assumed to belong to a specified class of functions; respectively, asymptotic tracking is successfully achieved when the feedback mechanism incorporates a device to replicate the information about the reference signal. The recently designed internal model-based controller just deal with the amplitude and phase uncertainties of the exogenous signals. In this context, any mismatch between the frequency of the internal-model and the frequency of the exogenous signals results in a nonzero steady-state error.

The problem of designing an internal-model based control in which the natural frequencies of the internal model are automatically tuned to match a totally unknown exosystem is presented in this report. The proposed control scheme successfully addresses the locally asymptotic tracking/rejecting any family of exogenous signals generated by some neutrally stable dynamical system for a specific class nonlinear systems. This scheme provides asymptotic tracking when the reference signal is not known but can be expressed as the function of a finite number of sinusoidal functions with different frequencies; furthermore, the exosystem is assumed to be a linear dynamical system generating the sinusoidal functions. This method is introduced by A. Serrani et. al. for the single-input single-output (SISO) finite dimensional nonlinear systems [42] and is extended to multi-input multi-output systems (MIMO).

Chapter 3
Planar Steering of a Ferromagnetic Particle: Modeling

As previously illustrated, an actuator made of several electromagnets offers some advantages over an MRI scanner in micro-device navigation inside the body. A general prototype of a potential magnetic actuator, shown in Figure 3-1, is composed of several electromagnets with various alignments and positions. After deciding on the actuator's structure and components, one can formulate the micro-device dynamical equation. With the electromagnet being the basic component of the magnetic actuator, its magnetic field should be mathematically defined, and the micro-device dynamical model is simply established. In fact, the state space representation is mostly used in the modern control theory as the system model, which is applied in this project. It should be mentioned that a navigation control assigns the micro-device's position, not its body axis direction; thus, the device is modeled by a ferromagnetic core from this point onwards. Finally, a primitive planar control of the particle motion is studied in this chapter to pave the way for developing the actuator design.

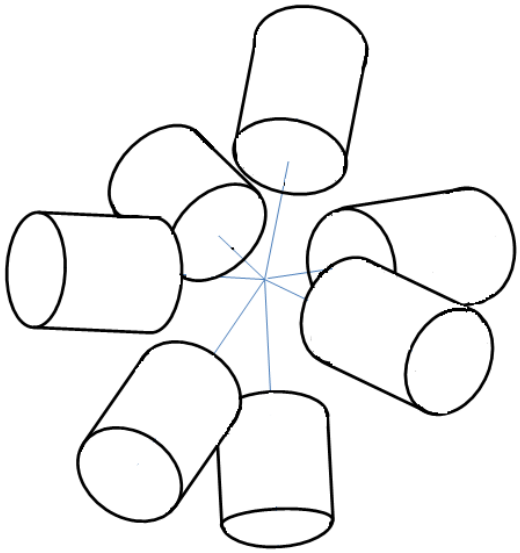

Figure 3-1: Scheme of a potential magnetic actuator made of multi-directional coils and electromagnets

3.1 The magnetic field calculation of an electromagnet

In the presence of soft magnetic material, determining the magnetic induction is reduced in order to solve an electromagnetism problem in vacuum when two types of currents exist. These two current types are: the real source current, and the current associated with the magnetized material. The latter current type is divided into surface current and volume current. In practice, the analytical calculation of a magnetic field mostly deals with a challenging integration, which is the concern of some research in this area. On this matter, numerical methods are mainly introduced to estimate the integration. The Simpson's method is an example of numerical solutions applied in a three-dimensional field

calculation [57]. Specifically, elliptical integral is introduced to determine the magnetic field of a current loop, which is the basic element of an electromagnet.

The elliptical integral uses Toroidal coordinates instead of Cartesian coordinates, and bears the simplified and well-known Elliptical integration, proposed in [58]. The idea of an elliptical integral is extended to calculate the magnetic field produced by a solenoid in [59, 60]. In this paper, a combination of analytical and numerical methods is introduced to estimate the integral value. Whereas the former approach uses the scalar potential to find the field, the latter one benefits from the vector potential concept to achieve this aim. More mathematical details on scalar potential calculation can be found in [61-64]. In order to eliminate the integration part from magnetic field equations, the multipole theory is proposed in [65, 66] to find the external magnetic field from circular cylindrical magnetic systems. It is specifically used to calculate the magnetic field from a cylindrical magnetic source in [67] and replaces the magnetic sources with point magnetic charges in cylindrical coordinates.

A magnetic field by a solenoid can also be found analytically. They are both based on a scalar potential calculation to define the magnetic field vector exterior to a cylindrical source [69] after first finding the vector potential [36, 60]. Since the analytical details are not within the scope of this project, the introduced papers can proide more information. Here, the method suggested in [36] is used to calculate the magnetic field analytically.

3.1.1 The magnetic field calculation of a coil

From this point onwards, the cylindrical coordinate will be used to calculate the field in a z-positive half space with respect to the axial symmetry of the coil. It should be mentioned that the model is given for a non-cored coil. The general way of calculating a magnetic field in the presence of the current volume density (which is one of the magnetic field sources) is calculating a vector called a vector field. A vector field may be calculated using the equation given below [37]:

$$\boldsymbol{A} = \frac{\mu_0}{4\pi} \iiint \frac{\boldsymbol{i}}{r}\, dv \qquad 3\text{-}1$$

where $\boldsymbol{A}$ is the vector potential, μ_0 is the permeability of free space, $\boldsymbol{i}$ is volume current density, and $\boldsymbol{r}$ is the vector from the current element to every desired point in space. For a current loop of radius a carrying current I , which is located parallel to the plane xy (Figure 3-2), the vector potential is calculated using the Biot-Savart law, as below:

$$\boldsymbol{A}(\boldsymbol{X}) = \frac{\mu_0 I}{4\pi} \oint \frac{d\acute{\boldsymbol{l}}}{\left|\boldsymbol{X} - \acute{\boldsymbol{X}}\right|} \qquad 3\text{-}2$$

where μ_0 is the permeability of free space and $d\acute{\boldsymbol{l}} = a d\emptyset \hat{e}_{\emptyset}$. $\hat{e}_{\emptyset}$ is unit vector oriented in the direction of positive polar angle rotation. $\boldsymbol{X}$ is the position vector of an arbitrary point where the field is aimed, and $\boldsymbol{X'}$ is the current carrying element location. The series expansion of $\left|\boldsymbol{X} - \acute{\boldsymbol{X}}\right|$ in terms of Bessel functions is used to simplify the integration. Because of the symmetry, the magnitude of vector

potential is independent of polar angle. The x-component of the vector potential vanishes if $\emptyset = 0$ and $\hat{e}_y = \hat{e}_\emptyset$ are substituted due to the fact that changing the angle would not change the result. The vector potential becomes:

$$\boldsymbol{A}(\rho, z) = \frac{\mu_0 Ia}{2} \hat{e}_y \int_0^\infty dk J_1(k\rho) J_1(ka) e^{-k|z-\acute{z}|} \quad 3\text{-}3$$

Equation 3-3 can be written in the form of $\boldsymbol{A} = A_\emptyset \hat{e}_\emptyset$, in which:

$$A_\emptyset(\rho, z) = \frac{\mu_0 Ia}{2} \int_0^\infty dk J_1(k\rho) J_1(ka) e^{-k|z-\acute{z}|} \quad 3\text{-}4$$

Afterwards, the vector potential of a cylindrical coil can be derived by making use of Equation (3-4) and the superposition principle. If the thickness of a wired cylinder in the radial direction is much less than the mean radius of the coil, it can be modeled by a cylindrical surface current $K = K\hat{e}_\emptyset$ where:

$$K = \frac{\Delta I}{\Delta \acute{z}} = \frac{NI}{L} \quad 3\text{-}5$$

where *N* is the number of turns and *L* is the coil length. Finally, the super position principle is applied and the entire coil vector potential is obtained as $\Delta z \to 0$. The final vector potential becomes:

$$A_\emptyset(\rho, z) = \frac{\mu_0 aNI}{2L} \int_0^\infty dk k^{-1} J_1(k\rho) J_1(ka) f(k; z) \quad 3\text{-}6$$

$$f(k; z) = \begin{cases} e^{-k(z-L)} - e^{-kz} & z \geq L \\ 2 - e^{-k(L-z)} - e^{-kz} & 0 \leq z < L \end{cases} \quad 3\text{-}7$$

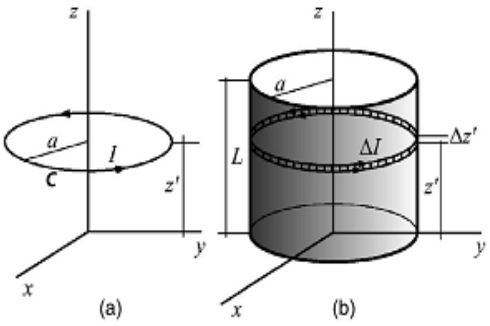

Figure 3-2: Geometry of (a) current loop and (b) cylindrical current [36].

The magnetic field is calculated using vector potential according to the equations below:

$$\boldsymbol{B} = \boldsymbol{\nabla} \times \boldsymbol{A} \quad 3\text{-}8$$

$$B_\rho = -\frac{\partial A_\emptyset}{\partial z} = \frac{\mu_0 aNI}{2L}\int_0^\infty dk\left(e^{-k|z-L|} - e^{-kz}\right)J_1(k\rho)J_1(ka) \quad 3\text{-}9$$

$$B_z = \frac{A_\emptyset}{\rho} + \frac{\partial A_\emptyset}{\partial \rho} = \frac{\mu_0 aNI}{2L}\int_0^\infty dk J_0(k\rho)J_1(ka)f(k;z) \quad 3\text{-}10$$

By assuming $B_\infty = \frac{\mu_0 NI}{L}$ and completing integration (for more details see [36]), one can write the magnetic field in the form of:

$$\boldsymbol{B} = B_\infty \boldsymbol{V}(\rho, z) \quad 3\text{-}11$$

In (3-11), the final magnetic field equation, $\boldsymbol{V}$ is a vector with nonlinear elements and has no dimension. It is possible to simplify the field equations by adding some assumption on the electromagnets' structure or the range of field calculation.

The above equations are derived by assuming that the electromagnet wiring thickness is negligible relative to its radius. In either case, the thickness has to be entered in the magnetic field calculation. To avoid more mathematical complexity caused by radial integration, the electromagnet is replaced by a number of finer ones. Next to the segmentation in radial direction, each new electromagnet contains a ratio of total numbers of turn located at the segment mean radius. The electromagnet and one of its segments are shown in Figure 3-3. The total magnetic field produced by the new structure is calculated below:

$$\boldsymbol{B} = \sum B_{i,\infty}\boldsymbol{V_i}(\rho, z) \quad 3\text{-}12$$

$$B_{i,\infty} = \frac{\mu_0 \acute{N} I}{L} \quad 3\text{-}13$$

where $\acute{N} = \frac{N}{n}$ is each segment's number of turns, n is number of segments, and V_i's are vectors of nonlinear functions.

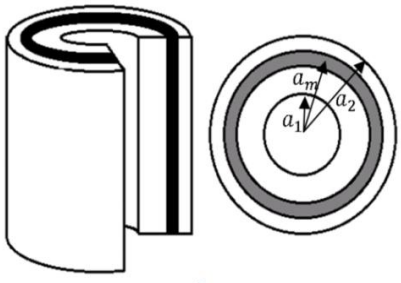

Figure 3-3: Electromagnet segmentation when wiring thickness is not negligible.

Equation (3-12) can be rewritten as:

$$\boldsymbol{B} = B_\infty \overline{\boldsymbol{V}}(\rho, z) \quad 3\text{-}14$$

$$\bar{\boldsymbol{V}}(\rho,z)=\frac{1}{n}\sum \boldsymbol{V_i}(\rho,z) \quad 3\text{-}15$$

Therefore, the magnetic field can be calculated for a single non-cored coil of defined thickness.

3.1.2 The core effect on magnetic field calculation

As mentioned earlier, the previous calculation has been improved for the magnetic field of a non-cored solenoid; however, adding the effect of a core may also enhance the magnetic field's magnitude and gradient. To our knowledge, there are few studies on analytically determining the produced magnetic field. A scalar potential-based approach is suggested in [37], which proposes a numerical magnetic field calculation. In this section, a simple analytical representation for the magnetic field initiated by the soft core magnetization vector is attempted. The magnetization vector, or $\boldsymbol{M}$, is triggered in the existence of a magnetic field. Consider a volume of the magnetic material enclosed by surface S and surrounded by air. The magnetic vector potential can be calculated using the following equation [37]:

$$\boldsymbol{A}=\frac{\mu_0}{4\pi}\iiint\frac{rot\,\boldsymbol{M}}{r}dv-\frac{\mu_0}{4\pi}\iint\frac{\hat{n}\times\boldsymbol{M}}{r}dS \quad 3\text{-}16$$

where $\hat{n}$ is the unit vector to the boundary surface. The magnetization vector is known for every magnetic material as a function of the magnetizing field vector. Moreover, the magnetizing field vector or ampere-turn density vector, $\boldsymbol{H}$, is related to the magnetic field density by a coefficient called the magnetic susceptibility, χ, a property of the magnetic material. In general, this relation is not linear, and the magnetic susceptibility varies by the ampere turn density vector. To simplify further, linearity is considered to be valid when the magnetic material is not saturated. With this assumption, the magnetization vector can be expressed as:

$$\boldsymbol{M}=(\mu-1)\boldsymbol{H}=\chi\boldsymbol{H} \quad 3\text{-}17$$

where μ is the magnetic permeability which is also a property of magnetic material. Moreover, the magnetic field density is related to the magnetizing field vector by:

$$\boldsymbol{B}=\mu_0\mu\,\boldsymbol{H} \quad 3\text{-}18$$

μ_0 is the vacuum permeability. Thus, for a known magnetic field density, the following equation defines the magnetization vector:

$$\boldsymbol{M}=\frac{\chi}{\mu_0\mu}\boldsymbol{B}=\alpha\boldsymbol{B} \quad 3\text{-}19$$

In the presence of the magnetic core, the current associated to the magnetization vector may be represented in the form of the surface density $\boldsymbol{i_{ms}}$ or volume density, $\boldsymbol{i_m}$ defined by:

$$\begin{cases}\boldsymbol{i_m}=rot\,\boldsymbol{M}\\ \boldsymbol{i_{ms}}=\boldsymbol{M}\times\hat{n}\end{cases} \quad 3\text{-}20$$

In order to achieve mathematical simplicity in the core magnetic field equation, it is assumed that there is a uniform field inside the solenoid along its axis. In this way, the magnetization is initiated

uniformly and along the solenoid axis, with the added assumption that the material properties are constant. Combining equations (3-1) and (3-16), one can write:

$$\boldsymbol{A} = \frac{\mu_0}{4\pi}\iiint \frac{\boldsymbol{i}}{r}dv - \frac{\mu_0}{4\pi}\iint \frac{\hat{n}\times \boldsymbol{M}}{r}dS \qquad 3\text{-}21$$

By implying more mathematical procedure, we have:

$$\boldsymbol{B}(\rho,z) = B_\infty\, \overline{\boldsymbol{V}}(\rho,z) + \mu_0\alpha\, \boldsymbol{B}(\rho,z)\times \hat{n}\, \boldsymbol{G}(\rho,z) \qquad 3\text{-}22$$

where $\leq a_1, z \leq L$, $\overline{\mathrm{V}}$ and G are defined vectors of nonlinear functions. At a specific point inside the solenoid, the magnetic field magnitude is assumed to be known. Hence:

$$B(0,l/2) = \frac{\bar{V}(0,l/2)}{\left(1-\mu_0\alpha\ G(0,l/2)\right)}B_\infty = \beta\, B_\infty \qquad 3\text{-}23$$

$$\boldsymbol{B}(\rho,z) = B_\infty\left(\overline{\boldsymbol{V}}(\rho,z) + \beta\, \boldsymbol{G}(\rho,z)\right) = B_\infty \boldsymbol{V}_c(\rho,z) \qquad 3\text{-}24$$

At this point, the magnetic field of an electromagnet which is a cored coil of nonzero thickness can be calculated. The key point is that the linearity of soft core magnetization should be preserved before the saturation in magnetization graph happens.

3.2 The magnetic field of actuator

The navigation control can be arranged by any ordered array of coils and electromagnets. Each electromagnet has a specific configuration designed to produce the desired total magnetic field shape. In addition, the resultant gradient profile should naturally stabilize the ferromagnetic particle position in blood flow. In fact, the actuation force applied on a magnetic particle depends on the field gradient in all directions, whose profile defines the stability of the time varying equilibrium point or equilibrium path. The first step in the calculation of field gradient is to find the total magnetic field produced by a set of coils. According to (3-24), each electromagnet's magnetic field linearly relates to its input electrical current appearing in the defined control parameter, $B_{k,\infty} = \frac{\mu_0 N I_k(t)}{l}$. The total magnetic field is calculated using the superposition law as (please refer to Appendix for experimental proof of superposition law validity):

$$\boldsymbol{B}(\boldsymbol{X},t) = \sum_{k=1}^{n} B_{k,\infty}(t)\boldsymbol{j}_{k,c}(\boldsymbol{X}) \qquad 3\text{-}25$$

$$\boldsymbol{j}_{k,c}(\boldsymbol{X}) = \boldsymbol{R}_k \boldsymbol{V}_{k,c}(\boldsymbol{\rho}_\mathrm{k}) \qquad 3\text{-}26$$

$$\boldsymbol{B}(\boldsymbol{X},t) = \boldsymbol{J}_c(\boldsymbol{X})\boldsymbol{B}_\infty(t) \qquad 3\text{-}27$$

where $\boldsymbol{R}_\mathrm{k}$ is the rotation matrix of the k^{th} electromagnet,$\boldsymbol{V}_{\boldsymbol{k},\boldsymbol{c}}$ is the $\boldsymbol{V}_{\boldsymbol{c}}$ vector generated by the k^{th} electromagnet in a cylindrical coordinate, $\boldsymbol{J}_{\boldsymbol{c}}$ is a 3 by n matrix, B_∞ is the control vector, and ρ_k is the cylindrical position vector of the desired point in the k^{th} electromagnet local coordinate system. At this point, we are ready to find the exerted force on a magnetic particle by the actuator. The magnetic force for a particle with volume v and magnetization vector $\boldsymbol{M}$ moving in a magnetic field $\boldsymbol{B}$ is:

$$\boldsymbol{F}_{magnetic} = v\,(\boldsymbol{M}.\boldsymbol{\nabla})\boldsymbol{B} \tag{3-28}$$

For a ferromagnetic particle, (3-28) is changed to [33]:

$$\boldsymbol{F}_{magnetic}(\boldsymbol{X},t) = k_u \boldsymbol{\nabla}\|\boldsymbol{B}\|^2 \tag{3-29}$$

or:

$$\boldsymbol{F}_{magnetic}(\boldsymbol{X},t) = k_u \boldsymbol{g}(\boldsymbol{X},\boldsymbol{B}_\infty(t)) \tag{3-30}$$

$$\boldsymbol{g}\big(\boldsymbol{X},\boldsymbol{B}_\infty(t)\big) = \begin{bmatrix} \boldsymbol{B}_\infty{}^T \boldsymbol{Q}_1(\boldsymbol{X})\boldsymbol{B}_\infty \\ \boldsymbol{B}_\infty{}^T \boldsymbol{Q}_2(\boldsymbol{X})\boldsymbol{B}_\infty \\ \boldsymbol{B}_\infty{}^T \boldsymbol{Q}_3(\boldsymbol{X})\boldsymbol{B}_\infty \end{bmatrix} \tag{3-31}$$

$$\boldsymbol{Q}_j(r) = \frac{\partial(\boldsymbol{J}_c{}^T(\boldsymbol{X})\boldsymbol{J}_c(\boldsymbol{X}))}{\partial X_j}\ ,\ \ j = 1,2,3\ \ \boldsymbol{X} = \{X_{\boldsymbol{1}}, X_{\boldsymbol{2}}, X_{\boldsymbol{3}}\} \tag{3-32}$$

where k_u is a constant defined value. The equations (3-30,3-31) represent the quadratic form for the magnetic force and will be useful in dynamical equation

Given the induced force formula on a ferromagnetic particle by an electromagnetic actuator whose electromagnets and coils have specified orientation and positions, one can derive the dynamical equations of the movement inside the actuator working space. Afterwards, the proper stimulation is planned to achieve the concerned navigation performance. A simple example is introduced in the next section to establish the general form of dealing with the navigation problem via an electromagnetic set up. However, the explained dynamical equations can be transformed to different forms by any diffeomorphic mapping whenever it simplifies the control design.

3.3 Planar motion control example

In this section, an example of controlling a ferromagnetic particle movement in a fluidic environment is introduced and will be used to compare two actuator configurations latter. A set up composed of four horizontal electromagnets which have a radius of 1.9 *cm* and a length of 7 *cm* is employed in the following example. The electromagnets top plane is tangent to the surface of cylinder of radius 4 *cm*, and they are uniformly distributed. In this condition, the working area is a $4 \times 4\ cm^2$ horizontal plane (Figure 3-4).

With respect to the fact that the navigational equations of a spherical core contain the essential information of untethered micro-device movement, they are used to design and evaluate the tracking controller. The forces acting on a core can be divided into three categories, which take different forms of complexity in each operating system. Magnetic force is the actuation induced force and can be applied by either an MRI scanner (produced by either Helmholtz or Maxwell pairs) or a set of electromagnets and coils. This force was explained in detail in the previous section. The second group belongs to the resistive forces: the fluidic resistance and the contact force between the particle and the environmental boundaries.

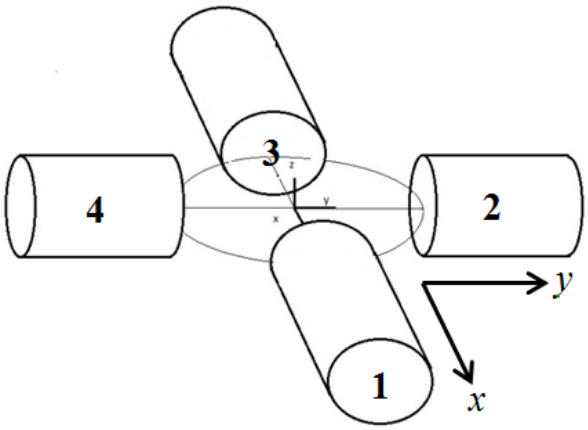

Figure 3-4: Horizontal arrangement of electromagnets.

In the case of navigation inside the blood vessels, blood flow results in a drag force, while touching the blood vessel produces frictional forces. The drag force in an unbounded fluid is depicted as:

$$\boldsymbol{D} = \frac{1}{2}\rho_f C_D A \|\boldsymbol{U}\|^2 \frac{\boldsymbol{U}}{\|\boldsymbol{U}\|} \qquad 3\text{-}33$$

where $\boldsymbol{D}$ is drag force, ρ_f is fluid density, C_D relates drag force to a dimensionless number and is called a drag coefficient, A represents sphere core cross section area, and $\boldsymbol{U}$ is the relative velocity of core to fluid flow. C_D is a function of a dimensionless Reynolds number estimated as:

$$C_D = \frac{24}{Re} + \frac{6}{1+\sqrt{Re}} + 0.4 \qquad 0 \le Re \le 2 \times 10^5 \qquad 3\text{-}34$$

Re number is defined:

$$Re = \frac{\rho_f \|\boldsymbol{U}\| d}{\mu} \qquad 3\text{-}35$$

in which d is the sphere diameter. Endovascular application implies the blood vessel wall affects drag force. Notwithstanding that blood vessel diameter varies according to heart contraction cycles, the vessels are assumed here to be a rigid body for the sake of simplicity. Accordingly, a correction coefficient to the relative velocity is introduced, which is a function of the ratio of the sphere diameter to tube diameter called λ. Munroe's studies introduced this coefficient, as shown below [25]:

$$\frac{V_t}{U} = 1 - \lambda^{1.5} \qquad \lambda < 0.6 \qquad 3\text{-}36$$

$$\lambda = \frac{d}{d_t} \qquad 3\text{-}37$$

where d_t is the sphere diameter and V_t is the estimated relative velocity in the blood vessel. In this modeling, the friction force is considered when the contacts are probable to appear. On the other

hand, the buoyancy and weight of the immersed particle are negligible in the fine vessels. Buoyancy and weight forces are expressed as:

$$\|\boldsymbol{F_w}\| = v\rho_m g \tag{3-38}$$

$$\|\boldsymbol{F_b}\| = v\rho_f g \tag{3-39}$$

where *v and* ρ_m are particle volume and density. Totally, the dynamical equation of immersed sphere can be written as:

$$\frac{d^2}{dt^2}\boldsymbol{X} = \frac{1}{v\rho_m}\left(\boldsymbol{F_{magnetic}} + \boldsymbol{F_w} + \boldsymbol{F_b} + \boldsymbol{D} + \boldsymbol{F_f}\right) \tag{3-40}$$

where $\boldsymbol{F_f}$ is the frictional force. The dynamical equations can take different forms depending on the forces in the system and the system's degrees of freedom.

In the case of electromagnetic actuation, the state space equation can be written as:

$$\begin{cases}\dot{\boldsymbol{X}}_{\boldsymbol{1}} = \boldsymbol{X_2} \\ \dot{\boldsymbol{X}}_{\boldsymbol{2}} = -\sigma_v \boldsymbol{U} + k_g \boldsymbol{g}(\boldsymbol{X_1}, \boldsymbol{B}_\infty(t)) + \boldsymbol{f_u}(t)\end{cases} \tag{3-41}$$

where $\sigma_v = \frac{\rho_f C_D A\|U\|}{2\rho_m v}$, $k_g = \frac{k_u}{\rho_m v}$ and $\boldsymbol{f_u}(t)$ is induced disturbance, and $\boldsymbol{X_1}, \boldsymbol{X_2}$ are position and velocity vectors. In this project it is assumed that the induced voltage due to the current change is ignorable. The state space model in Equation (3-41) is in the controllable canonical form by assuming the control term as a system input. If at each point where the control term admits at least one solution for input currents, the system is controllable. Therefore, the analysis of the relation between the input currents and assigned control vector will justify the control term's existence.

The nonlinear system in Equation (3-41) can be represented in the form of a cascade combination of a linear dynamical system and a memoryless nonlinear system, $(\overline{\boldsymbol{u}})^{-1} = \boldsymbol{g}^{-1}(\boldsymbol{X_1}, \boldsymbol{B}_\infty(t))$. According to Equation (3-31), the nonlinear control term has a quadratic form. It can be used to find the solution of a control term for any assigned control vector, $\boldsymbol{U_t}$. The new variable is defined as:

$$\boldsymbol{J_c}(\boldsymbol{X_1})\boldsymbol{B}_\infty(t) = \boldsymbol{P} \tag{3-42}$$

Substituting (3-42) into (3-31), we get:

$$\begin{bmatrix} \boldsymbol{J_c}(\boldsymbol{X_1}) \\ \left(\frac{\partial(\boldsymbol{J_c}^T(\boldsymbol{X_1})\boldsymbol{P})}{\partial \boldsymbol{X_1}}\right)^T \end{bmatrix} \boldsymbol{B}_\infty = \begin{bmatrix} \boldsymbol{P} \\ \frac{1}{2}\boldsymbol{U_t} \end{bmatrix} \tag{3-43}$$

Defining $\boldsymbol{P}$ as a spherical coordinate representation and taking Maxwell equations, $\boldsymbol{\nabla} \times \boldsymbol{B} = \boldsymbol{0}$, into account, Equation (3-43) can be written as:

$$\boldsymbol{R}(\varphi, \theta)\boldsymbol{J_m}(\boldsymbol{X_1})\boldsymbol{B}_\infty = \rho\{1,0,0,0,0,0\}^T + \frac{1}{2\rho}[\boldsymbol{0_{3\times3}} \quad \boldsymbol{I_{3\times3}}]\boldsymbol{U_t} \tag{3-44}$$

where:

$$\rho = \|\boldsymbol{P}\|, \boldsymbol{J_m} = \begin{bmatrix} \boldsymbol{J_c} \\ \dfrac{\partial \boldsymbol{J_c}}{\partial x_1} \\ \dfrac{\partial \left(\begin{bmatrix} 0 & 1 & 0 \\ 0 & 0 & 1 \end{bmatrix} \boldsymbol{J_c} \right)}{\partial x_2} \\ \dfrac{\partial ([0 \quad 0 \quad 1] \boldsymbol{J_c})}{\partial x_3} \end{bmatrix}, \boldsymbol{R}(\varphi, \theta) = \begin{bmatrix} (\boldsymbol{R_1})_{3\times3} & \boldsymbol{0}_{3\times6} \\ \boldsymbol{0}_{3\times3} & (\boldsymbol{R_2})_{3\times6} \end{bmatrix} \quad \text{3-45}$$

$$\boldsymbol{R_1} = \begin{bmatrix} \sin(\varphi)\cos(\theta) & \sin(\varphi)\sin(\theta) & \cos(\varphi) \\ -\sin(\theta) & \cos(\theta) & 0 \\ -\cos(\varphi)\cos(\theta) & -\cos(\varphi)\sin(\theta) & \sin(\varphi) \end{bmatrix}$$

$$\boldsymbol{R_2} = \begin{bmatrix} \sin(\varphi)\cos(\theta) & \sin(\varphi)\sin(\theta) & \cos(\varphi) & 0 & 0 & 0 \\ 0 & \sin(\varphi)\cos(\theta) & 0 & \sin(\varphi)\sin(\theta) & \cos(\varphi) & 0 \\ 0 & 0 & \sin(\varphi)\cos(\theta) & 0 & \sin(\varphi)\sin(\theta) & \cos(\varphi) \end{bmatrix}$$

The range and null space of $\boldsymbol{R}(\varphi, \theta)\boldsymbol{J_m}(\boldsymbol{X_1})$ for a defined value of (φ, θ) represents the system controllability at each point. It can be observed that the number of unknowns exceeds the number of equations when more than three electromagnets are used. In order to unify the solution, some constraints have to be considered. The current vector norm is used to be minimized in this chapter.

The 2D control of a horizontal system provides preliminary studies on the tracking control problem. The horizontal configuration depicted in Figure 3-4 is offered to initiate controlled movement in the xy-plane. The control problem is reduced to finding the input currents and $\boldsymbol{P}$ vector which minimizes the current vector's second norm. In this example, the inertial forces are assumed negligible relative to the viscous force. Moreover, the previous estimated optimization variable is used at each step as the initial value. Indeed, the input currents pass a low pass filter to prevent sudden change in system inputs. The filter time constant is chosen to be 0.01 *s* in order to accelerate the simulation running process. The block diagram of the controller is shown in Figure 3-5.

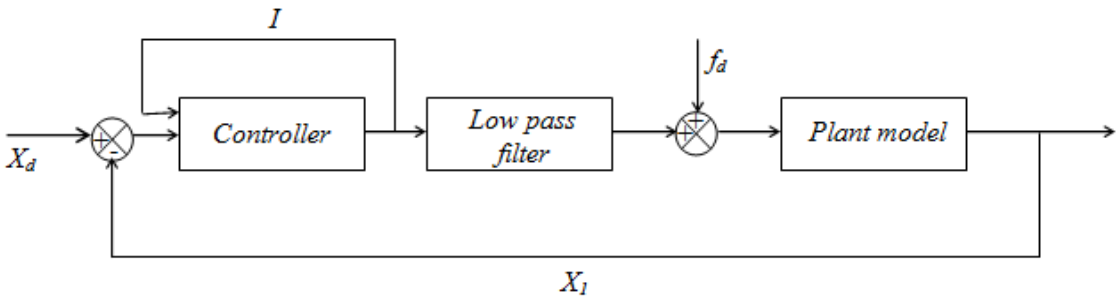

Figure 3-5: Block diagram of planar control motion by four horizontal electromagnets.

This experiment is done for an iron core when it is given that $^{k_g}/_{\sigma_v} = 0.285$. The simulation result for a ferromagnetic micro-particle with unit velocity, 1 *cm*, along the x-axis is depicted in Figure 3-6.

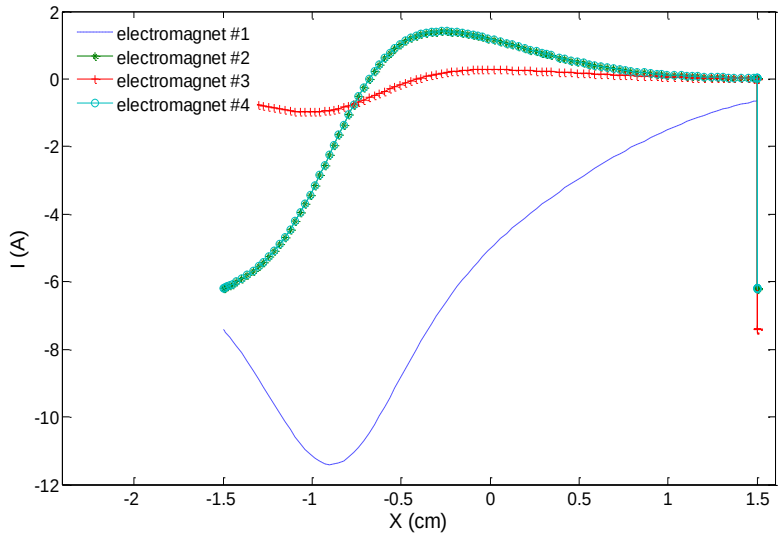

Figure 3-6: Simulation result for a ferromagnetic particle movement on x-axis.

The first issue observed from the simulation results is the large current values of electromagnet #1 (the front electromagnet) for 3/4 of the x-axis and electromagnets #2 and 4 (the side electromagnets) for more than 1/8 of the x-axis. This may cause overheating problems and significant energy dissipation. The sudden drop in the current values by passing half of the x-axis shows the intuitive attraction of the magnetic particle towards the front coil. The one directional attraction is the characteristic of a ferromagnetic particle in the presence of a single coil, since its magnetization vector is parallel to the magnetic field vector; therefore, the side coils need to interfere. The designed set up also initiates interconnectivity of dynamical equations. In this situation, providing the stability of the system is not simply achieved, as the controller is based on calculating an optimum point at each time step. It may induce sudden changes in the input currents and necessitate the use of a low pass filter. However, adding the low pass filter decelerates system response.

Chapter 4
New actuator structure and workspace optimization

In the last two chapters, the role of magnetic actuator design in ferromagnetic particle navigation was examined. The introduced movement control was applied by a horizontal configuration and shows that large current vector is required to provide the proper navigation; thus, a more efficient structure should be designed. In fact, the actuator design mostly involves defining the type and the placement of a set of coils. This procedure needs to focus on the achievement of the required mission. The question is which configuration should be chosen when the design purpose is known. In this chapter, the magnetic field of a single coil is investigated first, as the basic element. Next, two different configurations, horizontal and vertical, are considered to pave the way to an optimal design. An analytical approach is proposed to optimize the actuator structure to provide the maximum working space. Finally, a new augmented structure is proposed to reduce the energy consumption.

4.1 Initial simulation results

In general form, the magnetic field is proved to be the product of a non-dimension vector and current value. Figure 4-1 shows these quantities for an electromagnet with length 279 *mm*, and radius 150 *mm* (*Br*, *Bi* are radial and axial components of magnetic field, and $r0 = \rho$). The axial component of field variation with respect to radial distance in a plane 1 *cm* above the top plane is also shown in Figure 4-2 for different coil geometry.

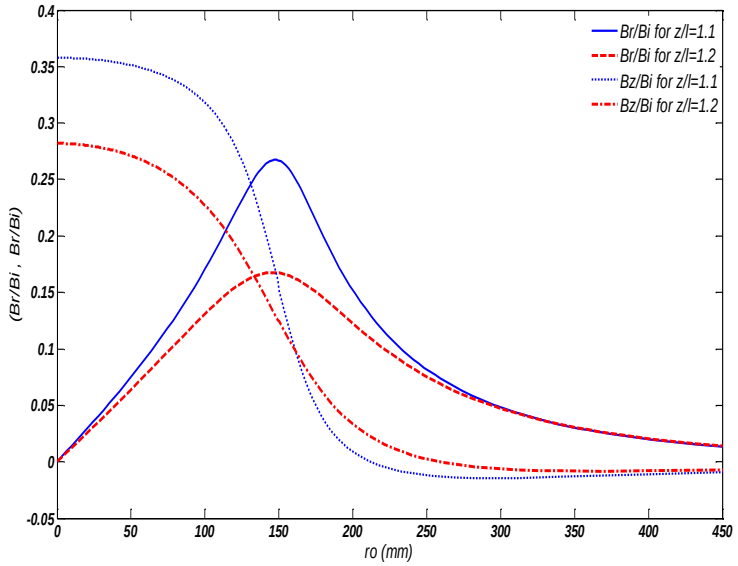

Figure 4-1: The computed magnetic field components for electromagnet with length 279 *mm*, and radius 150 *mm*.

It seems from the analytical formula that $\boldsymbol{V}$ solely depends on the geometrical parameters of an electromagnet. In addition, the results of the above electromagnet depict a larger axial component and its steeper change. Due the axial component importance in applied controlling forces, the magnetic actuation is mostly directed toward its profile shaping.

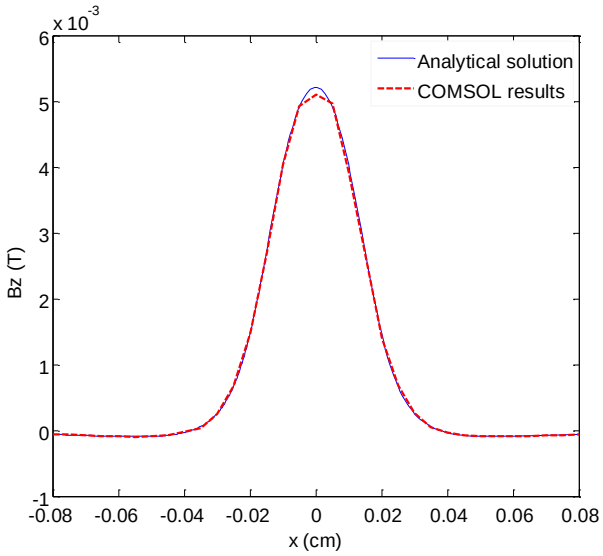

Figure 4-2: The axial component of magnetic field for a coil *with l*=4 *cm*, *N*=840, $a_1 = 1\ cm$, $a_2 = 2\ cm$, and *I*=1 *A* and 1 *cm* above the top base.

Before dealing with the magnetic field of a set of coils, it is useful to see how iron cores intensify the induced magnetic field. The analytical calculation of the new field was presented in the previous section, and its results are validated by experimental measurement. Figure 4-3 depicts the analytical and experimental results of the axial field component at electromagnet top plane for both $\rho = a_1$ and $\rho = 0$. The good match between the analytical results and experimental measurements carries out the efficiency of the defined equations. Using the equations, one can detect the length to radius ratio of the iron core as an important factor to boost the field. The wider the cylindrical structure is, the flatter the maximum area is. Therefore, the length to radius ratio defines the shape of magnetic field components for an electromagnet with a fixed length (Figure 4-4). Respectively, the total magnetic field will have less flatness when the electromagnet is used instead of a thin-wired coil with an average radius equal to outer radius of electromagnet. In this project the gradient coils are cored and called electromagnets.

Now, the induced magnetic field by a set of electromagnets is considered. Two different structures, vertical and horizontal configuration, are proposed for the electromagnets' alignment, to identify the role of the electromagnets configuration. The horizontal configuration is identical to the one utilized in the previous two chapters, and the vertical configuration is composed of vertical electromagnets. The electromagnets' top plane is tangent to a horizontal plane, and their centers are constrained to be

on a unique circle whose diameter is defined (Figure 4-5). A similar structure is used in MagLev lab at University of Waterloo.

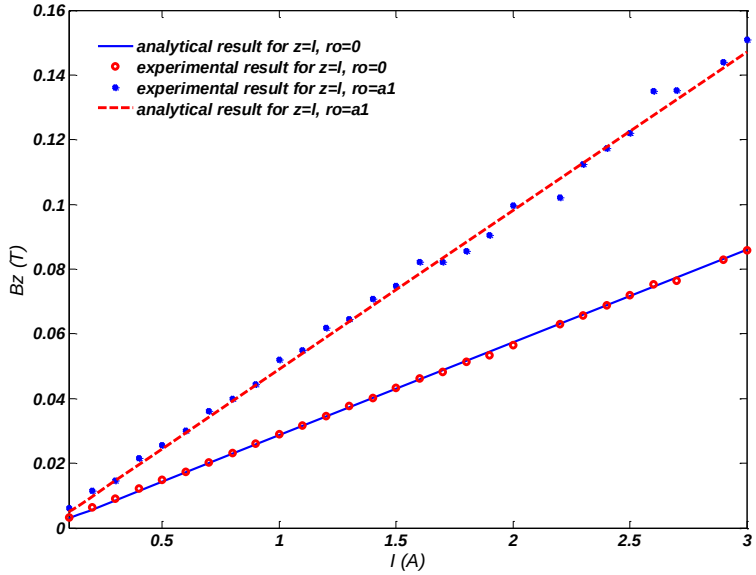

Figure 4-3: magnetic field axial component for an electromagnet with iron core, *l*=4 *cm*, *N*=840, $a_1 = 1\ cm$ and $a_2 = 2\ cm$, as a function of current at top plane

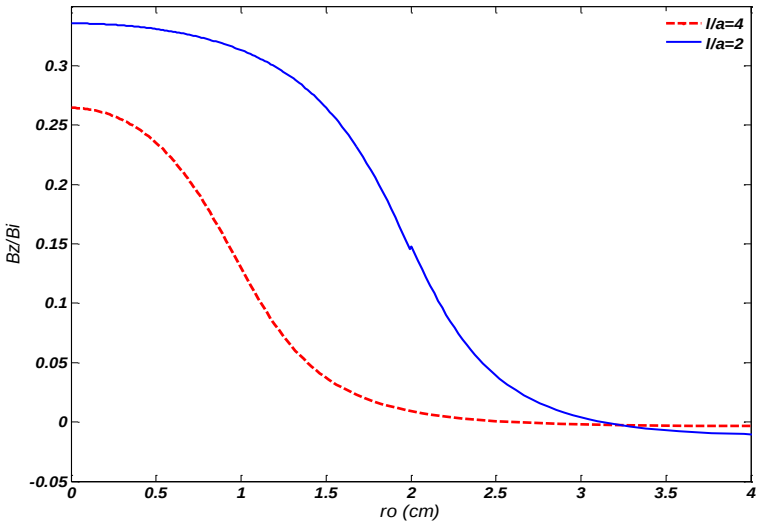

Figure 4-4: The computed axial magnetic field component for a coil with *l*=4 *cm* and fine wiring surface as a function of radial distance.

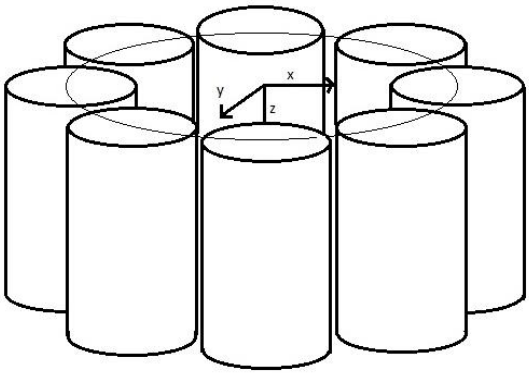

Figure 4-5: The vertical arrangement of electromagnets.

First, the stimulation of a vertical structure composed of two electromagnets on a magnetic particle is demonstrated. The Figure 4-6 shows the magnetic field produced by this set up when both electromagnets carry the same currents. It is observed that there are two maximum points below the centers of electromagnets. According to the magnetic force equation, each force component is a weighted summation of corresponding magnetic gradients. Since the gradient vector of z-component is larger than the other components, only this vector defines the system kinematics and dynamics. With respect to the gradient matrix symmetry and the magnetization direction which is large along z-axis, the final force equation is transformed to the following form:

$$\boldsymbol{F}_{magnetic}(\boldsymbol{X},t) = vM_z\left(\frac{\partial B_x}{\partial z},\frac{\partial B_y}{\partial z},\frac{\partial B_z}{\partial z}\right)^T \qquad 4\text{-}1$$

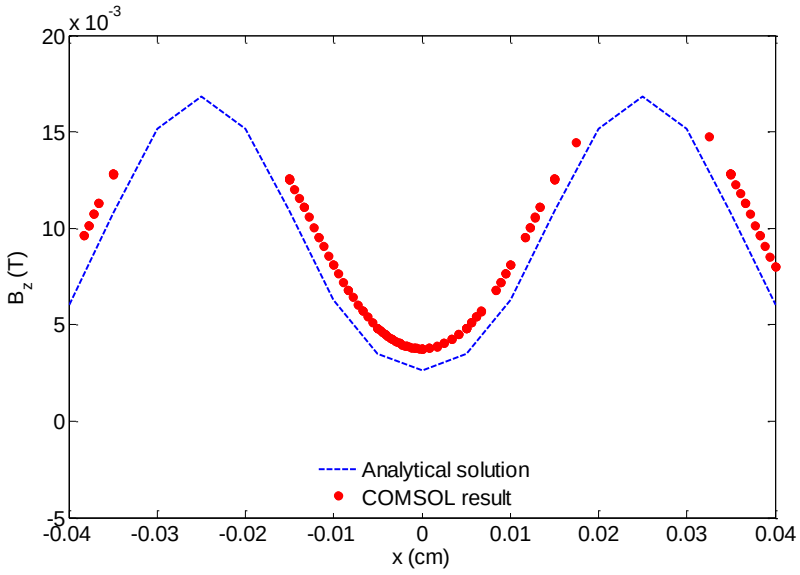

Figure 4-6: The axial component of magnetic field of two electromagnets located at 5 *cm* distance to each other carrying current vector {1,1} *A* on a plane 1 cm above the electromagnets top base.

According to the equation (4-1), the maximum points of the magnetic field z-component are stable equilibrium points. In this condition, the magnetic particle is attracted toward the maximum points. However, the position of the particle had to be controlled better by initiating a unified maximum point at each time. Multiple maximum points are reduced to one point when the particle is moving in a plane far from the electromagnets' top planes. Consequently, the current vector sets the maximum point location as it is exhibited in Figure 4-7 for current vector {1, 1} *A* and Figure 4-8 for current vector {2, 1} *A*. Similarly, the magnetic force can be extended from axial to planar by adding more vertical coils.

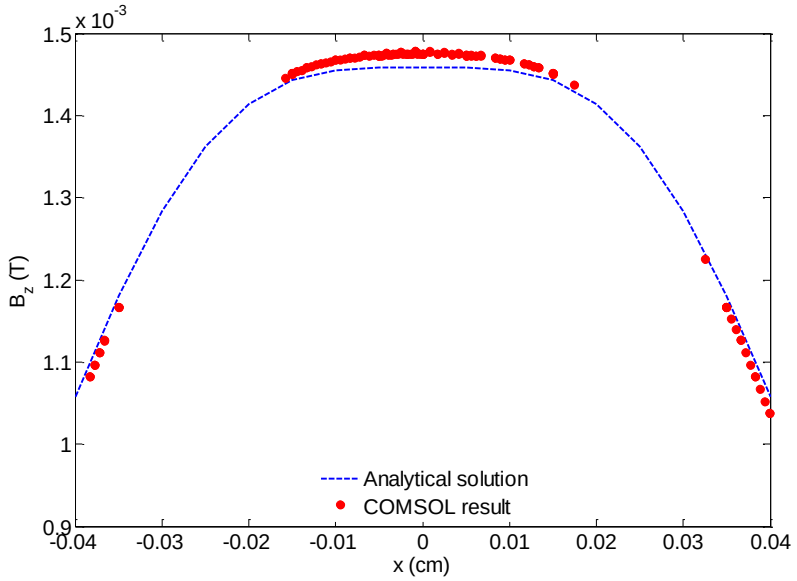

Figure 4-7: The axial component of magnetic field of two vertical electromagnets located at 5 *cm* distance to each other carrying current vector {1,1} *A* on a plane 5 *cm* above the electromagnets top base.

In fact, the vertical structure does not provide sufficient forces to resist the environmental reactions since the working space is not close to the electromagnet's surface. Therefore, a different structure is required to encounter environmental forces. The horizontal arrangement of the electromagnets offers better performance for navigation in the horizontal plane including coils axes. In the same way, the studies are focused on the magnetic field produced by two electromagnets. In this case, the electromagnets are aligned along the x-axis, and their local z-axes are directed toward the actuator center. The stimulation of the magnetic particle can be also provided by initiating an attracting point; the magnetic field should be biased nevertheless with a constant field (please refer to chapter 4 for more details). The x-component of the magnetic field is shown when the current vector has the same elements in Figure 4-9, and different values in Figure 4-10. In both cases, the current's direction is chosen to actuate a maximum point in the magnetic field profile.

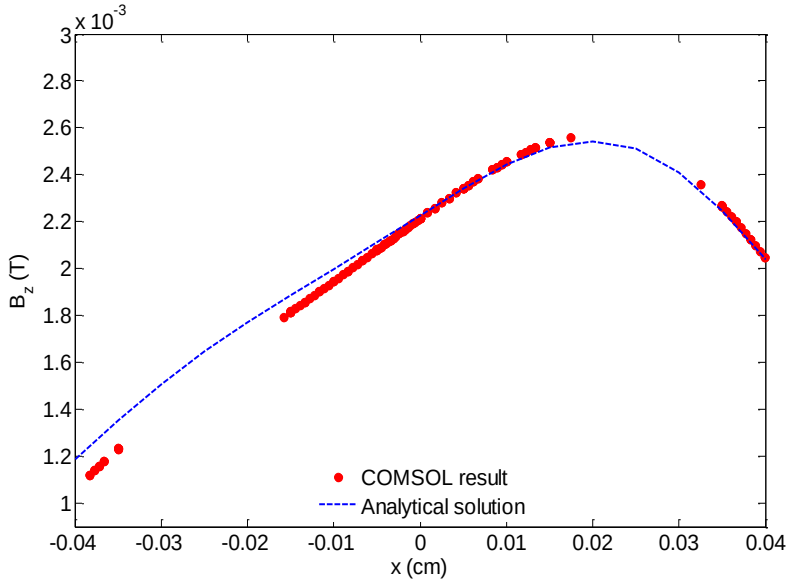

Figure 4-8: The axial component of magnetic field of two vertical electromagnets located at 5 *cm* distance to each other carrying current vector {2,1} *A* on a plane *5 cm* above the electromagnets top base.

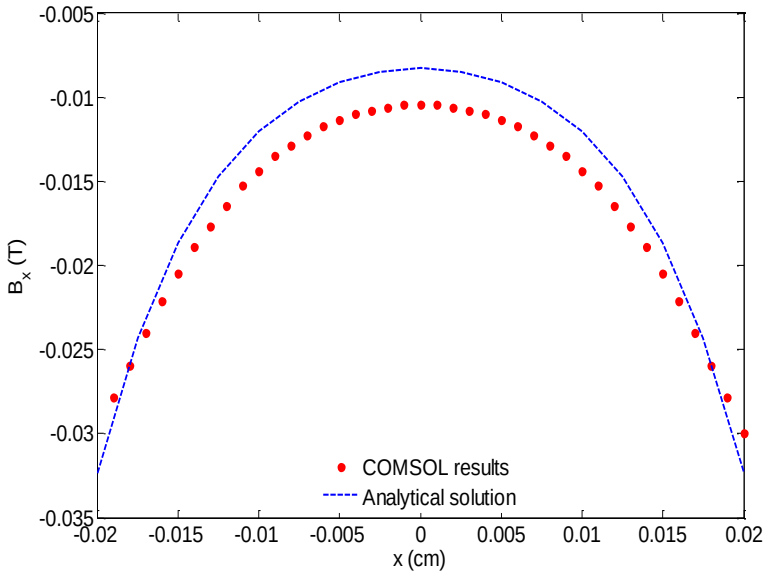

Figure 4-9: The x-component of magnetic field of four electromagnets located around a circle with radius 5 *cm* (horizontal structure) and carrying current vector {1,-1} *A*.

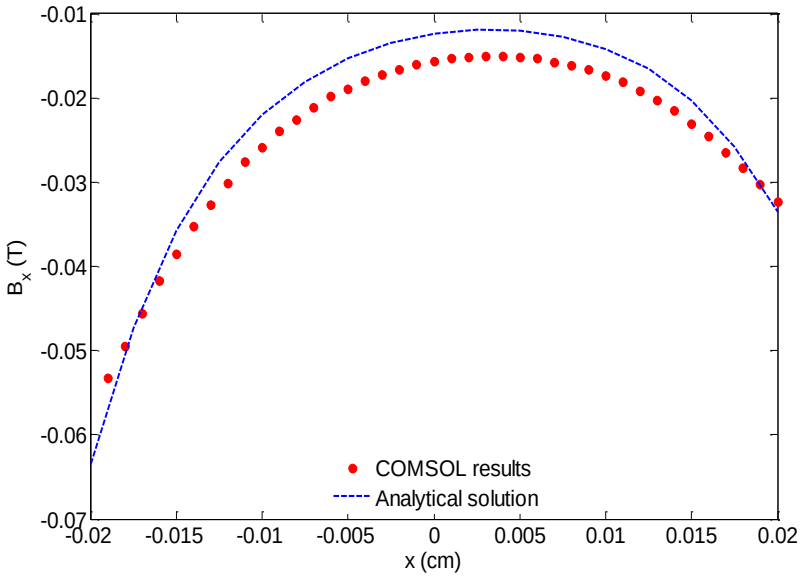

Figure 4-10: The x-component of magnetic field of four electromagnets located around a circle with radius 5 *cm* (horizontal structure) and carrying current vector {2,-1} *A*.

It follows that the maximum point location moves along x-axis by changing the currents ratio; however, the maximum point is a flat area. This happens because the distance between the electromagnets' top surfaces is more than the diffusion range of axial magnetic field component for each coil. Rather than making the electromagnets closer, one can sharpen the maximum point by increasing the current values. While physical constraints limit the possibility of working space reduction by enclosing the electromagnets, the current's maximum value is constrained by the energy dissipation issue. A method is needed for the optimization of the structure design and the satisfaction of all the constraints. To achieve this end, the system working space needs to be defined and transformed into the mathematical equation forms.

4.2 Working space optimization

The magnetic force vector is defined by both the magnetic field vector and the magnetic field gradients. The induced force by a single electromagnet is attractive and decreasing by the distance from the top plane. In fact, an actuator is designed to produce both appropriate magnetic field vector and gradient elements. The diffusion range of magnetic field is mostly defined by the coil's diameter; but increasing the current magnitude magnifies the force vector. As was mentioned, the physical constraints limit the maximum coil diameter, and the maximum current is limited due to the large heat dissipation issue. A criterion is required to optimally define the number, alignment, position, and diameter of the coils which maximize the working space.

In particular, the working space is defined as a compact set of points at which any desired force is accessible. This condition is sufficient for the non-extended model to be locally controllable; the extended state space model includes an additional state vector nonetheless. An extra condition is proven to be required to provide the weak controllability. At this point, the first condition is addressed to optimize the actuator design. According to this condition, the force vector should span the space by changing the current vector at each point of working space. Therefore, the matrix $\boldsymbol{M_W} = \boldsymbol{R}(\varphi,\theta)\boldsymbol{J_m}(\boldsymbol{X_1})$ must be full rank for all points of the working space and any direction of magnetization vector. In either case, there will be some force vectors inaccessible by input currents.

Finally, the actuator optimal design is converted to the interval matrix analysis problem whose elements are interval functions of position. In fact, the purpose of the new optimization problem is to maximize the working space where the matrix $\boldsymbol{M_W}$ has full rank. The coils' length, diameter, its alignment and location are the optimization variable; however, the problem remains too sophisticated. In order to attain an applicable method, the introduced variables are forced to meet some constraints. The coils' dimensions are chosen to minimize the heat dissipation while their top planes are set tangent to a known surface. If it is assumed that the coils have no overlap and have uniform distribution over the surface, then the number of coils, their radius and the surface geometrical parameters define the problem.

To begin with, the matrix $\boldsymbol{M_W}$ is composed of n-square matrices with *n*=4 for 2D and *n*=6 for 3D structure which are functions of position coordinates and the magnetization direction. This matrix defines the existence and magnitude of input current vector according to the following equation:

$$\boldsymbol{M_W I} = \alpha \begin{Bmatrix} \|\boldsymbol{M}\| \\ 0 \\ 0 \\ \dfrac{\beta \boldsymbol{U_t}}{2\|\boldsymbol{M}\|} \end{Bmatrix} = \boldsymbol{V} \qquad 4\text{-}2$$

where $\boldsymbol{I}$ is the current vector, $\|\boldsymbol{M}\|$ is the magnitude of magnetization vector, and α, β are constant. An alternative factor to compare two structures performance is the norm of current vector. In fact, the Lagrangian method is used to minimize the 2- norm when the minimization problem is constrained by (4-2). Accordingly, the following relation between current vector and Lagrangian constant vector is obtained:

$$2\boldsymbol{I} + \boldsymbol{M_W}^{\boldsymbol{T}}\boldsymbol{\lambda} = 0$$

$$\boldsymbol{I} = \boldsymbol{M_W}^{\boldsymbol{T}}\left(\boldsymbol{M_W}\boldsymbol{M_W}^{\boldsymbol{T}}\right)^{-1}\boldsymbol{V}$$

Therefore, the cost function takes the form of:

$$\overline{Co} = \boldsymbol{V^T}\left(\boldsymbol{M_W}\boldsymbol{M_W}^{\boldsymbol{T}}\right)^{-1}\boldsymbol{V}$$

$$\overline{Co} = \boldsymbol{V^T T}\left(\boldsymbol{M_W}\boldsymbol{M_W}^{\boldsymbol{T}}\right)^{-1}\boldsymbol{T^T V}$$

where $\boldsymbol{T}$ is the transformation matrix whose columns are the eigenvectors of $\boldsymbol{M_W}\boldsymbol{M_W}^{\boldsymbol{T}}$**.** By defining a new vector $\boldsymbol{W} = \boldsymbol{T^T V}$, the cost function can be represented as

$$\overline{Co} = \sum_{i=1}^{6} \left(\frac{1}{\lambda_i}\right) {w_i}^2 \qquad 4\text{-}3$$

where λ_i's are the eigenvalues of $\left(\boldsymbol{M_W M_W}^{\boldsymbol{T}}\right)$. Finally, maximizing the eigenvalues leads to finding an optimal structure.

The area enclosed by electromagnets is divided into smaller intervals along the coordinate axes, as well as the range of magnetization vector angles in the spherical coordinates. In fact, the larger eigenvalues at each point brings around smaller currents; thus, a function of eigenvalues is a good choice for optimization cost function. A simple candidate for cost function is the weighted sum of geometric and arithmetic mean of $\left(\boldsymbol{M_W M_W}^{\boldsymbol{T}}\right)$ eigenvalues which should be maximized. However, the defined cost function should be extended on the area concerned. In general, the cost function value is a function of position coordinates, and is a positive value variable. The integration of the cost function over the chosen area can be maximized as an alternative for the total optimization criterion.

In the previous section, two specific electromagnetic structures were studied. Each of them indicates the match to a specific task while their electromagnets' configurations still need to be defined optimally. In this section, the proposed optimization criterion is applied to solve a more general optimization problem in which the system is composed of a number of electromagnets with the alignment and positioning required to be calculated. Let the electromagnets' top planes be tangent to a sphere with a defined diameter. Since the electromagnets are assumed to cover the sphere's surface uniformly, their maximum number is increasing with the sphere diameter. First, the structure is made of six electromagnets whose diameter is 4 *cm*, and the sphere is of diameter 5 *cm*. The electromagnets are arranged pairwise and uniformly cover the volume inside the enclosed sphere. By the above assumption, 22 electromagnets are required to cover a workspace of diameter 10 *cm*, though.

In the first place, the geometric mean of the eigenvalues of the matrix $(M_W {M_W}^T)$ or $G = (det(M_W {M_W}^T))^{1/6}$ is calculated as the cost function. The result is shown in Figure 4-11 on a horizontal plane located 0.2 cm above the x-y plane and for both structures. More details can be found in Figure 4-12 and Figure 4-13 when the cost function is defined as the weighted sum of geometric and arithmetic means, $Co = .1M + 1000G$, where M is arithmetic mean of the eigenvalues, G is geometric mean of eigenvalues, and *Co* should be maximized. In fact, the coefficients of the weighted sum are set after calculating the values of both means at different points of workspace. Both terms should have the same order of magnitude in the cost function equation, and the coefficients are chosen to achieve this end. As a result, both minimum and maximum eigenvalues are maximized.

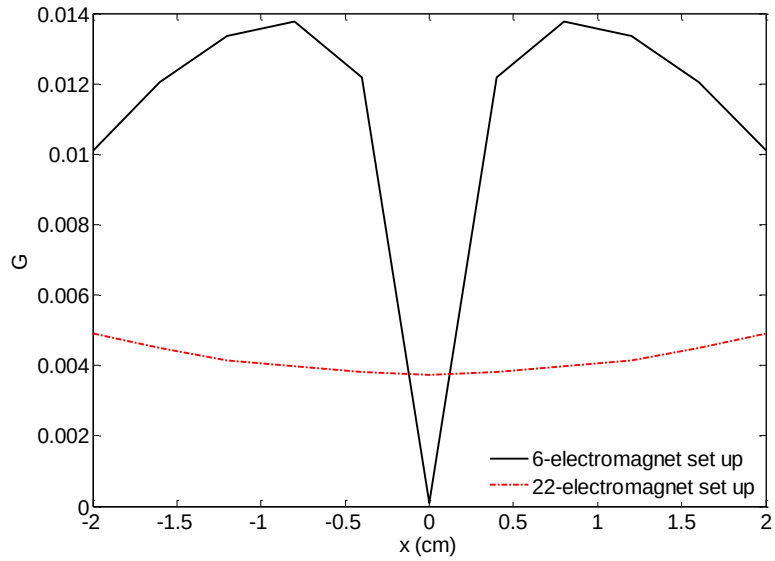

Figure 4-11: The variation of the geometric mean along the x-axis and on the horizontal plane.

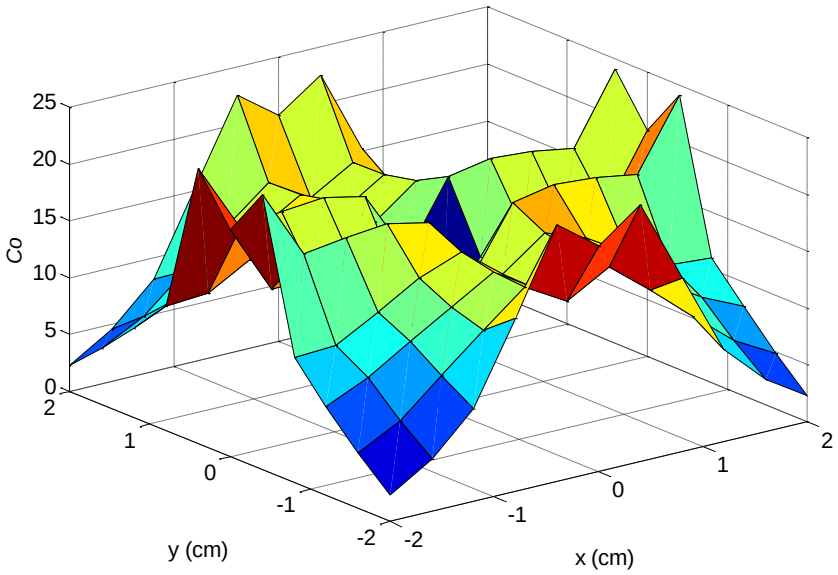

Figure 4-12: The variation of the cost function for 6-electromagnet set up and on the horizontal plane.

It is discernible from Figure 4-14 that the integration of cost function over a workspace of diameter 10 *cm* linearly increases by the number of electromagnets; nevertheless, the energy and physical constraints limit this number. On the other hand, the number of electromagnets is constrained from below due to the limited norm of maximum current. Besides, super conducting electromagnets,

employed in some medical applications, significantly eliminate the heat dissipation, admitting a larger limit for the current norm. In general, the six-electromagnet set up is preferred since it provides larger cost function summation.

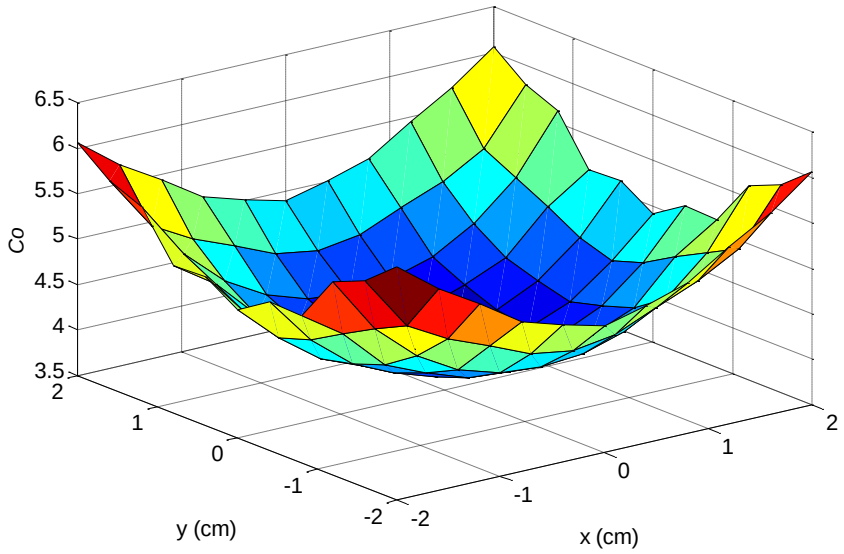

Figure 4-13: The variation of the cost function for 22-electromagnet set up and on the horizontal plane.

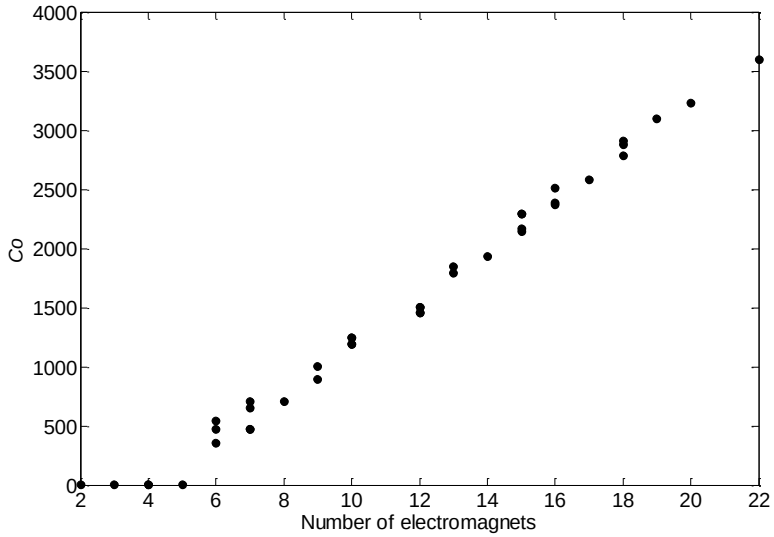

Figure 4-14: The variation of cost function integration by the number of electromagnets for a workspace of diameter 10 *cm*.

Although a structure is optimized by the introduced cost function in the previous section, it may still be some singular points in the working space. At these points, some of the electromagnets should carry a large current value. This issue can be included in the cost function equation by a coefficient of an additional term, $\frac{1}{(1+N_S)}$, where N_S is the number of singular points. However, the singular points may be avoided depending on the assigned application during the particle motion control. On this matter, comparing the results of Figure 4-12 and Figure 4-13 shows that a larger number of electromagnets eliminates the singular points. In general, designing an optimum structure is a tradeoff between choosing the number of electromagnets and their diameter.

On the other hand, expanding the working space is not applicable when the actuation force is applied by the external magnetic field of a set of electromagnets. Since the range of magnetic field diffusion for each coil is limited, the sudden drop in geometric mean of determinant value at the center of the working space is observed. A potential solution is adding uniform magnetic field in three dimensions to provide the magnetic field vector and its gradients independently. The maximum eigenvalue assigned to the matrix M_W, which is the maximum eigenvalue of its 6×6 sub-matrices, is sketched for the four electromagnetic 2D structure and its augmented structure with Helmholtz coil of diameter *4 cm* in Figure 4-15. Accordingly, the optimization factor can be dramatically increased while the number of singular points is reduced over the defined area. The comparison between the maximum determinants associated to the matrix M_W of the two structures (Figure 4-15) clearly presents this improvement. The effect of uniform magnetic field will be discussed in more details in the next section.

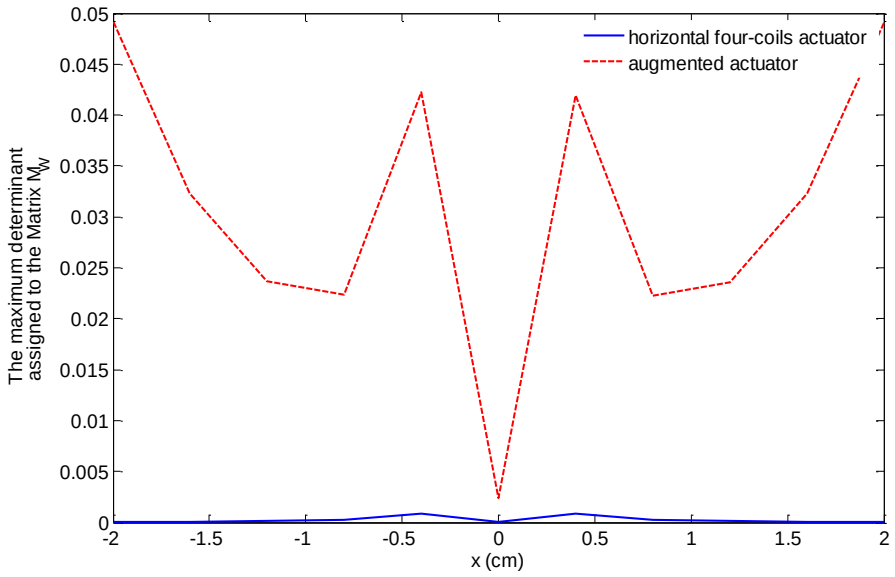

Figure 4-15: The variation of maximum determinant assigned to the matrix M_W along x-axis.

In the calculation process of a magnetic field, it is assumed that the superposition law is applicable. In the existence of soft material, the magnetic field equation can be written as an integral equation. In

this equation, the magnetic field is the state variable and current vector is the input of the integral equation. It is easy to prove that the integral equation is linear when the magnetization vector, M, is linearly represented as a function of the magnetic field, B. Therefore, the condition of the superposition law is satisfied and the magnetic field is represented as a linear function of the current vector.

In this project, the electromagnets are equipped with iron cores with saturation magnetic field between 1.5T to 2T, wherein all the equations are linear (please refer to appendix for more information). Besides, pole pieces and soft yokes often improve the actuator-produced magnetic force within the required area. While the utilized soft material shows a linear relation between the magnetization vector and magnetic field vector, the introduced criterion is applicable to compare the performance of different structures. This optimization method can be employed especially in micro structures where the main concern is designing an effective soft frame.

4.3 A new magnetic actuator design

Heretofore, augmenting the electromagnetic set up with uniform coils is demonstrated to improve the performance due to the larger cost function. Now, this improvement is studied from a different point of view. On this matter, the analysis is also based on the analytical equation for magnetic force. Starting from the magnetic force equation, one can investigate the reason behind the intuitive attraction of the ferromagnetic particle by an electromagnet. With respect to the gradient matrix symmetry, equation (3-28) (which is the magnetic force equation) can be rewritten as:

$$\boldsymbol{F}_{magnetic} = v\,(\boldsymbol{\nabla B}.\boldsymbol{M}) \tag{4-1}$$

Assuming the off-diagonal elements to be negligible, one can observe how the agreement of the magnetization direction with the diagonal elements signs affects the resultant force. In other words, the diagonal elements can be put into a vector called the magnetization vector. Respectively, the resultant force in each direction is the product of the corresponding elements of magnetization vector and gradient vector. However, the assumption is tolerated in practical examples.

The x-component of the magnetic field vector induced by the magnetic actuator is depicted in Figure 4-16. The actuator structure was introduced in the previous chapter. Now that the control purpose is to move the particle on the x-axis from one side to the other, the x-component of the magnetic field is considered. The effect of side electromagnets is considered to be relatively small, and the force is formed mainly by front and rear electromagnets. Now, the magnetic force projection on x-axis is:

$$\boldsymbol{F_x} = v\,(\boldsymbol{M_x}\frac{\boldsymbol{\partial B_x}}{\boldsymbol{\partial x}} + \boldsymbol{M_y}\frac{\boldsymbol{\partial B_y}}{\boldsymbol{\partial x}}) \tag{4-2}$$

Since the effect of side coils is ignorable when the current vector elements are of the same absolute values, the second term goes to zero. According to equation (4-2) and the Figure 4-16, the magnetic particle is attracted to the closer electromagnet. This is also true when the currents of both electromagnets on the x-axis have different signs.

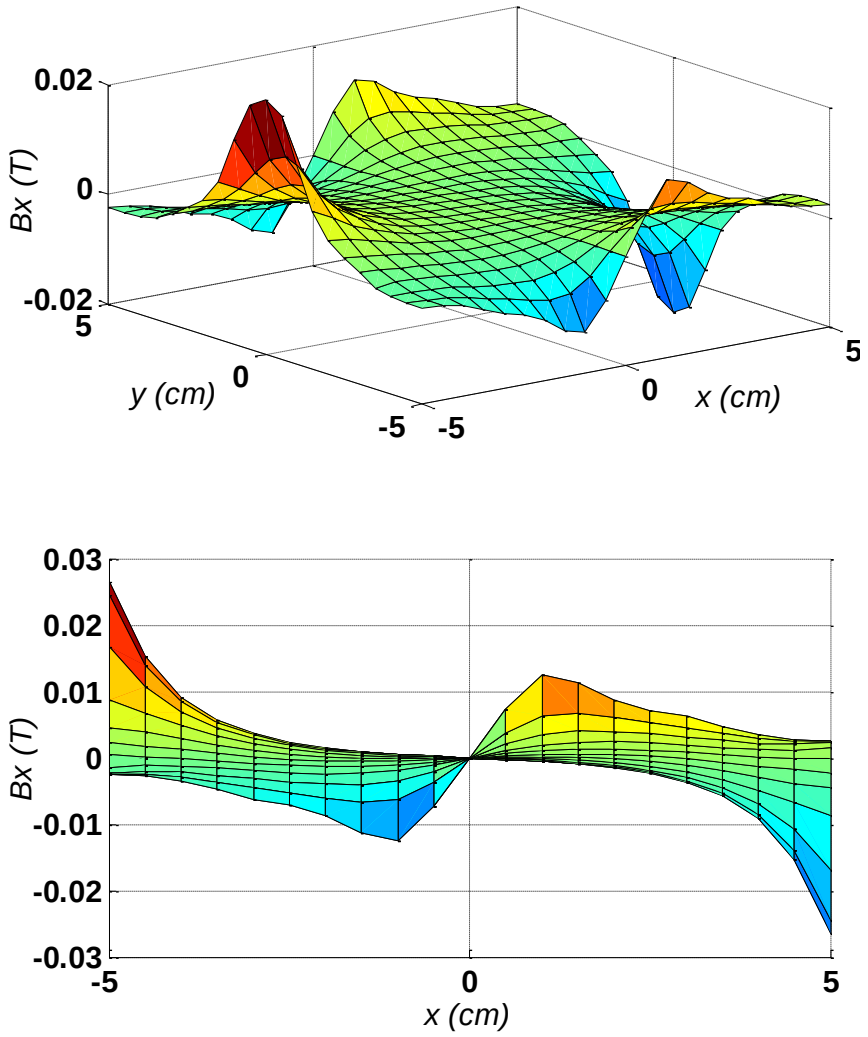

Figure 4-16: The x-component of magnetic field of four electromagnets located around a circle with radius *5 cm* (horizontal structure) and carrying current vector {1,1,1,1} *A*.
(The field is calculated in coils axes plane.)

As a matter of fact, a different current ratio for on-x-axis electromagnets changes the region of attraction; nevertheless, large current is required to be passed to the target electromagnet. In this case, the side electromagnets boost the attraction toward the desired spot depending on their currents' directions and values. Besides, one can improve the performance by controlling the magnetization direction. In order to add more details, the x-component of magnetic field when the reverse current directions are chosen for the on-x-axis electromagnets is shown in Figure 4-17. In this figure the magnetic field is biased with a constant value.

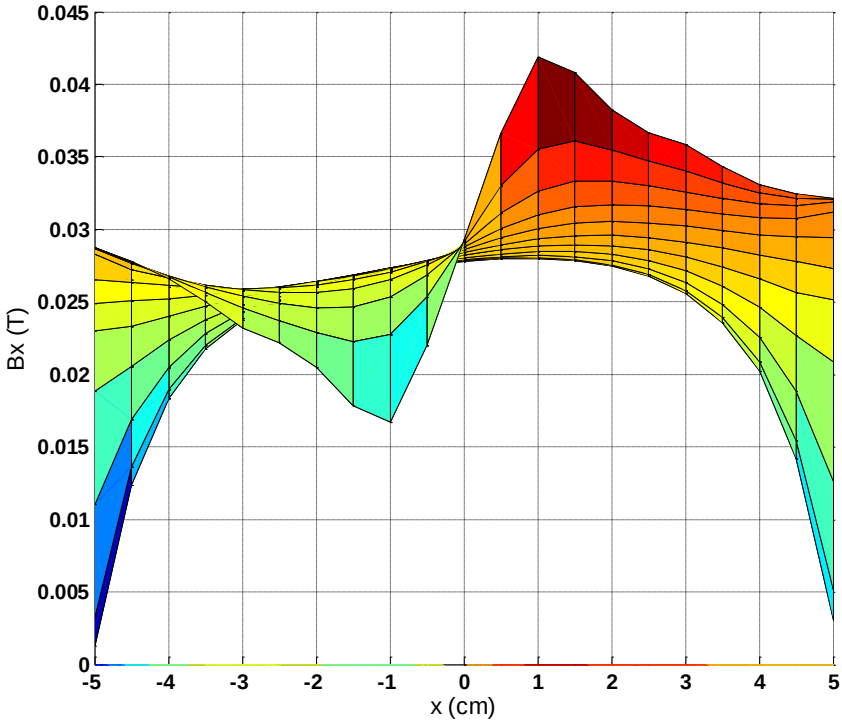

Figure 4-17: The x-component of magnetic field of four electromagnets located around a circle with radius 5 *cm* (horizontal structure) and carrying current vector {1,1,-1,1} *A*. The field is biased by 0.03 *T*. (The field is calculated in coils axes plane.)

By applying this modification, an attractive maximum point is constructed. In general form, the magnetization vector can be represented as the summation of two vectors: the magnetization vector produced by gradient coils, and the one induced by uniform coils. In this manner, the magnetic force equation may be transformed to the following form:

$$\boldsymbol{F_i} = v\,(\frac{\boldsymbol{\partial B_i}}{\boldsymbol{\partial X}}.\boldsymbol{M}) \qquad 4\text{-}3$$

$$\boldsymbol{F_i} = k\,(\frac{\boldsymbol{\partial B_{Gi}}}{\boldsymbol{\partial X}}.\boldsymbol{B_G} + \frac{\boldsymbol{\partial B_{Gi}}}{\boldsymbol{\partial X}}.\boldsymbol{B_U}) \qquad 4\text{-}4$$

where B_G is the gradient coils field, and B_U is the uniform coils field. If the uniform magnetic field has the same order of magnitude as the gradient field, the second term in equation (4-4) plays an important role to form the major force. Therefore, adding the uniform coils to the magnetic actuator structure for each direction improves the system performance. This improvement can be achieved by Helmholtz coils sketched in Figure 4-18 for 2D actuation.

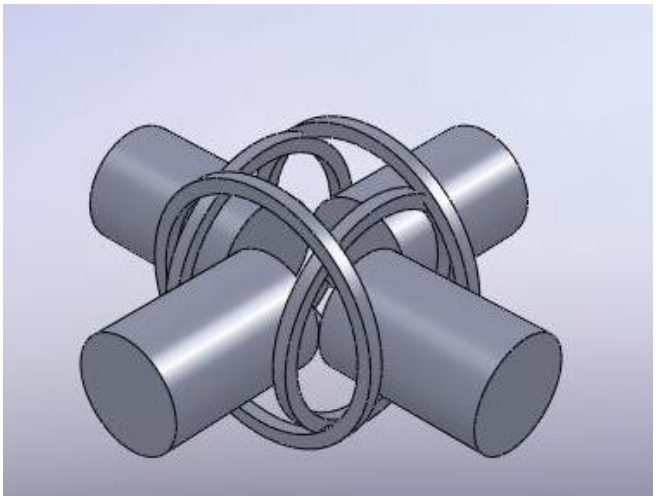

Figure 4-18: The new magnetic actuator composed of electromagnets and Helmholtz coils.

4.4 Planar motion control example via new actuator design

In this section, the same example as the one introduced in section 3.3 is solved when the augmented structure is employed to stimulate the movement. The equations (3-34),(3-3-44) are rewritten as:

$$\begin{bmatrix} \boldsymbol{J_{c1}} & \boldsymbol{J_{c2}} \\ \left(\frac{\partial\left(\boldsymbol{J_{c1}^T}(\boldsymbol{X_1})\boldsymbol{P_1}+\boldsymbol{J_{c1}^T}(\boldsymbol{X_1})\boldsymbol{P_2}\right)}{\partial \boldsymbol{X_1}}\right)^T & 0 \end{bmatrix} \boldsymbol{B}_\infty = \begin{bmatrix} \boldsymbol{P}=\boldsymbol{P_1}+\boldsymbol{P_2} \\ \frac{1}{2}\boldsymbol{U_t} \end{bmatrix} \quad 4\text{-}5$$

where:

$$\boldsymbol{J_m} = \begin{bmatrix} \boldsymbol{J_{c1}} & \boldsymbol{J_{c2}} \\ \frac{\partial \boldsymbol{J_{c1}}}{\partial x_1} & 0 \\ \frac{\partial\left(\begin{bmatrix}0 & 1 & 0\\ 0 & 0 & 1\end{bmatrix}\boldsymbol{J_{c1}}\right)}{\partial x_2} & 0 \\ \frac{\partial([0 \quad 0 \quad 1]\boldsymbol{J_{c1}})}{\partial x_3} & 0 \end{bmatrix} \quad 4\text{-}6$$

where $\boldsymbol{J_{c1}}$ is a 3×n matrix, and $\boldsymbol{J_{c2}}$ is 3×3 matrix. The former matrix is corresponded to the n gradient coils, and the latter one is corresponded to the uniform coils and has full rank. It is easily detected that the last three columns of $\boldsymbol{J_m}$ provides three independent columns; thus, the matrix is more likely to be full rank. The simulation results for input currents are shown in Figure 4-19. Moreover, the norm of current vector is exhibited in Figure 4-20.

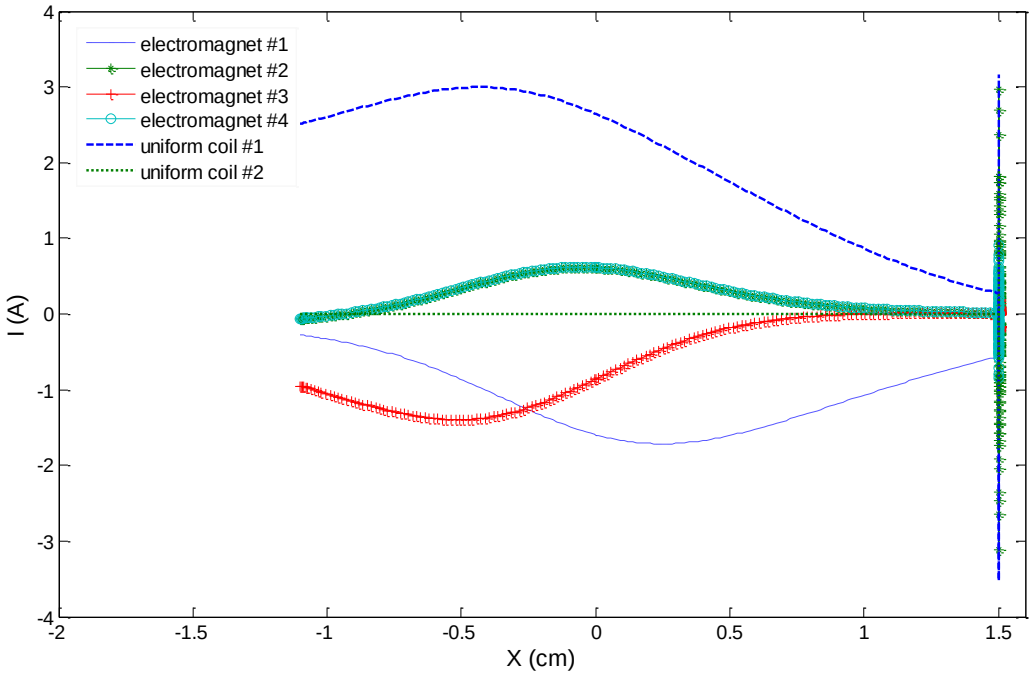

Figure 4-19: The simulation result for a ferromagnetic particle movement on x-axis actuated by new augmented configuration.

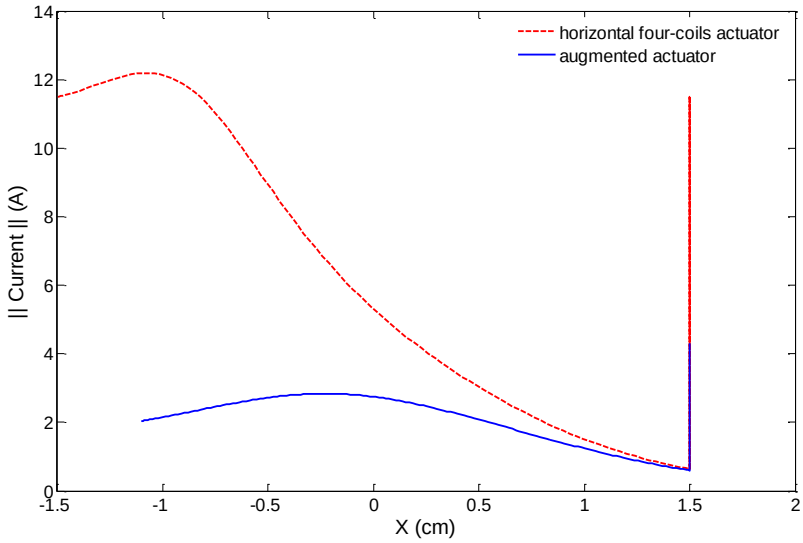

Figure 4-20: The comparison between the energy dissipation by two different actuator designs.

The implemented simulation admits a larger time constant since the current values are smaller than the previous example, and the same time constant decelerates the running process. As expected, the currents' values are reduced to some order of magnitude. The magnitude of the cost function, the current vector norm, drops significantly by changing the particle position along the x-axis, emphasizing the role of uniform fields. In addition to the improved structure, a more general control method is required to provide adequate navigation along a specific path. In fact, the introduced method needs nonlinear optimization to be repeated at each time step, which is not proper; it causes time delay and current discontinuity that should be compensated by a low pass filter. All in all, the designed control signal is not continuous. In the next section, a trajectory tracking control is proposed to benefit the precise navigation.

Chapter 5
Trajectory tracking control design

In the last two chapters, a controller was introduced to compare the performance of two different electromagnetic actuators to move a ferromagnetic particle along a straight line. The controller was designed to find an optimal current vector at each point and thus was combined with a low pass filter. It is discernible that at each time step a nonlinear optimization problem should be solved, which is a time consuming process is. Moreover, the path is divided into several points, and the particle is supposed to point toward them one by one through its trip on the defined path. A more general approach is required to control the movement of the particle. Path following and trajectory tracking controllers are two methods of keeping the movements of a system tracked. A multi-input multi-output (MIMO) trajectory tracking controller is proposed in this section to initiate navigation along a path with a fixed velocity.

5.1 The system main properties

First, the state space representation of the concerned electromagnetic system needs to be defined. The system is represented in section 3 as

$$\begin{cases} \dot{\boldsymbol{X}}_{\boldsymbol{1}} = \boldsymbol{X}_{\boldsymbol{2}} \\ \dot{\boldsymbol{X}}_{\boldsymbol{2}} = -\sigma_v \boldsymbol{U} + k_g \boldsymbol{g}(\boldsymbol{X}_{\boldsymbol{1}}, \boldsymbol{B}_\infty(t)) + \boldsymbol{f}_{\boldsymbol{u}}(t) \end{cases} \quad 5\text{-}1$$

The equation 3-31 can be refined as $\boldsymbol{g}(\boldsymbol{X}_{\boldsymbol{1}}, \boldsymbol{B}_\infty(t)) = 2\left(\frac{\partial(\boldsymbol{J}_c^T(\boldsymbol{X}_{\boldsymbol{1}})\boldsymbol{P})}{\partial \boldsymbol{X}_{\boldsymbol{1}}}\right)^T \boldsymbol{B}_\infty$. By adding a new variable to the state space equations and its derivative the new equations are introduced to be

$$\begin{cases} \dot{\boldsymbol{X}}_{\boldsymbol{1}} = \boldsymbol{X}_{\boldsymbol{2}} \\ \dot{\boldsymbol{X}}_{\boldsymbol{2}} = -\sigma_v \boldsymbol{U} + k_g(\boldsymbol{P}.\boldsymbol{\nabla})(\boldsymbol{J}_{\boldsymbol{c}}(\boldsymbol{X}_{\boldsymbol{1}})\boldsymbol{B}_\infty) + \boldsymbol{f}_{\boldsymbol{u}}(t) \\ \dot{\boldsymbol{P}} = \boldsymbol{J}_{\boldsymbol{c}}(\boldsymbol{X}_{\boldsymbol{1}})\boldsymbol{U}_{\boldsymbol{I}} + \dfrac{\boldsymbol{d}}{\boldsymbol{dt}}\left(\boldsymbol{J}_{\boldsymbol{c}}(\boldsymbol{X}_{\boldsymbol{1}})\right)\boldsymbol{B}_\infty \\ \dot{\boldsymbol{B}}_\infty = \boldsymbol{U}_{\boldsymbol{I}} \end{cases} \quad 5\text{-}2$$

$$\boldsymbol{Y} = \begin{cases} \boldsymbol{X}_{\boldsymbol{1}} \\ \boldsymbol{X}_{\boldsymbol{2}} \\ \boldsymbol{J}_{\boldsymbol{c}}(\boldsymbol{X}_{\boldsymbol{1}})\boldsymbol{B}_\infty \end{cases}$$

This transformation is offered for two main reasons. First, it provides the possibility of controlling the magnetization vector direction required in some micro devices navigation. Indeed, the uniform coils in the actuator structure bring around some independency in the system representation; thus, the magnetization vector is manipulated efficiently.

Before dealing with the controller design, one should investigate the basic characteristics of the system. A major feature of the system is whether it can reach a specified state from current state

called the system controllability. For the introduced electromagnetic system, the controllability simply defines the feasibility of moving a ferromagnetic particle between each two states in a working space. In order to expand the concept of the controllability, an accessibility relation is first outlined. In general, the state space is a smooth manifold, ($\boldsymbol{M}$), represented by countable local coordinate charts. Given a subset of state space, $\boldsymbol{U} \subseteq \boldsymbol{M}$, the state $\boldsymbol{X^1}$ is called U-accessible from the initial state $\boldsymbol{X_0}$ if a bounded measurable piecewise control vector can be found such that the corresponding system solution, $\boldsymbol{X}(t)$, satisfies $\boldsymbol{X}(t_0) = \boldsymbol{X_0}$, $\boldsymbol{X}(t_f) = \boldsymbol{X^1}$ and $\boldsymbol{X}(t) \subseteq \boldsymbol{U}$ during the period $t \in [t_0, t_f]$ [70].

Although accessibility relation is both reflexive and transitive, for nonlinear systems, it is not necessarily symmetric. A weaker relation can be defined which is a unique smallest equivalence relation on U. It contains all U-accessible pairs and is called weak U-accessibility. By this definition, $\boldsymbol{X^1}$ is weakly accessible from $\boldsymbol{X_0}$ iff there exists $\boldsymbol{X_0}, \boldsymbol{X_1}, \dots, \boldsymbol{X_k}$ such that $\boldsymbol{X^1} = \boldsymbol{X_k}$ and every two successive states have weak accessibility at least in one direction. The system is weakly controllable at a point if the weak accessible area from this point covers the whole state space manifold. However, this concept is global, and it may take a long time to reach a different state from current one. The system is called locally weakly controllable at each point, $\boldsymbol{X_0}$, if for its every neighborhood, the accessible area is still a neighborhood of $\boldsymbol{X_0}$. If the system is locally weakly controllable at each point of the state space, it is locally weakly controllable [70] .

Basically, a sufficient condition for a system to be locally weakly controllable is that it control Lie algebra construct a full rank distribution for every point in states space domain [54]. Given the control system of the form

$$\dot{\boldsymbol{X}} = \boldsymbol{f}(\boldsymbol{X}) + \sum_{i=1}^{m} \boldsymbol{g}_i(\boldsymbol{X}) u_i \tag{5-3}$$

the control Lie algebra is defined as the following set [69] :

$$\mathcal{C} = LC\left(\left\{\boldsymbol{\tau} \in V(\boldsymbol{M}) : \boldsymbol{\tau} = \left[\boldsymbol{\tau}_{\boldsymbol{i_k}}, \left[\boldsymbol{\tau}_{\boldsymbol{i_{k-1}}}, \dots, \left[\boldsymbol{\tau}_{\boldsymbol{i_2}}, \boldsymbol{\tau}_{\boldsymbol{i_1}}\right]\right]\right] : 1 \le i_k \le q, 1 \le k \le \infty\right\}\right) \tag{5-4}$$

where LC stands for linear combination, $V(\boldsymbol{M})$ is a vector space defined on $\boldsymbol{M}$, and $\boldsymbol{\tau}_1 = \boldsymbol{f}, \boldsymbol{\tau}_2 = \boldsymbol{g_1}, \dots, \boldsymbol{\tau}_q = \boldsymbol{g_m}$. Using the control Lie algebra, one can define the following distribution:

$$\Delta_{\mathcal{C}} = span\{\boldsymbol{\tau} : \boldsymbol{\tau} \in \mathcal{C}\} \tag{5-5}$$

The system is said to satisfy the controllability rank condition at $\boldsymbol{P_0}$ if

$$dim\, \Delta_{\mathcal{C}}(\boldsymbol{P_0}) = n \tag{5-6}$$

where *n* is the dimension of the state space. Satisfying the rank condition is a sufficient condition for the system to be locally weakly controllable. If the system is locally weakly controllable at every point, it is locally weakly controllable.

At this level, the controllability of the system introduced in equation (5-2) is investigated via the rank condition. By some mathematical calculation and considering the symmetry of the magnetic field gradient matrix, it can be proven that

$$(\boldsymbol{P}.\boldsymbol{\nabla})(\boldsymbol{J_c}(\boldsymbol{X_1})\boldsymbol{B}_\infty) = \boldsymbol{\nabla}(\boldsymbol{J_c}(\boldsymbol{X_1})\boldsymbol{B}_\infty)\boldsymbol{P} \tag{5-7}$$

$$\left(\frac{\boldsymbol{\partial}\left(\boldsymbol{J_c^T}(\boldsymbol{X_1})(\boldsymbol{J_c}(\boldsymbol{X_1})\boldsymbol{I})\right)}{\boldsymbol{\partial X_1}}\right)^{\boldsymbol{T}} = \left(\boldsymbol{\nabla}(\boldsymbol{J_c}(\boldsymbol{X_1})\boldsymbol{I})\boldsymbol{J_c}(\boldsymbol{X_1}) + \left(\boldsymbol{\nabla}\left(\boldsymbol{J_c}^{\boldsymbol{T}}(\boldsymbol{X_1})\boldsymbol{P}\right)\right)^{\boldsymbol{T}}\right) \tag{5-8}$$

In this case, the distribution $\Delta_{\mathcal{C}}$ takes the form

$$\Delta_{\mathcal{C}}(\boldsymbol{P_0}) = span\begin{Bmatrix} \boldsymbol{0_{3\times9}} & \boldsymbol{0_{3\times9}} & \beta_2\boldsymbol{M_J}(\boldsymbol{P_0}) & \boldsymbol{V_2}(\boldsymbol{P_0}) \\ \boldsymbol{0_{3\times9}} & \beta_1\boldsymbol{M_J}(\boldsymbol{P_0}) & \boldsymbol{V_1}(\boldsymbol{P_0}) & \boldsymbol{V_3}(\boldsymbol{P_0}) \\ \alpha\boldsymbol{J_c}(\boldsymbol{P_0}) & \boldsymbol{0_{3\times9}} & \boldsymbol{0_{3\times9}} & \beta_3\boldsymbol{J_{ct}}(\boldsymbol{X_1})\boldsymbol{M_J}(\boldsymbol{P_0}) \\ \boldsymbol{I_{9\times9}} & \boldsymbol{0_{9\times9}} & \boldsymbol{0_{9\times9}} & \boldsymbol{0_{9\times9}} \end{Bmatrix} \tag{5-9}$$

where $\boldsymbol{X_1}$ is the position vector, $\boldsymbol{P_0} = [\boldsymbol{X_1}; \boldsymbol{I}; \boldsymbol{P}]$, $\boldsymbol{V_1}, \boldsymbol{V_2}, \boldsymbol{V_3}$, some 3×9 matrices defined at $\boldsymbol{P_0}$, $\alpha, \beta_1, \beta_1, \beta_1$ are constant values, and $\boldsymbol{M_J}(\boldsymbol{P_0})$ and $\boldsymbol{J_{ct}}(\boldsymbol{X_1})$ are defined as:

$$\boldsymbol{M_J} = \left(\frac{\boldsymbol{\partial}\left(\boldsymbol{J_c^T}(\boldsymbol{X_1})(\boldsymbol{J_c}(\boldsymbol{X_1})\boldsymbol{I})\right)}{\boldsymbol{\partial X_1}}\right)^{\boldsymbol{T}}$$
$$\boldsymbol{J_{ct}}(\boldsymbol{X_1}) = \frac{\partial \sum_{j=1}^{3} \boldsymbol{J_{ci_j}}(\boldsymbol{X_1})}{\partial \boldsymbol{X_1}} \qquad i_1, i_2, i_3 \in \mathbb{N} \tag{5-10}$$

In practice, the system is locally weakly controllable if the actuator structure meets the following condition:

1) The $\boldsymbol{M_J}$ has full rank for all points in the working space.
2) For all points in the working space $\exists\ i_1, i_2, i_3$ such that $\boldsymbol{J_{ct}}$ has full rank.

In addition to being controllable, the system states should be detectable from the measured output vector. In the sense of observability, every two states should be distinguishable by a given piecewise constant control vector. Although the system controllability is necessary for manipulating the states, non-detectable states are out of control. When the system is not observable, it can be reduced to a smaller subsystem having the observability property. The main issue arising is the instability of the system due to its undetectable states in some cases; it is a property of the state space representation. The indistinguishable states lying on an output zeroing submanifold may disturb the performance when it comes to the trajectory tracking mission, in which the states are manipulated to track a predefined trajectory.

In order to introduce the required condition for precise tracking manipulation, the zero dynamics concept should be introduced first. A zero manifold is defined as a control invariant submanifold of $\boldsymbol{M}$ wherein the output vector remains zero for a specific smooth control vector. Given the zero manifold, one can define the zero dynamics as the restriction of the system dynamics to this manifold. In fact, the zero dynamics should be asymptotically stable at equilibrium point in order to provide the desired output regulation. In this case the system is called minimum phase [54], defined when it is possible to define a unique smooth control vector tangent to zero dynamics submanifold; this happens

in the case of invertible systems. In the next section, a trajectory tracking controller is designed and the effect of zero dynamics on tracking performance is discussed.

5.2 The system model modification

In this section, a controller is designed to stimulate a micro sized ferromagnetic particle movement in the aim of tracking a predefined trajectory. First, the state space representation should be modified in such a way that it appropriately simulates the actual system dynamics and is also simple. On this matter, the basic assumptions are initiated according to the relative importance of the applied forces on the ferromagnetic particle. In fact, the inertial forces are small enough to be ignored. Moreover, the particle mass is deniable, and thus no acceleration enters into the dynamical equations. Given these assumption, one can rewrite the state space representation of the system model in (5-2) as

$$\begin{cases} \dot{\boldsymbol{X_1}} = \bar{k}_g(\boldsymbol{P}.\boldsymbol{\nabla})(\boldsymbol{J_c}(\boldsymbol{X_1})\boldsymbol{B}_\infty) + \bar{\boldsymbol{f}}_{\boldsymbol{u}}(t) \\ \dot{\boldsymbol{P}} = \boldsymbol{J_c}(\boldsymbol{X_1})\boldsymbol{U_I} + \dfrac{\boldsymbol{d}}{\boldsymbol{dt}}\big(\boldsymbol{J_c}(\boldsymbol{X_1})\big)\boldsymbol{B}_\infty \\ \dot{\boldsymbol{B}}_\infty = \boldsymbol{U_I} \end{cases} \quad 5\text{-}11$$

In these equations, the magnetization vector can be removed from the equations whenever the alignment of the micro device is not critical in the navigation process. Spherical coordinates are offered when the micro device alignment needs to be set along the predefined path. In this way, the variation of the magnetization vector is divided into the magnitude change and direction change.

In this project, a micro particle is supposed to follow a predefined path with a velocity of constant magnitude. Therefore, the output vector can be simply assumed to be the position vector of the particle, and further modification is required on the system state space representation. The aim is to find a model whose number of inputs is the same as number of outputs such that every input is only connected to an output component. In other words, the outputs need to be independently connected to inputs through some dynamical equations. For this reason, a diffeomorphic mapping should be defined to provide the desired representation for the system. First, the connection between an output component and the input vector is labeled by an integer number called a relative degree. A vector relative degree $\{r_1, \dots, r_m\}$ exists for a multivariable system if at point $\boldsymbol{P_0}$

$$L_{\boldsymbol{g}_j} L_{\boldsymbol{f}}^{k} h_i(\boldsymbol{P}) = 0 \quad 5\text{-}12$$

for all $1 \le j \le m, k < r_i - 1, 1 \le i \le m$, and for every $\boldsymbol{P}$ in a neighbor of $\boldsymbol{P_0}$. Moreover, the following $m \times m$ matrix, $A(\boldsymbol{P})$, has to be nonsingular at $\boldsymbol{P} = \boldsymbol{P_0}$. This matrix is called characteristic matrix [69].

$$A(\boldsymbol{P}) = \begin{pmatrix} L_{\boldsymbol{g_1}} L_{\boldsymbol{f}}^{r_1-1} h_1(\boldsymbol{P}) & \dots & L_{\boldsymbol{g_m}} L_{\boldsymbol{f}}^{r_1-1} h_1(\boldsymbol{P}) \\ L_{\boldsymbol{g_1}} L_{\boldsymbol{f}}^{r_2-1} h_2(\boldsymbol{P}) & \cdots & L_{\boldsymbol{g_m}} L_{\boldsymbol{f}}^{r_2-1} h_2(\boldsymbol{P}) \\ \dots & \dots & \dots \\ L_{\boldsymbol{g_1}} L_{\boldsymbol{f}}^{r_m-1} h_m(\boldsymbol{P}) & \dots & L_{\boldsymbol{g_m}} L_{\boldsymbol{f}}^{r_m-1} h_m(\boldsymbol{P}) \end{pmatrix} \quad 5\text{-}13$$

These conditions can also be achieved by differentiating each output component since the input vector shows up in the succeeding differential equation. Assuming the input vector to be the time derivative of currents, one can find

$$\begin{cases} \dot{\boldsymbol{X}}_{\boldsymbol{1}} = \boldsymbol{X}_{\boldsymbol{2}} \\ \dot{\boldsymbol{X}}_{\boldsymbol{1}} = \bar{k}_g \left(\boldsymbol{\nabla} \left(\frac{d}{dt} \boldsymbol{J_c}(\boldsymbol{X}_{\boldsymbol{1}}) \boldsymbol{I} \right) \boldsymbol{P} + \boldsymbol{\nabla} (\boldsymbol{J_c}(\boldsymbol{X}_{\boldsymbol{1}}) \boldsymbol{I}) \left(\frac{d}{dt} \boldsymbol{J_c}(\boldsymbol{X}_{\boldsymbol{1}}) \right) \boldsymbol{I} \right) + \\ \qquad \bar{k}_g \left(\boldsymbol{\nabla} (\boldsymbol{J_c}(\boldsymbol{X}_{\boldsymbol{1}}) \boldsymbol{I}) \boldsymbol{J_c}(\boldsymbol{X}_{\boldsymbol{1}}) + \left(\boldsymbol{\nabla} \left(\boldsymbol{J_c}^{\boldsymbol{T}} (\boldsymbol{X}_{\boldsymbol{1}}) \boldsymbol{P} \right) \right)^{\boldsymbol{T}} \right) \boldsymbol{U_I} + \bar{\boldsymbol{f}}_{\boldsymbol{u}}(t) \\ \dot{\boldsymbol{B}}_{\infty} = \boldsymbol{U_I} \end{cases} \quad 5\text{-}14$$

At this point, the new input vector is introduced by the following mapping:

$$\boldsymbol{V} = \bar{k}_g \left(\boldsymbol{\nabla} (\boldsymbol{J_c}(\boldsymbol{X}_{\boldsymbol{1}}) \boldsymbol{I}) \boldsymbol{J_c}(\boldsymbol{X}_{\boldsymbol{1}}) + \left(\boldsymbol{\nabla} \left(\boldsymbol{J_c}^{\boldsymbol{T}} (\boldsymbol{X}_{\boldsymbol{1}}) \boldsymbol{P} \right) \right)^{\boldsymbol{T}} \right) \boldsymbol{U_I} \quad 5\text{-}15$$

The controllability first condition implies the existence of the vector $\boldsymbol{U_I}$ for every given input vector $\boldsymbol{V}$. By this transformation the characteristic matrix is an identity matrix of dimension 3×3 and the relative rank is 2 for every output component. If the matrix $\boldsymbol{M_J}$ is nonsingular, there exists more than one solution to the vector $\boldsymbol{U_I}$ and some optimization method is required to unify the solution. Besides, precise trajectory tracking necessitates asymptotically stable zero dynamics around the reference trajectory. On the other hand, the zero dynamics should be linear with respect to the input vector $\boldsymbol{V}$ for a theoretical reason explained in the next sections. Given all these requirements, the cost function is defined as

$$Cf = \frac{1}{2} \boldsymbol{U_I^T U_I} + \boldsymbol{I^T K_I U_I} + \boldsymbol{\lambda^T} \left(\bar{k}_g \boldsymbol{M_J U_I} - \boldsymbol{V} \right)$$

where $\boldsymbol{K_I}$ is a symmetric Hurwitz matrix, and $\boldsymbol{\lambda}$ is the vector of Lagrange coefficients. The first term in the right hand side of (5-15) guarantee the boundary on the required solution. The second term implies the different direction for the current vector and its time derivative. The optimal vector $\boldsymbol{U_I}$ is achieved as

$$\boldsymbol{U_I} = \left(\boldsymbol{K_I M_J^T} \left(\boldsymbol{M_J M_J^T} \right)^{-1} \boldsymbol{M_J} - \boldsymbol{K_I} \right) \boldsymbol{I} + \frac{1}{\bar{k}_g} \boldsymbol{M_J^T} \left(\boldsymbol{M_J M_J^T} \right)^{-1} \boldsymbol{V} \quad 5\text{-}16$$

All in all, the state space representation has three inputs as well as three outputs in which every output is independently connected to an input via its corresponding differential equation. Moreover, the representation contains the current vector dynamics constituting the zero dynamics.

5.3 The control design

The problem of asymptotically tracking, (rejecting) a desired trajectory (unwanted disturbances), is one of the challenging concepts in control theory. It is often assumed that a dynamical system called

an exosystem generates the reference and/or the disturbance signal which must be tracked and/or rejected. The controller is designed to incorporate the constructed internal model of the exosystem and is an interconnection of two parallel connected components, the servo compensator and the stabilizing compensator. While the former component generates the control inputs needed to impose the prescribed asymptotic tracking (rejecting), the latter one stabilizes the final closed loop system. Moreover, the robust regulation problem in the presence of parametric uncertainties ranging within a compact set is addressed.

However, the reference signal might be unknown in advance and thus the exosystem parameter. An internal-model based control is required wherein the natural frequencies of the internal model are automatically tuned to match a totally unknown exosystem. This scheme should provide asymptotic tracking when the reference signal is not known but can be expressed as the weighted summation of a finite number of sinusoidal functions with different phase values; furthermore, the exosystem is assumed to be a linear dynamical system generating the sinusoidal functions. An efficient approach is introduced by A. Serrani et al [42]. for a single-input, single-output finite-dimensional nonlinear system. In this project, the same approach is used to extend the results of the output regulation problem in the existence of parametric uncertainties on the plant and unknown frequencies of the linear exosytem to a specific class of multi-input multi-output nonlinear system.

The nonlinear systems considered in this section have the general form

$$\begin{cases} \dot{\boldsymbol{X}} = \boldsymbol{f}(\boldsymbol{X}, \boldsymbol{w}, \boldsymbol{\mu}) + \boldsymbol{g}(\boldsymbol{X}, \boldsymbol{w}, \boldsymbol{\mu})\boldsymbol{U} \\ \boldsymbol{y} = \boldsymbol{h}(\boldsymbol{X}, \boldsymbol{w}, \boldsymbol{\mu}) \end{cases} \quad 5\text{-}17$$

with state vector $\boldsymbol{X} \in \mathbb{R}^n$, control input $\boldsymbol{U} \in \mathbb{R}^m$, and output $\boldsymbol{y} \in \mathbb{R}^m$. The system includes a vector of unknown parameters $\boldsymbol{\mu} \in \mathbb{R}^p$, and its values range over a known compact set $\mathcal{P}$ containing the origin. The vector fields *f*, and *g* and the output map are assumed to be smooth and $\boldsymbol{f}(0,0,\boldsymbol{\mu}) = 0$, $\boldsymbol{h}(0,0,\boldsymbol{\mu}) = 0$. The exosystem is a neutrally stable linear time-invariant system of the form:

$$\dot{\boldsymbol{w}} = \boldsymbol{S}(\boldsymbol{\sigma})\boldsymbol{w} \quad 5\text{-}18$$

The regulated error is thus defined as

$$\boldsymbol{e} = \boldsymbol{y} - \boldsymbol{q}(\boldsymbol{w}, \boldsymbol{\mu})$$

where $\boldsymbol{q}(\boldsymbol{w}, \boldsymbol{\mu})$ is a smooth function of its arguments. The concerned control input is an error feedback controller modelled as

$$\begin{cases} \dot{\boldsymbol{\xi}} = \boldsymbol{\Lambda}(\boldsymbol{\xi}, \boldsymbol{e}) \\ \boldsymbol{U} = \boldsymbol{\Theta}(\boldsymbol{\xi}) \end{cases} \quad 5\text{-}19$$

with smooth functions $\boldsymbol{\Lambda}$, and $\boldsymbol{\Theta}$. The main concern of the output regulation problem is to design a controller of form (5-19) defined on a compact set, $\boldsymbol{\xi} = \boldsymbol{\mathcal{K}_\xi}$ for any given fixed compact sets $\boldsymbol{X} = \boldsymbol{\mathcal{K}_X}, \boldsymbol{w} = \boldsymbol{\mathcal{K}_w}$ such that:

1. the equilibrium of the unforced closed loop system

$$\begin{cases}\dot{\boldsymbol{X}} = \boldsymbol{f}(\boldsymbol{X},\boldsymbol{0},\boldsymbol{\mu}) + \boldsymbol{g}(\boldsymbol{X},\boldsymbol{0},\boldsymbol{\mu})\boldsymbol{\Theta}(\boldsymbol{\xi}) \\ \dot{\boldsymbol{\xi}} = \boldsymbol{\Lambda}\big(\boldsymbol{\xi},\boldsymbol{h}(\boldsymbol{X},\boldsymbol{0},\boldsymbol{\mu})\big)\end{cases}$$

is asymptotically stable for every $\boldsymbol{\mu} \in \mathcal{P}$, with domain of attraction containing the set $\boldsymbol{\mathcal{K}_x} \times \boldsymbol{\mathcal{K}_\xi}$,

2. the trajectory of the closed-loop system

$$\begin{cases}\dot{\boldsymbol{X}} = \boldsymbol{f}(\boldsymbol{X},\boldsymbol{w},\boldsymbol{\mu}) + \boldsymbol{g}(\boldsymbol{X},\boldsymbol{w},\boldsymbol{\mu})\boldsymbol{\Theta}(\boldsymbol{\xi}) \\ \dot{\boldsymbol{\xi}} = \boldsymbol{\Lambda}\big(\boldsymbol{\xi},\boldsymbol{h}(\boldsymbol{X},\boldsymbol{w},\boldsymbol{\mu}) - \boldsymbol{q}(\boldsymbol{w},\boldsymbol{\mu})\big) \\ \dot{\boldsymbol{w}} = \boldsymbol{S}(\boldsymbol{\sigma})\boldsymbol{w}\end{cases}$$

is defined for all initial conditions, is bounded and satisfies the condition $\lim_{t\to\infty} \boldsymbol{e}(t) = 0$.

The regulation problem limited to a specific class of time invariant nonlinear systems is adapted in the rest of the report.

One of the necessary assumptions needed for the problem to be well-posed is the type of studied systems. The class of considered systems are limited to those modeled by differential equations of form (5-17) and are globally diffeomorphic to a system of the form

$$\begin{cases}\dot{x}_1^i = x_2^i \\ \vdots \\ \dot{x}_{r_i-1}^i = x_{r_i}^i \\ \dot{x}_{r_i}^i = f_r^i(\boldsymbol{z},\boldsymbol{X},\boldsymbol{w},\boldsymbol{\mu}) + b^i(\boldsymbol{\mu})v_i \\ \dot{\boldsymbol{z}} = \boldsymbol{f_0}(\boldsymbol{z},\boldsymbol{X},\boldsymbol{w},\boldsymbol{\mu}) + \boldsymbol{C}(\boldsymbol{z},\boldsymbol{X},\boldsymbol{w},\boldsymbol{\mu})\boldsymbol{v} \\ y_i = x_1^i\end{cases} \qquad 5\text{-}20$$

where = 1, … , m , $\boldsymbol{X} = col\big(\boldsymbol{x^1},\boldsymbol{x^2},\cdots,\boldsymbol{x^m}\big)$, $b^i(\mu) > 0$ and the regulated errors are defined as

$$e_i = y_i - q_i(\boldsymbol{w},\boldsymbol{\mu}) \qquad 5\text{-}21$$

Assumption 5.1: For every $\boldsymbol{\sigma} \in \mathcal{P}$, there exists a globally defined solution $\boldsymbol{\zeta_\sigma}(\boldsymbol{w},\boldsymbol{\mu})$ to the equation

$$\frac{\partial \boldsymbol{\zeta_\sigma}(\boldsymbol{w},\boldsymbol{\mu})}{\partial \boldsymbol{w}}\boldsymbol{S}(\boldsymbol{\sigma})\boldsymbol{w} = \boldsymbol{f_0}(\boldsymbol{\zeta_\sigma}(\boldsymbol{w},\boldsymbol{\mu}),\overline{\boldsymbol{\vartheta}}_{\boldsymbol{\sigma}},\boldsymbol{w},\boldsymbol{\mu}) + \boldsymbol{C}(\boldsymbol{\zeta_\sigma}(\boldsymbol{w},\boldsymbol{\mu}),\overline{\boldsymbol{\vartheta}}_{\boldsymbol{\sigma}},\boldsymbol{w},\boldsymbol{\mu})\boldsymbol{c_\sigma}(\boldsymbol{w},\boldsymbol{\mu}) \qquad 5\text{-}22$$

where $\overline{\boldsymbol{\vartheta}}_{\boldsymbol{\sigma}} = col\big(\boldsymbol{\vartheta_\sigma^1},\boldsymbol{\vartheta_\sigma^2},\ldots,\boldsymbol{\vartheta_\sigma^m}\big)$, and $\boldsymbol{\vartheta_\sigma^i}$'s are globally defined mappings

$$\boldsymbol{\vartheta_\sigma^i}(\boldsymbol{w},\boldsymbol{\mu}) = \begin{pmatrix} q^i(\boldsymbol{w},\boldsymbol{\mu}) \\ L_{\boldsymbol{S(\sigma)w}}q^i(\boldsymbol{w},\boldsymbol{\mu}) \\ \vdots \\ L_{\boldsymbol{S(\sigma)w}}^{r_i-1}q^i(\boldsymbol{w},\boldsymbol{\mu}) \end{pmatrix}$$

and

$$c_\sigma^i(\boldsymbol{w},\boldsymbol{\mu}) = \frac{1}{b^i(\boldsymbol{\mu})}\Big[L_{\boldsymbol{S(\sigma)w}}^{r_i}q^i(\boldsymbol{w},\boldsymbol{\mu}) - f_r^i(\boldsymbol{\zeta_\sigma}(\boldsymbol{w},\boldsymbol{\mu}),\overline{\boldsymbol{\vartheta}}_{\boldsymbol{\sigma}}(\boldsymbol{w},\boldsymbol{\mu}),\boldsymbol{w},\boldsymbol{\mu})\Big]$$

The existence of these mapping is required to find a robust output regulation controller.

Assumption 5.2: For $1 \leq i \leq m$, $q_i \in \mathbb{N}$ and a set of real numbers $a_0^i(\boldsymbol{\sigma}), a_1^i(\boldsymbol{\sigma}), \cdots, a_{q_i-1}^i(\boldsymbol{\sigma})$ can be chosen to satisfy the equality

$$L_{\boldsymbol{S}(\boldsymbol{\sigma})\boldsymbol{w}}^{r_i} c_\sigma^i(\boldsymbol{w},\boldsymbol{\mu}) = a_0^i(\boldsymbol{\sigma}) c_\sigma^i(\boldsymbol{w},\boldsymbol{\mu}) + a_1^i(\boldsymbol{\sigma}) L_{\boldsymbol{S}(\boldsymbol{\sigma})\boldsymbol{w}} c_\sigma^i(\boldsymbol{w},\boldsymbol{\mu}) + \cdots + a_{q_i-1}^i(\boldsymbol{\sigma}) L_{\boldsymbol{S}(\boldsymbol{\sigma})\boldsymbol{w}}^{q_i-1} c_\sigma^i(\boldsymbol{w},\boldsymbol{\mu}) \quad 5\text{-}23$$

An important concept must be introduced at this point. Let the autonomous system of the form

$$\begin{cases} \dot{\boldsymbol{x}} = \boldsymbol{f}(\boldsymbol{x}) \\ \boldsymbol{y} = \boldsymbol{h}(\boldsymbol{x}) \end{cases}$$

be denoted by $\{\mathcal{X}, \boldsymbol{f}, \boldsymbol{h}\}$ with state vector $\boldsymbol{x} \in \mathcal{X}$ and output vector $\boldsymbol{y} \in \mathbb{R}^m$ It is assumed that $\boldsymbol{f}$ is a smooth vector field and $\boldsymbol{h}$ is a smooth mapping having the property $\boldsymbol{f}(\boldsymbol{0}) = \boldsymbol{0}$ and $\boldsymbol{h}(\boldsymbol{0}) = \boldsymbol{0}$.

Definition 5.1[41]*:* A system with representation $\{\mathcal{X}, \boldsymbol{f}, \boldsymbol{h}\}$ is called immersed into a different system with representation $\{\mathcal{X}', \boldsymbol{f}', \boldsymbol{h}'\}$ if a smooth mapping $\boldsymbol{\tau}: \mathcal{X} \to \mathcal{X}'$ can be defined such that $\boldsymbol{\tau}(\boldsymbol{0}) = \boldsymbol{0}$ and $\boldsymbol{h}(\boldsymbol{x}) \neq \boldsymbol{h}(\boldsymbol{x}') \Rightarrow \boldsymbol{h}'\big(\boldsymbol{\tau}(\boldsymbol{x})\big) \neq \boldsymbol{h}'\big(\boldsymbol{\tau}(\boldsymbol{x}')\big)$. The mapping also satisfies

$$\begin{cases} \dfrac{\partial \boldsymbol{\tau}}{\partial \boldsymbol{x}} \boldsymbol{f}(\boldsymbol{x}) = \boldsymbol{f}'\big(\boldsymbol{\tau}(\boldsymbol{x})\big) \\ \boldsymbol{h}(\boldsymbol{x}) = \boldsymbol{h}'\big(\boldsymbol{\tau}(\boldsymbol{x})\big) \end{cases}$$

for all $\boldsymbol{x} \in \mathcal{X}$.

Now, the purpose of assumption 5.2 can be illustrated. In fact, it implies that for every fixed value for the exosystem parameters, the mapping

$$\boldsymbol{\tau}_\sigma^i(\boldsymbol{w},\boldsymbol{\mu}) = \begin{pmatrix} c_\sigma^i(\boldsymbol{w},\boldsymbol{\mu}) \\ L_{\boldsymbol{S}(\boldsymbol{\sigma})\boldsymbol{w}} c_\sigma^i(\boldsymbol{w},\boldsymbol{\mu}) \\ \vdots \\ L_{\boldsymbol{S}(\boldsymbol{\sigma})\boldsymbol{w}}^{q_i-1} c_\sigma^i(\boldsymbol{w},\boldsymbol{\mu}) \end{pmatrix} \quad 5\text{-}24$$

exists and defines an immersion between

$$\begin{cases} \dot{\boldsymbol{w}} = \boldsymbol{S}(\boldsymbol{\sigma})\boldsymbol{w} \\ \dot{\boldsymbol{\mu}} = \boldsymbol{0} \\ v_i = c_\sigma^i(\boldsymbol{w},\boldsymbol{\mu}) \end{cases} \quad 5\text{-}25$$

and the linear observable system

$$\begin{cases} \dot{\boldsymbol{\eta}}^i = \boldsymbol{\Phi}^i(\boldsymbol{\sigma})\boldsymbol{\eta}^i \\ v_i = \boldsymbol{\Gamma}^i \boldsymbol{\eta}^i \end{cases} \quad 5\text{-}26$$

where $\boldsymbol{\Gamma}^i = (1 \quad 0 \quad 0 \quad \ldots \quad 0)_{1\times q_i}$, and

$$\boldsymbol{\Phi}^i(\boldsymbol{\sigma}) = \begin{pmatrix} 0 & 1 & 0 & \cdots & 0 \\ 0 & 0 & 1 & \cdots & 0 \\ \vdots & \vdots & \vdots & \ddots & \vdots \\ 0 & 0 & 0 & \cdots & 1 \\ a_0^i(\boldsymbol{\sigma}) & (\boldsymbol{\sigma})a_1^i & a_2^i(\boldsymbol{\sigma}) & \cdots & a_{q_i-1}^i(\boldsymbol{\sigma}) \end{pmatrix}$$

Without loss of generality, $\left(\boldsymbol{\Phi}^i(\boldsymbol{\sigma}), \boldsymbol{\Gamma}^i\right)$ can be chosen such that the characteristic polynomial of $\boldsymbol{\Phi}^i(\boldsymbol{\sigma})$ has all its eigenvalues on imaginary axis since (5-26) is the immersion of a neutrally stable exosystem. Moreover, the spectrum of $\boldsymbol{\Phi}^i(\boldsymbol{\sigma})$ must contain the eigenvalues of the exosystem as well as the eigenvalues which are multiples of the exosystem eigenvalues. This is required due to the nonlinearity of the plant which may generate a number of higher order harmonics.

5.3.1 Mathematical preliminaries

Before expanding the main controller design, some mathematical preliminaries on stability analysis need to be discussed. The initial definitions on and conditions for a system stability are demonstrated in the current subsection. In order to proceed, a number of critical Lemma's are extended which will be employed in the next subsections to prove the stability of the closed loop system.

Definition 5.2: A continuous function $\alpha: [0, a] \to \mathbb{R}^+$ is said to belong to class-*K* if it is

1. Strictly increasing,
2. $\alpha(0) = 0$.

The function α belongs to class-K_∞ if

3. $a = \infty$,
4. $\alpha(r) \to \infty$ as $r \to \infty$.

Definition 5.3: A continuous function $\beta: [0, a] \times \mathbb{R}^+ \to \mathbb{R}^+$ is said to belong to class-*KL* if it satisfies the following two conditions:

1. For every fixed $s \in \mathbb{R}^+$, the function $\begin{matrix} \alpha: [0, a] \to \mathbb{R}^+ \\ r \mapsto \beta(r, s) \end{matrix}$ belongs to class-K,
2. For every fixed $r \in [0, a]$, the function $\begin{matrix} \gamma: \mathbb{R}^+ \to \mathbb{R}^+ \\ s \mapsto \beta(r, s) \end{matrix}$ is strictly decreasing,

   and $\gamma \to 0$ as $s \to \infty$.

Definition 5.4: Assume the closed loop system is represented as

$$\dot{\boldsymbol{x}} = \boldsymbol{f}(\boldsymbol{x}, \boldsymbol{w}(t), \boldsymbol{\mu}) \qquad 5\text{-}27$$

where $\boldsymbol{x} \in \mathbb{R}^n$ and $\boldsymbol{f}$ is a smooth vector field. Moreover, $\boldsymbol{w}(t)$ is the exosystem solution of (5-25) when the initial condition $\boldsymbol{w}_0$ ranges on some open set $\mathcal{W} \subset \mathbb{R}^d$, and $(\boldsymbol{\mu}, \boldsymbol{\sigma}) \in \mathcal{P} \times \Sigma$. It is assumed that $\boldsymbol{f}(\boldsymbol{0}, \boldsymbol{w}, \boldsymbol{\mu}) = \boldsymbol{0}$ for all $\boldsymbol{w}$ and all $\boldsymbol{\mu}$. The system is called uniformly asymptotically stable around $\boldsymbol{x} = \boldsymbol{0}$ if a positive real number r and a class-KL function $\beta(.,.)$ can be independently defined from $\boldsymbol{w}_0$, $\boldsymbol{\mu}$ and $\boldsymbol{\sigma}$, such that

$$\|\boldsymbol{x}(t)\| \leq \beta(\|\boldsymbol{x}(0)\|, t)$$

in forward time and while $\boldsymbol{x}(0) \in \mathcal{B}_r$ ($\mathcal{B}_r$ is an open set with radius r centered at $\boldsymbol{x}(0)$). The equilibrium point is said to be uniformly exponentially stable if

$$\beta(\|\boldsymbol{x}(0)\|, t) = \kappa\|\boldsymbol{x}(0)\|e^{-\lambda t}$$

for some positive κ, λ which are independent of $\boldsymbol{w}_0$, $\boldsymbol{\mu}$ and $\boldsymbol{\sigma}$.

Lemma 5.1: Consider the system in (5-27). Assume that the equilibrium point $\boldsymbol{x} = \boldsymbol{0}$ is asymptotically stable, for every initial conditions $\boldsymbol{w}_0$ ranging over some fixed compact set, and also every $(\boldsymbol{\sigma}, \boldsymbol{\mu})$ in a compact set. Suppose that the domain of attraction $\mathcal{D}$ of $\boldsymbol{x} = \boldsymbol{0}$ contains a fixed open and connected set which contains the origin, for any $\boldsymbol{w}_0 \in \mathcal{K}_w$ and any $(\boldsymbol{\sigma}, \boldsymbol{\mu}) \in \mathcal{K}_\sigma \times \mathcal{K}_\mu$. Then, the origin is uniformly asymptotically stable.

Employing this Lemma, one can come up with

Corollary 5.1: Suppose that the set $\mathcal{D}$ defined in Lemma 5.1 is positively invariant under the flow of (5-27), in addition to the assumptions of this Lemma. If a diffeomorphism $\boldsymbol{\Phi}: \mathcal{D} \to \mathbb{R}^n$ preserving the origin can be defined, there exists a smooth positive definite function V proper on $\mathcal{D}$ and which satisfies

$$\frac{\partial V}{\partial \boldsymbol{x}} f(\boldsymbol{x}, \boldsymbol{w}(t), \boldsymbol{\mu}) < -\alpha(\boldsymbol{x}) \qquad 5\text{-}28$$

for any $\boldsymbol{x} \in \mathcal{D}$, $\boldsymbol{w_0} \in \mathcal{K}_w$, and $(\boldsymbol{\sigma}, \boldsymbol{\mu}) \in \mathcal{K}_\sigma \times \mathcal{K}_\mu$ where $\alpha(\boldsymbol{x})$ is a smooth positive definite function.

The Lyapunov approach is utilized in the rest of this section to improve a dynamic output feedback stabilizer. First, a dynamical equation is considered for the controller whose input is the tracking error and output is the feedback controller. The main concern is to find the involved coefficients due to either coordinates transformation or constituting feedback stabilizer. In order to find proper coefficients, the closed loop system is divided into subsystems for which the Lyapunov functions are selected. Preserving the Lyapunov function properties is how the coefficients are derived; this scheme is categorized as backstepping methods. The basic backstepping tools are introduced in [53] and are extended to multi variable system in the following paragraphs.

Lemma 5.2: Consider a compact set $\mathcal{S}$ in the product space $\mathbb{R}^m \times \mathbb{R}^n$. Let $\mathcal{S}_z$ and $\mathcal{S}_x$ be its respective projections (i.e., $\mathcal{S} \subset \mathcal{S}_z \times \mathcal{S}_x$). Let $\chi(\boldsymbol{z})$ be a continuous real function on $\mathcal{S}_z$ and be positive definite on the projection of the set $\{(\boldsymbol{z}, \boldsymbol{x}): \boldsymbol{x} = \boldsymbol{0}\} \cap \mathcal{S}$. Let $\psi(\boldsymbol{x})$ be a continuous real function on $\mathcal{S}_x$ and be positive definite on $\mathcal{S}_x \backslash \{\boldsymbol{0}\}$ as well as $\varphi(\boldsymbol{z}, \boldsymbol{x}, \boldsymbol{d})$ be a continuous real function on $\mathcal{S} \times \mathcal{D}$ satisfying $\varphi(\boldsymbol{z}, \boldsymbol{x}, \boldsymbol{d}) = \boldsymbol{0}$ for all $(\boldsymbol{z}, \boldsymbol{x}, \boldsymbol{d}) \in (\{(\boldsymbol{z}, \boldsymbol{x}): \boldsymbol{x} = \boldsymbol{0}\} \cap \mathcal{S}) \times \mathcal{D}$. Let κ be a function of class-K_∞. Provided these conditions, a positive real number K_* exists such that, for all $K \geq K_*$ and all $(\boldsymbol{z}, \boldsymbol{x}, \boldsymbol{d}) \in \mathcal{S} \times \mathcal{D}$,

$$-\chi(\boldsymbol{z}) - \kappa(K)\psi(\boldsymbol{x}) + \varphi(\boldsymbol{z}, \boldsymbol{x}, \boldsymbol{d}) < 0 \qquad 5\text{-}29$$

In the rest of this subsection the following assumption is required to be made.

Assumption 5.3: this assumption is called ULP assumption, which stands for uniformly Lyapunov property. Let start with the system of the form

$$\dot{\boldsymbol{z}} = \boldsymbol{h}\big(\boldsymbol{z}, \boldsymbol{0}, \boldsymbol{d}(t)\big)$$

It is assumed that there exists an open set $\mathcal{U}_1$ in $\mathbb{R}^m$, a nonnegative real number $\nu < 1$, a real number $c \geq 1$, and a diffeomorphic function $V: \mathcal{U}_1 \to \mathbb{R}^+$ such that the set $\{\boldsymbol{z}: \nu < V(\boldsymbol{z}) \leq c + 1\}$ is a compact subset of $\mathcal{U}_1$, and the function V satisfies $\dot{V} \leq -\mathrm{O}_1(\boldsymbol{z})$ where $\mathrm{O}_1(\boldsymbol{z})$ is continuous on $\mathcal{U}_1$ and positive definite on $\{\boldsymbol{z}: \nu < V(\boldsymbol{z}) \leq c + 1\}$.

At this point we are ready to introduce the first backstepping tool. In this Lemma, the derivative of the control is used instead of the control itself.

Lemma 5.3: Let the nonlinear system be diffeomorphic and of the form

$$\begin{cases} \dot{\boldsymbol{z}} = \boldsymbol{h}\big(\boldsymbol{z}, \boldsymbol{x}, \boldsymbol{d}(t)\big) \\ \dot{x}_1 = x_2 + f_1\big(\boldsymbol{z}, \boldsymbol{x}, \boldsymbol{d}(t)\big) \\ \dot{x}_2 = x_3 + f_2\big(\boldsymbol{z}, \boldsymbol{x}, \boldsymbol{d}(t)\big) \\ \vdots \\ \dot{x}_{j-1} = x_j + f_{j-1}\big(\boldsymbol{z}, \boldsymbol{x}, \boldsymbol{d}(t)\big) \\ \dot{x}_j = u + f_j\big(\boldsymbol{z}, \boldsymbol{x}, \boldsymbol{d}(t)\big) \end{cases}$$

where $\boldsymbol{x} = col\big(x_1, \dots, x_j\big) \in \mathbb{R}^j$, $\boldsymbol{z} \in \mathbb{R}^m$. Let ULP assumption be held and the polynomial

$$p(s) = s^j + a_j s^{j-1} + \cdots + a_1$$

be Hurwitz. Let the matrix $\boldsymbol{A_c}$ be the companion form corresponding to $p(s)$. Moreover, assume $\boldsymbol{P_c}$ solve the matrix equation $\boldsymbol{A_c^T P_c} + \boldsymbol{P_c A_c} = -\boldsymbol{I}$. First, the variable $\xi_i = {x_i}/{K^{i-1}}$ is defined, for a must be defined parameter $K \geq 1$ and $i = 1, \dots, j$. In new coordinate system $\boldsymbol{\xi} = col\big(\xi_1, \dots, \xi_j\big)$, let $\boldsymbol{h}(.,.,.)$ is bounded by a continuous function $\widehat{\boldsymbol{h}}(\boldsymbol{z}, \boldsymbol{\xi}, \boldsymbol{d})$ as well as $f_i(.,.,.)$ by continuous function $\hat{f}_i(\boldsymbol{z}, \boldsymbol{\xi}, \boldsymbol{d})$.Next, for some given $\mu \geq 1$, the Lyapunov function is defined as

$$W(\boldsymbol{z}, \boldsymbol{\xi}) = c\frac{V}{c + 1 - V} + \mu\frac{\boldsymbol{\xi^T P_c \xi}}{\mu + 1 - \boldsymbol{\xi^T P_c \xi}} \qquad 5\text{-}30$$

In addition, we define the set $\mathcal{U}_2 = \{\boldsymbol{z}: V(\boldsymbol{z}) < c + 1\} \times \{\boldsymbol{\xi}: \boldsymbol{\xi^T P_c \xi} < \mu + 1\}$. Under these conditions, the function $W(\boldsymbol{z}, \boldsymbol{\xi}): \mathcal{U}_2 \to \mathbb{R}^+$ is proper on $\mathcal{U}_2$ and if the control is chosen as

$$u = -K^j\big(a_1\xi_1 + \cdots + a_j\xi_j\big) \qquad 5\text{-}31$$

for each strictly positive real number ρ, a positive real number $K_* \geq 1$ can be found such that, for all $K > K_*$, W satisfies $\dot{W} \leq -\mathrm{O}_2(\boldsymbol{z}, \boldsymbol{\xi})$ where $\mathrm{O}_2(\boldsymbol{z}, \boldsymbol{\xi})$ is continuous on $\mathcal{U}_2$ and positive definite on $\{(\boldsymbol{z}, \boldsymbol{\xi}): \rho + \nu < W(\boldsymbol{z}, \boldsymbol{\xi}) \leq \mu^2 + c^2 + 1\}$.

Proof: By applying the offered control in and coordinate transformation, the closed loop system takes the form

$$\begin{cases}\dot{\boldsymbol{z}} = \boldsymbol{h}\left(\boldsymbol{z}, \bar{\boldsymbol{\xi}}, \boldsymbol{d}(t)\right) \\ \dot{\boldsymbol{\xi}} = K\boldsymbol{A_c}\boldsymbol{\xi} + \boldsymbol{F_K}\left(\boldsymbol{z}, \bar{\boldsymbol{\xi}}, \boldsymbol{d}(t)\right)\end{cases}$$

where $\bar{\boldsymbol{\xi}} = col\left(\xi_1, K\xi_2, \dots, K^{j-1}\xi_j\right)$, and

$$\boldsymbol{F_K} = \begin{pmatrix} f_1\left(\boldsymbol{z}, \bar{\boldsymbol{\xi}}, \boldsymbol{d}(t)\right) \\ \frac{1}{K} f_2\left(\boldsymbol{z}, \bar{\boldsymbol{\xi}}, \boldsymbol{d}(t)\right) \\ \vdots \\ \frac{1}{K^{j-1}} f_j\left(\boldsymbol{z}, \bar{\boldsymbol{\xi}}, \boldsymbol{d}(t)\right) \end{pmatrix}$$

The derivative of the Lyapunov function W is calculated as

$$\dot{W} = \frac{c(c+1)}{(c+1-V)^2}\dot{V} + \frac{\mu(\mu+1)}{(\mu+1-U)^2}\dot{U}$$

where $U = \boldsymbol{\xi^T}\boldsymbol{\xi}$. Further calculation conducts the following inequality.

5-32

$$\dot{W} \leq \frac{c(c+1)}{(c+1-V)^2}\frac{\partial V}{\partial \boldsymbol{z}}\boldsymbol{h}(\boldsymbol{z}, \boldsymbol{0}, \boldsymbol{d}) + \frac{c(c+1)}{(c+1-V)^2}\frac{\partial V}{\partial \boldsymbol{z}}\left(\boldsymbol{h}\left(\boldsymbol{z}, \bar{\boldsymbol{\xi}}, \boldsymbol{d}\right) - \boldsymbol{h}(\boldsymbol{z}, \boldsymbol{0}, \boldsymbol{d})\right) - \frac{\mu}{\mu+1}KU + \boldsymbol{\xi^T}\boldsymbol{P_c}\boldsymbol{F_k}$$

Under the assumption $W(\boldsymbol{z}, \boldsymbol{\xi}) \leq \mu^2 + c^2 + 1$, one can find

$$V \leq (c+1)\frac{c^2+\mu^2+1}{c^2+\mu^2+1+c} \qquad \text{5-33a}$$

$$U \leq (c+1)\frac{c^2+\mu^2+1}{c^2+\mu^2+1+\mu} \qquad \text{5-33b}$$

$$\frac{c(c+1)}{(c+1-V)^2} \leq \frac{(c^2+\mu^2+1+c)^2}{c(c+1)} \qquad \text{5-33c}$$

By using (5-33c) and after further steps, the inequality (5-32) is converted to

$$\dot{W} \leq -\frac{(c^2+\mu^2+1+c)^2}{c(c+1)}\mathrm{O}_1 - \frac{\mu}{\mu+1}KU + \frac{(c^2+\mu^2+1+c)^2}{c(c+1)}\left|\frac{\partial V}{\partial \boldsymbol{z}}\right|\bar{\boldsymbol{h}} + \left|\boldsymbol{\xi^T}\boldsymbol{P_c}\right|\bar{\boldsymbol{F}}_{\boldsymbol{K}} \qquad \text{5-34}$$

where $\bar{\boldsymbol{h}}(\boldsymbol{z}, \boldsymbol{\xi}, \boldsymbol{d}) = sup_K\left|\boldsymbol{h}\left(\boldsymbol{z}, \bar{\boldsymbol{\xi}}, \boldsymbol{d}\right) - \boldsymbol{h}(\boldsymbol{z}, \boldsymbol{0}, \boldsymbol{d})\right|$ and does exist since $\boldsymbol{h}(.,.,.)$ is bounded by $\hat{\boldsymbol{h}}(\boldsymbol{z}, \boldsymbol{\xi}, \boldsymbol{d})$. For the same reason, there exists $\bar{\boldsymbol{F}}_{\boldsymbol{K}}(\boldsymbol{z}, \boldsymbol{\xi}, \boldsymbol{d}) = sup_K\left|\boldsymbol{F_K}\left(\boldsymbol{z}, \bar{\boldsymbol{\xi}}, \boldsymbol{d}\right)\right|$. Now, the following functions are defined.

$$\chi(\boldsymbol{z}) = \frac{(c^2+\mu^2+1+c)^2}{2c(c+1)}\mathrm{O}_1$$

$$\psi(\boldsymbol{\xi}) = \frac{\mu}{2(\mu+1)}U$$

$$\varphi(\boldsymbol{z},\boldsymbol{\xi},\boldsymbol{d}) = \frac{(c^2+\mu^2+1+c)^2}{c(c+1)}\left|\frac{\partial V}{\partial \boldsymbol{z}}\right|\overline{\boldsymbol{h}} + \left|\boldsymbol{\xi}^{\boldsymbol{T}}\boldsymbol{P_c}\right|\overline{\boldsymbol{F}}_{\boldsymbol{K}}$$

$$\kappa(K) = K$$

For an arbitrary small and strictly positive real number ρ, the set $\mathcal{S}$ is set as

$$\mathcal{S} = \{\boldsymbol{z}: \rho + \nu < W(\boldsymbol{z},\boldsymbol{\xi}) \leq \mu^2 + c^2 + 1\}$$

This set is proved to be compact due to the consequent inequalities (5-33a) and (5-33b). Moreover, the corresponding projections of the set satisfies $\mathcal{S}_z \subset \{\boldsymbol{z}: V < c+1\}$ and $\mathcal{S}_\xi \subset \{\boldsymbol{\xi}: U < \mu+1\}$. By the same logic used to prove Lemma 2.3 in [53], one can show that

1. $\chi(\boldsymbol{z})$ is continuous on $\mathcal{S}_z$ and positive definite on the projection set $\{(\boldsymbol{z},\boldsymbol{\xi}): \boldsymbol{\xi} = \boldsymbol{0}\}$,
2. $\psi(\boldsymbol{\xi})$ is continuous on $\mathcal{S}_\xi$ and positive definite on $\mathcal{S}_\xi \backslash \{\boldsymbol{0}\}$,
3. $\varphi(\boldsymbol{z},\boldsymbol{\xi},\boldsymbol{d})$ is continuous on $\mathcal{S} \times \mathcal{D}$, and

   $\varphi(\boldsymbol{z},\boldsymbol{x},\boldsymbol{d}) = \boldsymbol{0}$ for all $(\boldsymbol{z},\boldsymbol{x},\boldsymbol{d}) \in (\{(\boldsymbol{z},\boldsymbol{x}): \boldsymbol{x} = \boldsymbol{0}\} \cap \mathcal{S}) \times \mathcal{D}$.

This implies that all the conditions of Lemma 5.2 are satisfied; thus, there exists $K_* \geq 1$ such that, for all $K \geq K_*$ the inequality (5-34) takes the form

$\dot{W} \leq -\chi(\boldsymbol{z}) - K\psi(\boldsymbol{\xi})$

Finally, we set $\mathrm{O}_2 = \chi(\boldsymbol{z}) + K\psi(\boldsymbol{\xi})$ which is positive definite on $\mathcal{S}$, and the proof is completed.

It can be checked that increasing the upper bound of the set $W(\boldsymbol{z},\boldsymbol{\xi}) \leq \mu^2 + c^2 + 1$ will not change the result since

$$\frac{aV}{a+1-V} \leq b \ \rightarrow V \leq (a+1)\frac{b}{b+a} < a+1$$

and b dose not change the required inequality $V < a+1$. This result is used to prove the next corollary.

Corollary 5.2: Let the nonlinear closed loop system have the form

$$\begin{cases} \dot{\boldsymbol{z}} = \boldsymbol{h}\left(\boldsymbol{z},\bar{\boldsymbol{\xi}},\boldsymbol{d}(t)\right) \\ \dot{\boldsymbol{\xi}}^{\boldsymbol{1}} = K^1\boldsymbol{A_c}\boldsymbol{\xi}^{\boldsymbol{1}} \\ \vdots \\ \dot{\boldsymbol{\xi}}^{\boldsymbol{m}} = K^m\boldsymbol{A_c}\boldsymbol{\xi}^{\boldsymbol{m}} \end{cases}$$

where $\boldsymbol{\xi}^{\boldsymbol{i}} = col\left(\xi_1^i, \dots, \xi_{r_i}^i\right)$, $\bar{\boldsymbol{\xi}} = col\left(\bar{\boldsymbol{\xi}}^{\boldsymbol{1}}, \dots, \bar{\boldsymbol{\xi}}^{\boldsymbol{m}}\right)$, and $\bar{\boldsymbol{\xi}}^{\boldsymbol{i}} = col\left(\xi_1^i, K\xi_2^i, \dots, K^{j-1}\xi_{r_i}^i\right)$. Let ULP assumption be held and the polynomials

$p^i(s) = s^{r_i} + a_{r_i}^i s^{r_i-1} + \cdots + a_1^i$

be Hurwitz. Let the matrix $\boldsymbol{A_c^i}$ be the companion form corresponding to $p^i(s)$. Moreover, assume $\boldsymbol{P_c^i}$ solve the matrix equation $\left(\boldsymbol{A_c^i}\right)^{\boldsymbol{T}}\boldsymbol{P_c^i} + \boldsymbol{P_c^i}\boldsymbol{A_c^i} = -\boldsymbol{I}$. First, the variable $\xi_k^i = {x_k^i}/{(K^i)^{k-1}}$ is defined, for a must be defined parameter $K^i \geq 1$ and $k = 1, \dots, r_i$. In new coordinate system $\boldsymbol{\xi} = col\left(\boldsymbol{\xi}^{\boldsymbol{1}}, \dots, \boldsymbol{\xi}^{\boldsymbol{m}}\right)$,

let $\boldsymbol{h}(.,.,.)$ is bounded by a continuous function $\widehat{\boldsymbol{h}}(\boldsymbol{z},\boldsymbol{\xi},\boldsymbol{d})$. Next, for some given $\mu_i \geq 1$, the Lyapunov function is defined as

$$W(\boldsymbol{z},\boldsymbol{\xi}) = c\frac{V}{c+1-V} + \mu_1\frac{\left(\boldsymbol{\xi^1}\right)^{\boldsymbol{T}}\boldsymbol{P_c^1}\boldsymbol{\xi^1}}{\mu_1+1-(\boldsymbol{\xi^1})^{\boldsymbol{T}}\boldsymbol{P_c^1}\boldsymbol{\xi^1}} + \cdots + \mu_m\frac{(\boldsymbol{\xi^m})^{\boldsymbol{T}}\boldsymbol{P_c^m}\boldsymbol{\xi^m}}{\mu_m+1-(\boldsymbol{\xi^m})^{\boldsymbol{T}}\boldsymbol{P_c^m}\boldsymbol{\xi^m}} \quad 5\text{-}35$$

In addition, we define the set

$$\mathcal{U}_3 = \{\boldsymbol{z}: V(\boldsymbol{z}) < c+1\} \times \left\{\boldsymbol{\xi^1}: \left(\boldsymbol{\xi^1}\right)^{\boldsymbol{T}}\boldsymbol{P_c^1}\boldsymbol{\xi^1} < \mu_1+1\right\} \times \ldots \times \{\boldsymbol{\xi^m}: (\boldsymbol{\xi^m})^{\boldsymbol{T}}\boldsymbol{P_c^m}\boldsymbol{\xi^m} < \mu_m+1\}$$

Under these conditions, the function $W(\boldsymbol{z},\boldsymbol{\xi}): \mathcal{U}_3 \to \mathbb{R}^+$ is proper on $\mathcal{U}_3$ and for strictly positive real numbers ρ_i's, the positive real number $K_*^i \geq 1$ can be found such that, for all $K^i > K_*^i$, W satisfies $\dot{W} \leq -\mathrm{O}_3(\boldsymbol{z},\boldsymbol{\xi})$ where $\mathrm{O}_3(\boldsymbol{z},\boldsymbol{\xi})$ is continuous on $\mathcal{U}_3$ and positive definite on

$$\{(\boldsymbol{z},\boldsymbol{\xi}): \rho_1+\cdots+\rho_m+\nu < W(\boldsymbol{z},\boldsymbol{\xi}) \leq (\mu_1)^2+\cdots+(\mu_m)^2+c^2+1\}$$

Proof: This is proved by induction and Lemma 5.3.

Step 1: The system takes the form

$$\begin{cases} \dot{\boldsymbol{z}} = \boldsymbol{h}\left(\boldsymbol{z}, \bar{\boldsymbol{\xi}}_{\boldsymbol{1}}, \overbrace{\boldsymbol{0},\ldots,\boldsymbol{0}}^{\boldsymbol{m-1}}, \boldsymbol{d}(t)\right) \\ \dot{\boldsymbol{\xi}}^{\boldsymbol{1}} = K^1\boldsymbol{A_c}\boldsymbol{\xi^1} \end{cases}$$

The conditions of Lemma 5.3 are met; thus, the function

$$W_1\left(\boldsymbol{z},\boldsymbol{\xi^1}\right) = c\frac{V}{c+1-V} + \mu_1\frac{\left(\boldsymbol{\xi^1}\right)^{\boldsymbol{T}}\boldsymbol{P_c^1}\boldsymbol{\xi^1}}{\mu_1+1-(\boldsymbol{\xi^1})^{\boldsymbol{T}}\boldsymbol{P_c^1}\boldsymbol{\xi^1}}$$

is proper on $\mathcal{U}_2$ and satisfies $\dot{W}_1 \leq -\mathrm{O}_2\left(\boldsymbol{z},\boldsymbol{\xi^1}\right)$ where $\mathrm{O}_2\left(\boldsymbol{z},\boldsymbol{\xi^1}\right)$ is continuous on $\mathcal{U}_2$ and positive definite on $\left\{\left(\boldsymbol{z},\boldsymbol{\xi^1}\right): \rho_1+\nu < W_1\left(\boldsymbol{z},\boldsymbol{\xi^1}\right) \leq (\mu_1)^2+\cdots+(\mu_m)^2+c^2+1\right\}$.

Step 2: It is assumed that for the system

$$\begin{cases} \dot{\boldsymbol{z}} = \boldsymbol{h}\left(\boldsymbol{z}, \bar{\boldsymbol{\xi}}_{\boldsymbol{1}}, \ldots, \bar{\boldsymbol{\xi}}_{\boldsymbol{l}}, \overbrace{\boldsymbol{0},\ldots,\boldsymbol{0}}^{\boldsymbol{m-l}}, \boldsymbol{d}(t)\right) \\ \dot{\boldsymbol{\xi}}^{\boldsymbol{1}} = K^1\boldsymbol{A_c}\boldsymbol{\xi^1} \\ \vdots \\ \dot{\boldsymbol{\xi}}^{\boldsymbol{l}} = K^l\boldsymbol{A_c}\boldsymbol{\xi^l} \end{cases} \quad 5\text{-}36$$

There exists a function as

$$W_l\left(\boldsymbol{z},\boldsymbol{\xi^1},\ldots,\boldsymbol{\xi^l}\right) = c\frac{V}{c+1-V} + \mu_1\frac{\left(\boldsymbol{\xi^1}\right)^{\boldsymbol{T}}\boldsymbol{P_c^1}\boldsymbol{\xi^1}}{\mu_1+1-(\boldsymbol{\xi^1})^{\boldsymbol{T}}\boldsymbol{P_c^1}\boldsymbol{\xi^1}} + \cdots + \mu_l\frac{\left(\boldsymbol{\xi^l}\right)^{\boldsymbol{T}}\boldsymbol{P_c^l}\boldsymbol{\xi^l}}{\mu_l+1-(\boldsymbol{\xi^l})^{\boldsymbol{T}}\boldsymbol{P_c^l}\boldsymbol{\xi^l}}$$

which is proper on the set

$$\mathcal{U}_3^l = \{\boldsymbol{z}: V(\boldsymbol{z}) < c+1\} \times \left\{\boldsymbol{\xi^1}: \left(\boldsymbol{\xi^1}\right)^T \boldsymbol{P_c^1} \boldsymbol{\xi^1} < \mu_1 + 1\right\} \times \ldots \times \left\{\boldsymbol{\xi^l}: \left(\boldsymbol{\xi^l}\right)^T \boldsymbol{P_c^l} \boldsymbol{\xi^l} < \mu_l + 1\right\}$$

and satisfies $\dot{W}_l \leq -\mathrm{O}_3^l\left(\boldsymbol{z}, \boldsymbol{\xi^1}, \ldots, \boldsymbol{\xi^l}\right)$ where O_3^l is continuous on $\mathcal{U}_3^l$ and positive definite on the set

$$\left\{\left(\boldsymbol{z}, \boldsymbol{\xi^1}, \ldots, \boldsymbol{\xi^l}\right): \rho_1 + \cdots + \rho_l + \nu < W_l\left(\boldsymbol{z}, \boldsymbol{\xi^1}, \ldots, \boldsymbol{\xi^l}\right) \leq (\mu_1)^2 + \cdots + (\mu_m)^2 + c^2 + 1\right\}$$

for some strictly positive real numbers ρ_i, $1 \leq i \leq l$. Since $\rho_1 + \cdots + \rho_l + \nu$ is an arbitrary small and strictly positive and $((\mu_1)^2 + \cdots + (\mu_m)^2 + c^2) > 1$ the ULP assumption is observed for the system (5-36).

Step 3: It needs to be proved that there exists a Lyapunov function as

$$W_{l+1}\left(\boldsymbol{z}, \boldsymbol{\xi^1}, \ldots, \boldsymbol{\xi^l}, \boldsymbol{\xi^{l+1}}\right) = W_l\left(\boldsymbol{z}, \boldsymbol{\xi^1}, \ldots, \boldsymbol{\xi^l}\right) + \mu_{l+1} \frac{\left(\boldsymbol{\xi^{l+1}}\right)^T \boldsymbol{P_c^{l+1}} \boldsymbol{\xi^{l+1}}}{\mu_{l+1} + 1 - (\boldsymbol{\xi^{l+1}})^T \boldsymbol{P_c^{l+1}} \boldsymbol{\xi^{l+1}}}$$

which is proper on the set

$$\mathcal{U}_3^{l+1} = \mathcal{U}_3^l \times \left\{\boldsymbol{\xi^l}: \left(\boldsymbol{\xi^l}\right)^T \boldsymbol{P_c^l} \boldsymbol{\xi^l} < \mu_l + 1\right\}$$

and satisfies $\dot{W}_{l+1} \leq -\mathrm{O}_3^{l+1}\left(\boldsymbol{z}, \boldsymbol{\xi^1}, \ldots, \boldsymbol{\xi^l}, \boldsymbol{\xi^{l+1}}\right)$ where O_3^{l+1} is continuous on $\mathcal{U}_3^{l+1}$ and positive definite on the set

$$\left\{\left(\boldsymbol{z}, \boldsymbol{\xi^1}, \ldots, \boldsymbol{\xi^l}, \boldsymbol{\xi^{l+1}}\right): \rho_1 + \cdots + \rho_{l+1} + \nu < W_{l+1}\left(\boldsymbol{z}, \boldsymbol{\xi^1}, \ldots, \boldsymbol{\xi^l}, \boldsymbol{\xi^{l+1}}\right) \leq (\mu_1)^2 + \cdots + (\mu_m)^2 + c^2 + 1\right\}$$

for some strictly positive real numbers ρ_i, $1 \leq i \leq (l+1)$. This can be achieved by following the same steps utilized in the proof of Lemma 5.3. The only difference is that since the Lyapunov function W_l is proper, it is directly used instead of the form $\bar{c}\frac{W_l}{\bar{c}+1-W_l}$.

The second backstepping tool which will be employed in control design is the following Lemma.

Lemma 5.4 [53]: Consider the diffeomorphic nonlinear system of the form

$$\begin{cases} \dot{\boldsymbol{z}} = \boldsymbol{h}\left(\boldsymbol{z}, \boldsymbol{e}, \boldsymbol{d}(t)\right) \\ \dot{\boldsymbol{e}} = L\boldsymbol{A_0}\boldsymbol{e} + \boldsymbol{P}\left(\boldsymbol{z}, \boldsymbol{e}, \boldsymbol{d}(t)\right) \end{cases}$$

where $\boldsymbol{z} \in \mathbb{R}^m$, $\boldsymbol{e} \in \mathbb{R}^n$, L is a strictly positive real number and the matrix $\boldsymbol{A_0}$ is Hurwitz. Let assumption ULP be satisfied and define the set $\mathcal{T} = \{\boldsymbol{z}: V(\boldsymbol{z}) \leq c+1\}$. Assume that there exists positive real numbers υ_1 and υ_2 and a bounded continuous function γ such that $\gamma(0) = 0$ and for every $(\boldsymbol{z}, \boldsymbol{e}, \boldsymbol{d}) \in \mathcal{T} \times \mathbb{R}^m \times \mathcal{D}$,

$$\|\boldsymbol{h}(\boldsymbol{z}, \boldsymbol{e}, \boldsymbol{d}) - \boldsymbol{h}(\boldsymbol{z}, \boldsymbol{0}, \boldsymbol{d})\| \leq \gamma(\|\boldsymbol{e}\|)$$
$$\|\boldsymbol{P}(\boldsymbol{z}, \boldsymbol{e}, \boldsymbol{d})\| \leq \nu_1 + \nu_2\|\boldsymbol{e}\|$$

Consider a class-K_∞ function is provided such that

$$\lim_{L\to\infty} inf \frac{L}{\mu^4(L)} \to \infty$$

Moreover, let $\boldsymbol{P_0}$ be the solution of the matrix equation $\boldsymbol{A_0^T P_0} + \boldsymbol{P_0 A_0} = -\boldsymbol{I}$. Define the function

$$W(\boldsymbol{z},\boldsymbol{e}) = c\frac{V(\boldsymbol{z})}{c+1-V(\boldsymbol{z})} + \mu(L)\frac{ln\big(1+\boldsymbol{e^T P_0 e}\big)}{\mu(L)+1-ln(1+\boldsymbol{e^T P_0 e})} \quad 5\text{-}37$$

and the set

$$\mathcal{U}_4 = \{\boldsymbol{z}: V(\boldsymbol{z}) < c+1\} \times \big\{\boldsymbol{e}: ln\big(1+\boldsymbol{e^T P_0 e}\big) < \mu(L)+1\big\}$$

Under the quoted assumptions, for some strictly positive real number L, the function $W(\boldsymbol{z},\boldsymbol{e}): \mathcal{U}_4 \to \mathbb{R}^+$ is proper on $\mathcal{U}_4$. Moreover, there exists a positive real number L_* such that, for $L \geq L_*$ and every positive real number ρ, the inequality $\dot{W} \leq -\mathrm{O}_4(\boldsymbol{z},\boldsymbol{e})$ is observed. In this case, O_4 is continuous on $\mathcal{U}_4$ and positive definite on the set $\Big\{(\boldsymbol{z},\boldsymbol{e}): \rho+\nu < W(\boldsymbol{z},\boldsymbol{e}) \leq \big(\mu(L)\big)^2 + c^2 + 1\Big\}$.

According to the Lyapunov theory, the asymptotic stability of the dynamical system around an equilibrium point is guaranteed when there exists a positive definite function whose derivative is negative definite on a specified set. The introduced backstepping tools in the previous two Lemmas provide the existence of the Lyapunov function. In the next subsections, the Lyapunov approach is used to prove the stability of the closed loop system by choosing the proper control parameters.

5.3.2 The canonical internal model

In the next subsections a regulation via partial state feedback control is illustrated, and as the first step, a particular parameterization of the internal model (5-26) is adapted here to be used in the next steps. This new parameterization is inspired by the Nikiforov'swork, and precisely comes from the following lemma. It should be noted that $i = 1, \dots, m$ in all the following equations.

Lemma 5.5: Given any square Hurwitz matrix $\boldsymbol{F^i}$ and any vector $\boldsymbol{G^i}$ such that the pair $\big(\boldsymbol{F^i}, \boldsymbol{G^i}\big)$ is controllable, the Sylvester equation

$$\boldsymbol{M_\sigma^i \Phi^i(\sigma) - F^i M_\sigma^i = G^i \Gamma^i} \quad 5\text{-}37$$

has a unique solution $\boldsymbol{M_\sigma^i}$, which is nonsingular.

In fact, this solution is used to represent the internal model (5-26) in a new coordinate coordinates defined by the transformation matrix $\boldsymbol{M_\sigma^i}$. In the new coordinate system the internal model has the form:

$$\begin{aligned} \dot{\bar{\boldsymbol{\eta}}}^{\boldsymbol{i}} &= \big(\boldsymbol{F^i} + \boldsymbol{\Psi_\sigma^i G^i}\big)\bar{\boldsymbol{\eta}}^{\boldsymbol{i}} \\ v_i &= \boldsymbol{\Psi_\sigma^i}\bar{\boldsymbol{\eta}}^{\boldsymbol{i}} \end{aligned} \quad 5\text{-}38$$

in which

$$\boldsymbol{\Psi_\sigma^i} = \boldsymbol{\Gamma^i} {\boldsymbol{M_\sigma^i}}^{-1}$$

$$\bar{\boldsymbol{\tau}}_{\boldsymbol{\sigma}}^{\boldsymbol{i}}(\boldsymbol{w},\boldsymbol{\mu}) = \boldsymbol{M_\sigma^i \tau_\sigma^i}(\boldsymbol{w},\boldsymbol{\mu})$$

The critical point is that the output of (5-38) is exactly the mapping $c_\sigma^i(\boldsymbol{w},\boldsymbol{\mu})$.

Since the error and its derivatives are used in feedback control regulation, the design is initiated by representing the system in the error form. On this matter, the states are the difference between the

output vector and its reference trajectory as derived in (5-21) in addition to their derivatives. More detail can be found in the next subsection.

5.3.3 The error system

In practice, some change of coordinate is required to figure out the controller structure and coefficient stabilizing the closed loop system. The first global change of coordinate transfers the origin of the plant to the mappings derived from (5-22) and also the globally mappings $\vartheta_\sigma^i(\boldsymbol{w},\boldsymbol{\mu})$. The transformation has the form

$$\begin{aligned}\tilde{x}^i &= x^i - \vartheta_\sigma^i(\boldsymbol{w},\boldsymbol{\mu})\\ \tilde{\boldsymbol{z}} &= \boldsymbol{z} - \boldsymbol{\zeta_\sigma}(\boldsymbol{w},\boldsymbol{\mu})\end{aligned} \tag{5-39}$$

Then (5-20) takes the so called error system form

$$\begin{cases}\dot{\tilde{x}}_1^i = \tilde{x}_2^i\\ \vdots\\ \dot{\tilde{x}}_{r_i-1}^i = \tilde{x}_{r_i}^i\\ \dot{\tilde{x}}_{r_i}^i = \tilde{f}_r^i(\tilde{\boldsymbol{z}},\tilde{\boldsymbol{x}},\boldsymbol{w},\boldsymbol{\mu}) + b^i(\boldsymbol{\mu})(v_i - c_\sigma^i(\boldsymbol{w},\boldsymbol{\mu}))\\ \dot{\tilde{\boldsymbol{z}}} = \tilde{\boldsymbol{f}}_{\boldsymbol{0}}(\tilde{\boldsymbol{z}},\tilde{\boldsymbol{x}},\boldsymbol{w},\boldsymbol{\mu}) + \tilde{\boldsymbol{C}}(\tilde{\boldsymbol{z}},\tilde{\boldsymbol{x}},\boldsymbol{w},\boldsymbol{\mu})\big(\boldsymbol{v} - \boldsymbol{c_\sigma}(\boldsymbol{w},\boldsymbol{\mu})\big)\\ e_i = \tilde{x}_1^i\end{cases} \tag{5-40}$$

where $\boldsymbol{c_\sigma} = col(c_\sigma^1, c_\sigma^2, \cdots, c_\sigma^m)$ and r_i is the number of output derivatives used as the states and the output itself. In addition, $\tilde{\boldsymbol{x}} = col\big(\tilde{\boldsymbol{x}}^{\boldsymbol{1}}, \dots, \tilde{\boldsymbol{x}}^{\boldsymbol{m}}\big)$.

The first assumption made on error system eliminates the zero dynamics, which affect the control signal but not the output, to asymptotically stable ones. This assumption is summarized below.

Assumption 5.3: it is assumed that the zero dynamics of (5-40) having the form

$$\dot{\tilde{\boldsymbol{z}}} = \tilde{\boldsymbol{f}}_{\boldsymbol{0}}(\tilde{\boldsymbol{z}},\boldsymbol{0},\boldsymbol{w},\boldsymbol{\mu}) \tag{5-41}$$

is asymptotically and locally exponentially stable at $\tilde{z} = 0$.

In order to proceed, a few more changes of variable are required to gradually convert the system to a form proper to be stabilized. At this level, the following change of coordinates is applied:

$$\theta^i = \tilde{x}_{r_i}^i + \big(k^i\big)^{r_i-1} b_0^i \tilde{x}_1^i + \cdots + \big(k^i\big) b_{r_i-2}^i \tilde{x}_{r_i-1}^i \tag{5-42}$$

in which $k^i > 0$ are chosen such that the polynomial

$$p_0^i(\lambda) = \lambda^{r_i-1} + b_{r_i-2}^i \lambda^{r_i-2} + \cdots + b_1^i \lambda + b_0^i$$

is Hurwitz. Now, the system (5-40) is converted to

$$\begin{cases}\dot{\tilde{\boldsymbol{z}}}_{\boldsymbol{a}} = \boldsymbol{f_a}(\tilde{\boldsymbol{z}}_{\boldsymbol{a}},\boldsymbol{\theta},\boldsymbol{w},\boldsymbol{\rho},\boldsymbol{k}) + \boldsymbol{G_a}\boldsymbol{\theta} + \overline{\boldsymbol{C}}(\tilde{\boldsymbol{z}},\tilde{\boldsymbol{x}},\boldsymbol{w},\boldsymbol{\mu})\big(\boldsymbol{v} - \boldsymbol{c_\sigma}(\boldsymbol{w},\boldsymbol{\mu})\big)\\ \dot{\boldsymbol{\theta}} = \boldsymbol{\phi}(\tilde{\boldsymbol{z}}_{\boldsymbol{a}},\boldsymbol{\theta},\boldsymbol{w},\boldsymbol{\rho},\boldsymbol{k}) + \boldsymbol{b}(\boldsymbol{\mu})\big(\boldsymbol{v} - \boldsymbol{c_\sigma}(\boldsymbol{w},\boldsymbol{\mu})\big)\end{cases} \tag{5-43}$$

where, $\boldsymbol{\rho} = (\boldsymbol{\mu}, \boldsymbol{\sigma})$, $\boldsymbol{k} = col(k^1, k^2, \dots, k^m)$, $\boldsymbol{\theta} = col(\theta^1, \theta^2, \dots, \theta^m)$, $\overline{\boldsymbol{C}} = \begin{bmatrix} \widetilde{\boldsymbol{C}} \\ \mathbf{0}_{(n-m)\times m} \end{bmatrix}$,

$\tilde{\boldsymbol{z}}_{\boldsymbol{a}} = col\left(\tilde{\mathbf{z}}, \tilde{x}_1^1, \dots, \tilde{x}_{r_1-1}^1, \dots, \tilde{x}_1^m, \dots, \tilde{x}_{r_m-1}^m\right)$

$\boldsymbol{b}(\boldsymbol{\mu}) = diag\left(b^1(\boldsymbol{\mu}), b^2(\boldsymbol{\mu}), \dots, b^m(\boldsymbol{\mu})\right)$

$$\boldsymbol{f}_{\boldsymbol{a}}(\tilde{\boldsymbol{z}}_{\boldsymbol{a}}, \boldsymbol{\theta}, \boldsymbol{w}, \boldsymbol{\rho}, \boldsymbol{k}) = \begin{pmatrix} \tilde{\boldsymbol{f}}_{\mathbf{0}}(\tilde{\boldsymbol{z}}_{\boldsymbol{a}}, \boldsymbol{\theta} - \overline{\boldsymbol{\theta}}, \boldsymbol{w}, \boldsymbol{\mu}) \\ \tilde{x}_2^1 \\ \vdots \\ -(k^1)^{r_1-1} b_0^1 \tilde{x}_1^1 - \cdots - (k^1) b_{r_1-2}^1 \tilde{x}_{r_1-1}^1 \\ \vdots \\ \tilde{x}_2^m \\ \vdots \\ -(k^m)^{r_m-1} b_0^m \tilde{x}_1^m - \cdots - (k^m) b_{r_m-2}^m \tilde{x}_{r_m-1}^m \end{pmatrix}$$

$$\boldsymbol{G}_{\boldsymbol{a}} = \begin{pmatrix} \mathbf{0}_{dim(\tilde{\mathbf{z}})\times 1} & \mathbf{0}_{dim(\tilde{\mathbf{z}})\times 1} & \mathbf{0}_{dim(\tilde{\mathbf{z}})\times 1} \\ \boldsymbol{G}_{\boldsymbol{a}}^{\mathbf{1}} & \cdots & \mathbf{0}_{(r_1-1)\times 1} \\ \vdots & \ddots & \vdots \\ \mathbf{0}_{(r_m-1)\times 1} & \cdots & \boldsymbol{G}_{\boldsymbol{a}}^{\boldsymbol{m}} \end{pmatrix}, \boldsymbol{G}_{\boldsymbol{a}}^{\boldsymbol{i}} = col(0,0,\dots,1)_{(r_i-1)\times 1}$$

$$\boldsymbol{\phi}(\tilde{\boldsymbol{z}}_{\boldsymbol{a}}, \boldsymbol{\theta}, \boldsymbol{w}, \boldsymbol{\rho}, \boldsymbol{k}) = \begin{pmatrix} \tilde{f}_r^1(\tilde{\boldsymbol{z}}_{\boldsymbol{a}}, \boldsymbol{\theta} - \overline{\boldsymbol{\theta}}, \boldsymbol{w}, \boldsymbol{\rho}) \\ \vdots \\ \tilde{f}_r^m(\tilde{\boldsymbol{z}}_{\boldsymbol{a}}, \boldsymbol{\theta} - \overline{\boldsymbol{\theta}}, \boldsymbol{w}, \boldsymbol{\rho}) \end{pmatrix}, \overline{\boldsymbol{\theta}} = \begin{pmatrix} (k^1)^{r_1-1} b_0^1 \tilde{x}_1^1 + \cdots + (k^1) b_{r_1-2}^1 \tilde{x}_{r_1-1}^1 \\ \vdots \\ (k^m)^{r_m-1} b_0^m \tilde{x}_1^m + \cdots + (k^m) b_{r_m-2}^m \tilde{x}_{r_m-1}^m \end{pmatrix}$$

Given the new state space representation, the first step in stability evaluation can be made. In fact, the zero dynamics of the system (5-43) is introduced and proved to be asymptotically and locally exponentially stable. The zero dynamics have the form

$$\dot{\tilde{\boldsymbol{z}}}_{\boldsymbol{a}} = \boldsymbol{f}_{\boldsymbol{a}}(\tilde{\boldsymbol{z}}_{\boldsymbol{a}}, \mathbf{0}, \boldsymbol{w}, \boldsymbol{\rho}, \boldsymbol{k}) \qquad 5\text{-}44$$

Let $\tilde{\boldsymbol{f}}_{\mathbf{0}}(\tilde{\boldsymbol{z}}_{\boldsymbol{a}}, \boldsymbol{\theta} - \overline{\boldsymbol{\theta}}, \boldsymbol{w}, \boldsymbol{\mu})$ is bounded by a continuous function $\hat{\boldsymbol{f}}_{\mathbf{0}}(\tilde{\boldsymbol{z}}, \overline{\boldsymbol{v}}, \boldsymbol{w}, \boldsymbol{\mu})$ where $\overline{\boldsymbol{v}} = col(\overline{\boldsymbol{v}}^1, \dots, \overline{\boldsymbol{v}}^m)$, and $\overline{\boldsymbol{v}}^i$ is defined in the same way as $\overline{\boldsymbol{\xi}}^i$ in Corollary 5-2. Given assumption 5-3, the ULP assumption can be made. Under these assumptions, the system (5-44) admits the proper Lyapunov function, whose existence proves the stability, as introduced in Corollary 5-3. Since the properties of the introduced Lyapunov function is preserved for any $\boldsymbol{x} \in \mathcal{D}$, $\boldsymbol{w_0} \in \mathcal{K}_w$, and $(\boldsymbol{\sigma}, \boldsymbol{\mu}) \in \mathcal{K}_\sigma \times \mathcal{K}_\mu$, the system (5-44) is uniformly asymptotically stable in parameter $\boldsymbol{k}$, and locally exponentially stable at point $\tilde{\boldsymbol{z}}_{\boldsymbol{a}} = \mathbf{0}$. In other words, for some finite positive number $R_1 > 0$, there exist real numbers $c > 1, \boldsymbol{k}^* > 0$ such that for any $\boldsymbol{k} > \boldsymbol{k}^*$, there exists a continuously differentiable positive definite function W_1 with the properties:

1. The set $\mathcal{U}_1 = \{\tilde{\boldsymbol{z}}_{\boldsymbol{a}} : W_1(\tilde{\boldsymbol{z}}_{\boldsymbol{a}}) < c + 1\}$ is compact containing the set $\overline{\mathcal{B}}_{\mathrm{R}_1}$.
2. The function is positive definite on $\mathcal{U}_1$.
3. For some positive numbers e_1, e_2, r_1, the estimate $e_1\|\tilde{\boldsymbol{z}}_{\boldsymbol{a}}\|^2 \le W_1(\tilde{\boldsymbol{z}}_{\boldsymbol{a}}) \le e_2\|\tilde{\boldsymbol{z}}_{\boldsymbol{a}}\|^2$ holds for any $\tilde{\boldsymbol{z}}_{\boldsymbol{a}} \in \mathcal{B}_{r_1}$, for some positive.

4. $\dot{W}_1 < -\alpha_1(\tilde{\boldsymbol{z}}_{\boldsymbol{a}})$ for any $\tilde{\boldsymbol{z}}_{\boldsymbol{a}} \in \{\tilde{\boldsymbol{z}}_{\boldsymbol{a}}: W_1(\tilde{\boldsymbol{z}}_{\boldsymbol{a}}) < c + 1\}$, $\boldsymbol{w^0} \in \mathcal{K}_w$, and $\boldsymbol{\rho} \in \mathcal{R}$, in which $\alpha_1(.)$ is a positive definite function satisfying $\alpha_1(\tilde{\boldsymbol{z}}_{\boldsymbol{a}}) \geq l\|\tilde{\boldsymbol{z}}_{\boldsymbol{a}}\|^2$, for some $l > 0$.

This positive definite function, the Lyapunov function, can be defined as

$$W_1(\tilde{z}_a) = c_0 \frac{V(\tilde{\boldsymbol{z}})}{1 + c_0 - V(\tilde{\boldsymbol{z}})} + \sum_{i=1}^{m} d_i \frac{U_1^i(\tilde{\boldsymbol{x}}_{\boldsymbol{a}}^{\boldsymbol{i}})}{1 + d_i - U_1^i(\tilde{\boldsymbol{x}}_{\boldsymbol{a}}^{\boldsymbol{i}})} \qquad 5\text{-}45$$

where $U_1^i(\tilde{\boldsymbol{x}}_{\boldsymbol{a}}^{\boldsymbol{i}}) = (\tilde{\boldsymbol{x}}_{\boldsymbol{a}}^{\boldsymbol{i}})^T \boldsymbol{D}_{\boldsymbol{k}^i}^{-T} \boldsymbol{P}_{\boldsymbol{0}}^{\boldsymbol{i}} \boldsymbol{D}_{\boldsymbol{k}^i}^{-1} \tilde{\boldsymbol{x}}_{\boldsymbol{a}}^{\boldsymbol{i}}$, $D_{k^i} = diag\left(1, k^i, \dots, (k^i)^{r_i-2}\right)$, $\tilde{\boldsymbol{x}}_{\boldsymbol{a}}^{\boldsymbol{i}} = col(\tilde{x}_1^i, \dots, \tilde{x}_{r_i-1}^i)$, the function V is the Lyapunov function derived from assumption 5.3. Moreover, by denoting the companion matrix of the polynomial $p_0^i(\lambda)$ with $\boldsymbol{A}_{\boldsymbol{0}}^{\boldsymbol{i}}$, $\boldsymbol{P}_{\boldsymbol{0}}^{\boldsymbol{i}}$ is the solution of Lyapunov equation $\boldsymbol{P}_{\boldsymbol{0}}^{\boldsymbol{i}} \boldsymbol{A}_{\boldsymbol{0}}^{\boldsymbol{i}} + (\boldsymbol{A}_{\boldsymbol{0}}^{\boldsymbol{i}})^{\boldsymbol{T}} \boldsymbol{P}_{\boldsymbol{0}}^{\boldsymbol{i}} = -\boldsymbol{I}$. In fact, the system (5-44) preserves the conditions of ULP assumption.

At this point, the internal model presented in (5-38) providing reference control is augmented with a new input variable to impose the effect of deviation from reference trajectory to control signal. The new internal model is then connected to a memory-less stabilizer controller in parallel. A saturation level is also put on the control elements to guarantee stability. Therefore, the error system (5-43) is augmented with

$$\begin{aligned} \dot{\boldsymbol{\xi}} &= (\overline{\boldsymbol{F}} + \overline{\boldsymbol{G}}\boldsymbol{\Psi}_{\boldsymbol{\sigma}})\boldsymbol{\xi} + \overline{\boldsymbol{N}}\boldsymbol{\theta} \\ \boldsymbol{v} &= \boldsymbol{\Psi}_{\boldsymbol{\sigma}} sat(\boldsymbol{\xi}) - diag(K^1, \dots, K^m)\boldsymbol{\theta} \end{aligned} \qquad 5\text{-}46$$

where $\boldsymbol{\xi} = col(\xi^1, \dots, \xi^m)$ and

$$\overline{\boldsymbol{G}} = \begin{pmatrix} \boldsymbol{G^1} & \cdots & \boldsymbol{0}_{q_1 \times 1} \\ \vdots & \ddots & \vdots \\ \boldsymbol{0}_{q_m \times 1} & \cdots & \boldsymbol{G^m} \end{pmatrix}, \overline{\boldsymbol{F}} = \begin{pmatrix} \boldsymbol{F^1} & \dots & \boldsymbol{0}_{q_1 \times q_1} \\ \vdots & \ddots & \vdots \\ \boldsymbol{0}_{q_m \times q_m} & \dots & \boldsymbol{F^m} \end{pmatrix}$$

$$\boldsymbol{\Psi}_{\boldsymbol{\sigma}} = \begin{pmatrix} \boldsymbol{\Psi}_{\boldsymbol{\sigma}}^{\boldsymbol{1}} & \dots & \boldsymbol{0}_{1 \times q_m} \\ \vdots & \ddots & \vdots \\ \boldsymbol{0}_{1 \times q_1} & \dots & \boldsymbol{\Psi}_{\boldsymbol{\sigma}}^{\boldsymbol{m}} \end{pmatrix}, \overline{\boldsymbol{N}} = \begin{pmatrix} \boldsymbol{N^1} & \dots & \boldsymbol{0}_{q_1 \times 1} \\ \vdots & \ddots & \vdots \\ \boldsymbol{0}_{q_m \times 1} & \dots & \boldsymbol{N^m} \end{pmatrix}$$

It can be easily observed that (5-46) is composed of individual systems of the form

$$\begin{aligned} \dot{\boldsymbol{\xi}}^{\boldsymbol{i}} &= \left(\boldsymbol{F}^{\boldsymbol{i}} + \boldsymbol{G}^{\boldsymbol{i}}\boldsymbol{\Psi}_{\boldsymbol{\sigma}}^{\boldsymbol{i}}\right)\boldsymbol{\xi}^{\boldsymbol{i}} + \boldsymbol{N}^{\boldsymbol{i}}\theta^i \\ v_i &= \boldsymbol{\Psi}_{\boldsymbol{\sigma}}^{\boldsymbol{i}} sat\left(\boldsymbol{\xi}^{\boldsymbol{i}}\right) - K^i\theta^i \qquad K^i > 0 \end{aligned} \qquad 5\text{-}47$$

for $1 \leq i \leq m$.

The third change of coordinates is applied to find out the appropriate choices for the matrices $\boldsymbol{N}^{\boldsymbol{i}}$. The following transformations are applied:

$$\boldsymbol{\chi}^{\boldsymbol{i}} = \boldsymbol{\xi}^{\boldsymbol{i}} - \overline{\boldsymbol{\tau}}_{\boldsymbol{\sigma}}^{\boldsymbol{i}}(\boldsymbol{w}, \boldsymbol{\mu}) - \frac{1}{b^i(\mu)} \boldsymbol{G}^{\boldsymbol{i}}\theta^i$$

The new coordinate shows the difference between the state vector of the internal model (5-38) and its augmented counterpart. By choosing $\boldsymbol{N}^{\boldsymbol{i}} = -\boldsymbol{K}^{\boldsymbol{i}}\boldsymbol{G}$, which simplifies the final equations, one can find the new form of closed loop system as

$$\begin{cases}\dot{\boldsymbol{\chi}} = \bar{\boldsymbol{F}}\boldsymbol{\chi} + \bar{\boldsymbol{F}}\bar{\boldsymbol{G}}\boldsymbol{B}(\boldsymbol{\mu})\boldsymbol{\theta} - \bar{\boldsymbol{G}}\boldsymbol{B}(\boldsymbol{\mu})\boldsymbol{\phi}(\tilde{\boldsymbol{z}}_{\boldsymbol{a}}, \boldsymbol{\theta}, \boldsymbol{w}, \boldsymbol{\rho}, \boldsymbol{k}) - \bar{\boldsymbol{G}}\boldsymbol{\Psi}_{\boldsymbol{\sigma}}(sat(\boldsymbol{\xi}) - \boldsymbol{\xi}) \\ \dot{\tilde{\boldsymbol{z}}}_{\boldsymbol{a}} = \boldsymbol{f}_{\boldsymbol{a}}(\tilde{\boldsymbol{z}}_{\boldsymbol{a}}, \boldsymbol{\theta}, \boldsymbol{w}, \boldsymbol{\rho}, \boldsymbol{k}) + \boldsymbol{G}_{\boldsymbol{a}}\boldsymbol{\theta} + \bar{\boldsymbol{C}}(\tilde{\boldsymbol{z}}, \tilde{\boldsymbol{x}}, \boldsymbol{w}, \boldsymbol{\mu})\big(\boldsymbol{\Psi}_{\boldsymbol{\sigma}} sat(\boldsymbol{\xi}) - \boldsymbol{K}\boldsymbol{\theta} - \boldsymbol{\Psi}_{\boldsymbol{\sigma}}\bar{\boldsymbol{\tau}}_{\boldsymbol{\sigma}}(\boldsymbol{w}, \boldsymbol{\mu})\big) \\ \dot{\boldsymbol{\theta}} = \boldsymbol{\phi}(\tilde{\boldsymbol{z}}_{\boldsymbol{a}}, \boldsymbol{\theta}, \boldsymbol{w}, \boldsymbol{\rho}, \boldsymbol{k}) + \boldsymbol{b}(\boldsymbol{\mu})\big(\boldsymbol{\Psi}_{\boldsymbol{\sigma}} sat(\boldsymbol{\xi}) - \boldsymbol{K}\boldsymbol{\theta} - \boldsymbol{\Psi}_{\boldsymbol{\sigma}}\bar{\boldsymbol{\tau}}_{\boldsymbol{\sigma}}(\boldsymbol{w}, \boldsymbol{\mu})\big)\end{cases} \quad 5\text{-}48$$

where $\bar{\boldsymbol{\tau}}_{\boldsymbol{\sigma}} = col\big(\bar{\boldsymbol{\tau}}_{\boldsymbol{\sigma}}^{\boldsymbol{1}}, \dots, \bar{\boldsymbol{\tau}}_{\boldsymbol{\sigma}}^{\boldsymbol{m}}\big)$ and $\boldsymbol{B}(\boldsymbol{\mu}) = diag\left(\frac{1}{b^1(\boldsymbol{\mu})}, \dots, \frac{1}{b^m(\boldsymbol{\mu})}\right)$. Now, by setting $\boldsymbol{\theta} = \boldsymbol{0}$, the system is converted to the form

$$\begin{cases}\dot{\boldsymbol{\chi}} = \bar{\boldsymbol{F}}\boldsymbol{\chi} - \bar{\boldsymbol{G}}\boldsymbol{B}(\boldsymbol{\mu})\boldsymbol{\phi}(\tilde{\boldsymbol{z}}_{\boldsymbol{a}}, \boldsymbol{0}, \boldsymbol{w}, \boldsymbol{\rho}, \boldsymbol{k}) - \bar{\boldsymbol{G}}\boldsymbol{\Psi}_{\boldsymbol{\sigma}}\left(sat\big(\boldsymbol{\chi} + \bar{\boldsymbol{\tau}}_{\boldsymbol{\sigma}}(\boldsymbol{w}, \boldsymbol{\mu})\big) - \boldsymbol{\chi} - \bar{\boldsymbol{\tau}}_{\boldsymbol{\sigma}}(\boldsymbol{w}, \boldsymbol{\mu})\right) \\ \dot{\tilde{\boldsymbol{z}}}_{\boldsymbol{a}} = \boldsymbol{f}_{\boldsymbol{a}}(\tilde{\boldsymbol{z}}_{\boldsymbol{a}}, \boldsymbol{0}, \boldsymbol{w}, \boldsymbol{\rho}, \boldsymbol{k}) + \bar{\boldsymbol{C}}(\tilde{\boldsymbol{z}}_{\boldsymbol{a}}, \boldsymbol{0} - \bar{\boldsymbol{\theta}}, \boldsymbol{w}, \boldsymbol{\mu})\boldsymbol{\Psi}_{\boldsymbol{\sigma}}\left(sat\big(\boldsymbol{\chi} + \bar{\boldsymbol{\tau}}_{\boldsymbol{\sigma}}(\boldsymbol{w}, \boldsymbol{\mu})\big) - \bar{\boldsymbol{\tau}}_{\boldsymbol{\sigma}}(\boldsymbol{w}, \boldsymbol{\mu})\right)\end{cases} \quad 5\text{-}49$$

Let us define the functions

$$\boldsymbol{h}(\tilde{\boldsymbol{z}}_{\boldsymbol{a}}, \boldsymbol{\chi}, \boldsymbol{w}, \boldsymbol{\rho}, \boldsymbol{k}) = \boldsymbol{f}_{\boldsymbol{a}}(\tilde{\boldsymbol{z}}_{\boldsymbol{a}}, \boldsymbol{0}, \boldsymbol{w}, \boldsymbol{\rho}, \boldsymbol{k}) - \bar{\boldsymbol{C}}(\tilde{\boldsymbol{z}}_{\boldsymbol{a}}, \boldsymbol{0} - \bar{\boldsymbol{\theta}}, \boldsymbol{w}, \boldsymbol{\mu})\boldsymbol{\Psi}_{\boldsymbol{\sigma}}\left(sat\big(\boldsymbol{\chi} + \bar{\boldsymbol{\tau}}_{\boldsymbol{\sigma}}(\boldsymbol{w}, \boldsymbol{\mu})\big) - \bar{\boldsymbol{\tau}}_{\boldsymbol{\sigma}}(\boldsymbol{w}, \boldsymbol{\mu})\right)$$

$$\boldsymbol{P}(\tilde{\boldsymbol{z}}_{\boldsymbol{a}}, \boldsymbol{\chi}, \boldsymbol{w}, \boldsymbol{\rho}, \boldsymbol{k}) = -\bar{\boldsymbol{G}}\boldsymbol{B}(\boldsymbol{\mu})\boldsymbol{\phi}(\tilde{\boldsymbol{z}}_{\boldsymbol{a}}, \boldsymbol{0}, \boldsymbol{w}, \boldsymbol{\rho}, \boldsymbol{k}) - \bar{\boldsymbol{G}}\boldsymbol{\Psi}_{\boldsymbol{\sigma}}\left(sat\big(\boldsymbol{\chi} + \bar{\boldsymbol{\tau}}_{\boldsymbol{\sigma}}(\boldsymbol{w}, \boldsymbol{\mu})\big) - \boldsymbol{\chi} - \bar{\boldsymbol{\tau}}_{\boldsymbol{\sigma}}(\boldsymbol{w}, \boldsymbol{\mu})\right)$$

By assuming that functions $\tilde{f}_r^i(\tilde{\boldsymbol{z}}_{\boldsymbol{a}}, -\bar{\boldsymbol{\theta}}, \boldsymbol{w}, \boldsymbol{\rho})$ are bounded, the following inequalities are concluded.

$$\|\boldsymbol{h}(\tilde{\boldsymbol{z}}_{\boldsymbol{a}}, \boldsymbol{\chi}, \boldsymbol{w}, \boldsymbol{\rho}, \boldsymbol{k}) - \boldsymbol{h}(\tilde{\boldsymbol{z}}_{\boldsymbol{a}}, \boldsymbol{0}, \boldsymbol{w}, \boldsymbol{\rho}, \boldsymbol{k})\| \leq \|\bar{\boldsymbol{C}}\|\|\boldsymbol{\Psi}_{\boldsymbol{\sigma}}\|\left\|sat\big(\boldsymbol{\chi} + \bar{\boldsymbol{\tau}}_{\boldsymbol{\sigma}}(\boldsymbol{w}, \boldsymbol{\mu})\big) - sat\big(\bar{\boldsymbol{\tau}}_{\boldsymbol{\sigma}}(\boldsymbol{w}, \boldsymbol{\mu})\big)\right\| \leq \gamma(\boldsymbol{\chi})$$

$$\|\boldsymbol{P}(\tilde{\boldsymbol{z}}_{\boldsymbol{a}}, \boldsymbol{\chi}, \boldsymbol{w}, \boldsymbol{\rho}, \boldsymbol{k})\| \leq \delta_1 + \delta_2\|\boldsymbol{\chi}\|$$

for some strictly positive real numbers δ_1, δ_2 and a bounded continuous function γ. With respect to the fact that the system (5-44) satisfies the ULP assumption, the conditions of Lemma 5.4 are observed, and the augmented system (5-49) admits a continuously differentiable positive definite function on $\{\tilde{\boldsymbol{z}}_{\boldsymbol{a}}: W_1(\tilde{\boldsymbol{z}}_{\boldsymbol{a}}) < c + 1\} \times \{\boldsymbol{\chi}: U_2(\boldsymbol{\chi}) < e_1(L) + 1\}$ as

$$W_2(\tilde{\boldsymbol{z}}_{\boldsymbol{a}}, \boldsymbol{\chi}) = c\frac{W_1(\tilde{\boldsymbol{z}}_{\boldsymbol{a}})}{c + 1 - W_1(\tilde{\boldsymbol{z}}_{\boldsymbol{a}})} + e_1(L)\frac{U_2(\boldsymbol{\chi})}{e_1(L) + 1 - U_2(\boldsymbol{\chi})}$$

where $e_1(L) > 1$ is a strictly positive class-K_∞ function defined in Lemma 5.4, $U_2(\boldsymbol{\chi}) = ln\big(1 + \boldsymbol{\chi}^{\boldsymbol{T}}\boldsymbol{P}_{\boldsymbol{0}}\boldsymbol{\chi}\big)$, $\bar{\boldsymbol{F}} = L\boldsymbol{A}_{\boldsymbol{0}}$, and $\boldsymbol{P}_{\boldsymbol{0}}$ satisfies $\boldsymbol{A}_{\boldsymbol{0}}^{\boldsymbol{T}}\boldsymbol{P}_{\boldsymbol{0}} + \boldsymbol{P}_{\boldsymbol{0}}\boldsymbol{A}_{\boldsymbol{0}} = -\boldsymbol{I}$. Moreover, for some finite positive number
$R_1 > R_2 > 0$, there exists real numbers $\boldsymbol{L}_* > 0$ such that for any $\boldsymbol{L} > \boldsymbol{L}_*$, the function W_2 has the properties:

1. The set $\mathcal{U}_2 = \{(\tilde{\boldsymbol{z}}_{\boldsymbol{a}}, \boldsymbol{\chi}): W_2(\tilde{\boldsymbol{z}}_{\boldsymbol{a}}, \boldsymbol{\chi}) < \bar{c} + 1\}$ is compact containing the set $\bar{\mathcal{B}}_{\mathrm{R}_2}$ where $\bar{c} = c^2 + \big(e_1(L)\big)^2$.
2. The function W_2 is positive definite on its domain.
3. For some positive numbers $e_1, e_2, r_2 < r_1$, the estimate $e_1\|(\tilde{\boldsymbol{z}}_{\boldsymbol{a}}, \boldsymbol{\chi})\|^2 \leq W_2(\tilde{\boldsymbol{z}}_{\boldsymbol{a}}, \boldsymbol{\chi}) \leq e_2\|(\tilde{\boldsymbol{z}}_{\boldsymbol{a}}, \boldsymbol{\chi})\|^2$ holds for any $(\tilde{\boldsymbol{z}}_{\boldsymbol{a}}, \boldsymbol{\chi}) \in \mathcal{B}_{r_2}$.
4. $\dot{W}_2 < -\alpha_2(\tilde{\boldsymbol{z}}_{\boldsymbol{a}}, \boldsymbol{\chi})$ for any $(\tilde{\boldsymbol{z}}_{\boldsymbol{a}}, \boldsymbol{\chi}) \in \mathcal{U}_2$, $\boldsymbol{w}^{\boldsymbol{0}} \in \mathcal{K}_w$, and $\boldsymbol{\rho} \in \mathcal{R}$, in which $\alpha_2(.)$ is a positive definite function satisfying $\alpha_2(\tilde{\boldsymbol{z}}_{\boldsymbol{a}}, \boldsymbol{\chi}) \geq l\|(\tilde{\boldsymbol{z}}_{\boldsymbol{a}}, \boldsymbol{\chi})\|^2$, for some $l > 0$.

As a result, the ULP assumption is held for the system in (5-49).Two further steps will complete the proof of closed loop system stability.

First, it is assumed that the zero dynamics of the system is unforced; therefore, in new coordinate system, it has the form

$$\begin{cases} \dot{\boldsymbol{\chi}} = \bar{\boldsymbol{F}}\boldsymbol{\chi} + \bar{\boldsymbol{F}}\bar{\boldsymbol{G}}\boldsymbol{B}(\boldsymbol{\mu})\boldsymbol{\theta} - \bar{\boldsymbol{G}}\boldsymbol{B}(\boldsymbol{\mu})\boldsymbol{\phi}(\tilde{\boldsymbol{z}}_{\boldsymbol{a}}, \boldsymbol{\theta}, \boldsymbol{w}, \boldsymbol{\rho}, \boldsymbol{k}) - \bar{\boldsymbol{G}}\boldsymbol{\Psi}_{\boldsymbol{\sigma}}(sat(\boldsymbol{\xi}) - \boldsymbol{\xi}) \\ \dot{\tilde{\boldsymbol{z}}}_{\boldsymbol{a}} = \boldsymbol{f}_{\boldsymbol{a}}(\tilde{\boldsymbol{z}}_{\boldsymbol{a}}, \boldsymbol{\theta}, \boldsymbol{w}, \boldsymbol{\rho}, \boldsymbol{k}) + \boldsymbol{G}_{\boldsymbol{a}}\boldsymbol{\theta} \\ \dot{\boldsymbol{\theta}} = -\boldsymbol{b}(\boldsymbol{\mu})\boldsymbol{K}\boldsymbol{\theta} + \boldsymbol{\phi}(\tilde{\boldsymbol{z}}_{\boldsymbol{a}}, \boldsymbol{\theta}, \boldsymbol{w}, \boldsymbol{\rho}, \boldsymbol{k}) + \boldsymbol{b}(\boldsymbol{\mu})\big(\boldsymbol{\Psi}_{\boldsymbol{\sigma}} sat(\boldsymbol{\xi}) - \boldsymbol{\Psi}_{\boldsymbol{\sigma}}\bar{\boldsymbol{\tau}}_{\boldsymbol{\sigma}}(\boldsymbol{w}, \boldsymbol{\mu})\big) \end{cases} \quad 5\text{-}50$$

Then, similar to the previous step, the key functions are defined as

$$\boldsymbol{h}(\tilde{\boldsymbol{z}}_{\boldsymbol{a}}, \boldsymbol{\chi}, \boldsymbol{\theta}, \boldsymbol{w}, \boldsymbol{\rho}, \boldsymbol{k}) = \begin{cases} \bar{\boldsymbol{F}}\boldsymbol{\chi} + \bar{\boldsymbol{F}}\bar{\boldsymbol{G}}\boldsymbol{B}(\boldsymbol{\mu})\boldsymbol{\theta} - \bar{\boldsymbol{G}}\boldsymbol{B}(\boldsymbol{\mu})\boldsymbol{\phi}(\tilde{\boldsymbol{z}}_{\boldsymbol{a}}, \boldsymbol{\theta}, \boldsymbol{w}, \boldsymbol{\rho}, \boldsymbol{k}) - \bar{\boldsymbol{G}}\boldsymbol{\Psi}_{\boldsymbol{\sigma}}(sat(\boldsymbol{\xi}) - \boldsymbol{\xi}) \\ \boldsymbol{f}_{\boldsymbol{a}}(\tilde{\boldsymbol{z}}_{\boldsymbol{a}}, \boldsymbol{\theta}, \boldsymbol{w}, \boldsymbol{\rho}, \boldsymbol{k}) + \boldsymbol{G}_{\boldsymbol{a}}\boldsymbol{\theta} \end{cases}$$

$$\boldsymbol{P}(\tilde{\boldsymbol{z}}_{\boldsymbol{a}}, \boldsymbol{\chi}, \boldsymbol{\theta}, \boldsymbol{w}, \boldsymbol{\rho}, \boldsymbol{k}) = \boldsymbol{\phi}(\tilde{\boldsymbol{z}}_{\boldsymbol{a}}, \boldsymbol{\theta}, \boldsymbol{w}, \boldsymbol{\rho}, \boldsymbol{k}) + \boldsymbol{b}(\boldsymbol{\mu})\big(\boldsymbol{\Psi}_{\boldsymbol{\sigma}} sat(\boldsymbol{\xi}) - \boldsymbol{\Psi}_{\boldsymbol{\sigma}}\bar{\boldsymbol{\tau}}_{\boldsymbol{\sigma}}(\boldsymbol{w}, \boldsymbol{\mu})\big)$$

Let assume that the deviation from reference trajectory is limited to a compact set and thus bounded and, for a continuous function γ_0,

$$\|\boldsymbol{\phi}(\tilde{\boldsymbol{z}}_{\boldsymbol{a}}, \boldsymbol{\theta}, \boldsymbol{w}, \boldsymbol{\rho}, \boldsymbol{k}) - \boldsymbol{\phi}(\tilde{\boldsymbol{z}}_{\boldsymbol{a}}, \boldsymbol{0}, \boldsymbol{w}, \boldsymbol{\rho}, \boldsymbol{k})\| \leq \gamma_0(\boldsymbol{\theta})$$

Then, it is concluded that, for some strictly positive real numbers δ_1, δ_2 and a bounded continuous function γ,

$$\|\boldsymbol{h}(\tilde{\boldsymbol{z}}_{\boldsymbol{a}}, \boldsymbol{\chi}, \boldsymbol{\theta}, \boldsymbol{w}, \boldsymbol{\rho}, \boldsymbol{k}) - \boldsymbol{h}(\tilde{\boldsymbol{z}}_{\boldsymbol{a}}, \boldsymbol{\chi}, \boldsymbol{0}, \boldsymbol{w}, \boldsymbol{\rho}, \boldsymbol{k})\| \leq \gamma(\boldsymbol{\theta})$$

$$\|\boldsymbol{P}(\tilde{\boldsymbol{z}}_{\boldsymbol{a}}, \boldsymbol{\chi}, \boldsymbol{w}, \boldsymbol{\rho}, \boldsymbol{k})\| \leq \delta_1 + \delta_2\|\boldsymbol{\theta}\|$$

In addition, the ULP assumption is preserved when $\boldsymbol{\theta} = \boldsymbol{0}$; then, the conditions of Lemma 5.4 are preserved, and a continuously differentiable positive definite function can be defined on $\{\tilde{\boldsymbol{z}}_{\boldsymbol{a}}: W_1(\tilde{\boldsymbol{z}}_{\boldsymbol{a}}) < c + 1\} \times \{\boldsymbol{\chi}: U_2(\boldsymbol{\chi}) < e_1(L) + 1\} \times \{\boldsymbol{\theta}: U_3(\boldsymbol{\theta}) < e_2(\bar{L}) + 1\}$as

$$W_3(\tilde{\boldsymbol{z}}_{\boldsymbol{a}}, \boldsymbol{\chi}, \boldsymbol{\theta}) = W_2(\tilde{\boldsymbol{z}}_{\boldsymbol{a}}, \boldsymbol{\chi}) + e_2(\bar{L})\frac{U_3(\boldsymbol{\theta})}{e_2(\bar{L}) + 1 - U_3(\boldsymbol{\theta})} +$$

where $e_2(\bar{L}) > 1$ is a strictly positive class-K_∞ function, $U_3(\boldsymbol{\theta}) = ln\big(1 + \boldsymbol{\theta}^{\boldsymbol{T}}\boldsymbol{P}_{\boldsymbol{0}}\boldsymbol{\theta}\big)$, $-\boldsymbol{b}(\boldsymbol{\mu})\boldsymbol{K} = \bar{L}\boldsymbol{A}_{\boldsymbol{0}}$, and $\boldsymbol{P}_{\boldsymbol{0}}$ satisfies $\boldsymbol{A}_{\boldsymbol{0}}^{\boldsymbol{T}}\boldsymbol{P}_{\boldsymbol{0}} + \boldsymbol{P}_{\boldsymbol{0}}\boldsymbol{A}_{\boldsymbol{0}} = -\boldsymbol{I}$. Moreover, for some finite positive number $R_2 > R_3 > 0$, there exists real number $\bar{\boldsymbol{L}}_* > 0$ such that for any $\bar{\boldsymbol{L}} > \bar{\boldsymbol{L}}_*$, the function W_3 has the properties:

1. The set $\mathcal{U}_3 = \{(\tilde{\boldsymbol{z}}_{\boldsymbol{a}}, \boldsymbol{\chi}, \boldsymbol{\theta}): W_3(\tilde{\boldsymbol{z}}_{\boldsymbol{a}}, \boldsymbol{\chi}, \boldsymbol{\theta}) < \bar{c} + 1\}$ is compact containing the set $\bar{\mathcal{B}}_{\mathrm{R}_3}$.
2. The function W_3 is positive definite on its domain.
3. For some positive numbers $e_1, e_2, r_3 < r_2$, the estimate $e_1\|(\tilde{\boldsymbol{z}}_{\boldsymbol{a}}, \boldsymbol{\chi}, \boldsymbol{\theta})\|^2 \leq W_2(\tilde{\boldsymbol{z}}_{\boldsymbol{a}}, \boldsymbol{\chi}, \boldsymbol{\theta}) \leq e_2\|(\tilde{\boldsymbol{z}}_{\boldsymbol{a}}, \boldsymbol{\chi}, \boldsymbol{\theta})\|^2$ holds for any $(\tilde{\boldsymbol{z}}_{\boldsymbol{a}}, \boldsymbol{\chi}, \boldsymbol{\theta}) \in \mathcal{B}_{r_3}$.
4. $\dot{W}_3 < -\alpha_3(\tilde{\boldsymbol{z}}_{\boldsymbol{a}}, \boldsymbol{\chi}, \boldsymbol{\theta})$ for any $(\tilde{\boldsymbol{z}}_{\boldsymbol{a}}, \boldsymbol{\chi}, \boldsymbol{\theta}) \in \mathcal{U}_3$, $\boldsymbol{w}^{\boldsymbol{0}} \in \mathcal{K}_w$, and $\boldsymbol{\rho} \in \mathcal{R}$, in which $\alpha_3(.)$ is a positive definite function satisfying $\alpha_2(\tilde{\boldsymbol{z}}_{\boldsymbol{a}}, \boldsymbol{\chi}) \geq l\|(\tilde{\boldsymbol{z}}_{\boldsymbol{a}}, \boldsymbol{\chi})\|^2$, for some $l > 0$.

The proof of asymptotic stability is completed when the system zero dynamics is unforced. The next step is to enter the effect of control term in the zero dynamics equation. On the other hand, one can use Lemma Corollary 5.2 to prove the stability when there is no boundary on the deviation from reference trajectory. In this case the function U_3 is redefined as $U_3(\boldsymbol{\theta}) = 1 + \boldsymbol{\theta}^T \boldsymbol{P_0} \boldsymbol{\theta}$.

The analysis of the control effect on zero dynamics is initiated by some basic assumptions. Since the zero dynamics is assumed to be locally exponentially stable, there exists some strictly positive number r_0 such that $\frac{\partial V_0(\tilde{\boldsymbol{z}})}{\partial \tilde{\boldsymbol{z}}} \tilde{\boldsymbol{f}}_{\boldsymbol{0}}(\tilde{\boldsymbol{z}}, \boldsymbol{0}, \boldsymbol{w}, \boldsymbol{\mu}) \leq -l_0 \|\tilde{\boldsymbol{z}}\|^2$ on the open set $\mathcal{B}_{r_0}$ where $l_0 \propto \left.\frac{\partial \tilde{\boldsymbol{f}}_{\boldsymbol{0}}(\tilde{\boldsymbol{z}}, \boldsymbol{0}, \boldsymbol{w}, \boldsymbol{\mu})}{\partial \tilde{\boldsymbol{z}}}\right|_{\tilde{\boldsymbol{z}}=\boldsymbol{0}}$. In fact, the control signal is composed of two terms, $\overline{\boldsymbol{C}}(\tilde{\boldsymbol{z}}, \widetilde{\boldsymbol{x}}, \boldsymbol{w}, \boldsymbol{\mu}) \boldsymbol{\Psi}_{\boldsymbol{\sigma}}\big(sat(\boldsymbol{\xi}) - \overline{\boldsymbol{\tau}}_{\boldsymbol{\sigma}}(\boldsymbol{w}, \boldsymbol{\mu})\big)$ and $-\overline{\boldsymbol{C}}(\tilde{\boldsymbol{z}}, \widetilde{\boldsymbol{x}}, \boldsymbol{w}, \boldsymbol{\mu}) \boldsymbol{K} \boldsymbol{\theta}$, which appeared in the time derivative of the Lyapunov function. While the first term can be compensated for by other terms, with respect to Lemma 5.2, the second term eliminates the region of attraction. Given the same Lyapunov function as the previous step, it admits the time derivative reformulated as

$$\dot{W}_3 \leq -l_0 \|\tilde{\boldsymbol{z}}\|^2 - l_1 \bar{\alpha}_1(\widetilde{\boldsymbol{x}}_{\boldsymbol{a}}) - l_2 \bar{\alpha}_2(\boldsymbol{\chi}) - l_3 \boldsymbol{\theta}^{\boldsymbol{T}} \boldsymbol{\theta} + \left\| \frac{\partial \boldsymbol{V_0}(\tilde{\boldsymbol{z}})}{\partial \tilde{\boldsymbol{z}}} \right\| \|\boldsymbol{C}\| \|\boldsymbol{K}\| \|\boldsymbol{\theta}\| + \boldsymbol{2} \|\boldsymbol{\theta}\| \|\boldsymbol{P_0}\| \|\boldsymbol{\phi}\|$$

on the open set $\mathcal{B}_r$ where $r = min(r_0, r_3)$. Let $\left\| \frac{\partial \boldsymbol{V_0}(\tilde{\boldsymbol{z}})}{\partial \tilde{\boldsymbol{z}}} \right\| \leq l_4 \|\tilde{\boldsymbol{z}}\|$, and

$$\|\boldsymbol{\phi}\| \leq l_5^1 \|\tilde{\boldsymbol{z}}\| + l_5^2 \|(\widetilde{\boldsymbol{x}}_{\boldsymbol{a}}, \boldsymbol{\chi})\| + l_5^3 \|\boldsymbol{\theta}\|$$

on the open set $\mathcal{B}_{\bar{r}} \subseteq \mathcal{B}_r$, where

$$l_5^1 = \left\| \left. \frac{\partial \boldsymbol{\phi}}{\partial \tilde{\boldsymbol{z}}} \right|_{(\tilde{\boldsymbol{z}}_{\boldsymbol{a}}, \boldsymbol{\chi}, \boldsymbol{\theta}) = \boldsymbol{0}} \right\|, \; l_5^2 = \left\| \left. \frac{\partial \boldsymbol{\phi}}{\partial (\widetilde{\boldsymbol{x}}_{\boldsymbol{a}}, \boldsymbol{\chi})} \right|_{(\tilde{\boldsymbol{z}}_{\boldsymbol{a}}, \boldsymbol{\chi}, \boldsymbol{\theta}) = \boldsymbol{0}} \right\|, \text{ and } l_5^3 = \left\| \left. \frac{\partial \boldsymbol{\phi}}{\partial \boldsymbol{\theta}} \right|_{(\tilde{\boldsymbol{z}}_{\boldsymbol{a}}, \boldsymbol{\chi}, \boldsymbol{\theta}) = \boldsymbol{0}} \right\|$$

Under this condition, one can conclude that

$$\begin{aligned} \dot{W}_3 \leq -l_0 \|\tilde{\boldsymbol{z}}\|^2 - l_1 \bar{\alpha}_1(\widetilde{\boldsymbol{x}}_{\boldsymbol{a}}) - l_2 \bar{\alpha}_2(\boldsymbol{\chi}) - \big(l_3 - 2 l_5^3 \|\boldsymbol{P_0}\|\big) \boldsymbol{\theta}^{\boldsymbol{T}} \boldsymbol{\theta} + 2 l_5^2 \|\boldsymbol{P_0}\| \|(\widetilde{\boldsymbol{x}}_{\boldsymbol{a}}, \boldsymbol{\chi})\| \|\boldsymbol{\theta}\| \\ + (2 l_5^1 \|\boldsymbol{P_0}\| + l_4 \|\boldsymbol{C}\| \|\boldsymbol{K}\|) \|\boldsymbol{\theta}\| \|\tilde{\boldsymbol{z}}\| \end{aligned} \quad \text{5-51}$$

Afterwards, since $\|(\widetilde{\boldsymbol{x}}_{\boldsymbol{a}}, \boldsymbol{\chi})\| \|\boldsymbol{\theta}\| = \boldsymbol{0}$ for $\forall (\tilde{\boldsymbol{z}}, \widetilde{\boldsymbol{x}}_{\boldsymbol{a}}, \boldsymbol{\chi}, \boldsymbol{\theta}) \in \{(\tilde{\boldsymbol{z}}, \widetilde{\boldsymbol{x}}_{\boldsymbol{a}}, \boldsymbol{\chi}, \boldsymbol{\theta}) \in \boldsymbol{\mathcal{B}}_{\bar{\boldsymbol{r}}} | (\widetilde{\boldsymbol{x}}_{\boldsymbol{a}}, \boldsymbol{\chi}, \boldsymbol{\theta}) = \boldsymbol{0}\}$, the Lemma 5.2 is applied when the sets are defined as the intersection of $\overline{\mathcal{B}}_{\bar{r}} \subset \mathcal{B}_{\bar{r}}$ and the previous employed compact sets. The inequality (5-51) is transformed to the form

5-52

$$\dot{W}_3 \leq -\frac{l_1}{2} \bar{\alpha}_1(\widetilde{\boldsymbol{x}}_{\boldsymbol{a}}) - \frac{l_2}{2} \bar{\alpha}_2(\boldsymbol{\chi}) - l_0 \|\tilde{\boldsymbol{z}}\|^2 - \frac{\big(l_3 - 2 l_5^3 \|\boldsymbol{P_0}\|\big)}{2} \|\boldsymbol{\theta}\|^2 + (2 l_5^1 \|\boldsymbol{P_0}\| + l_4 \|\boldsymbol{C}\| \|\boldsymbol{K}\|) \|\boldsymbol{\theta}\| \|\tilde{\boldsymbol{z}}\|$$

Finally, if the condition

$$2 \sqrt{\frac{(l_3 - 2 l_5^3 \|\boldsymbol{P_0}\|)}{2} l_0} > (2 l_5^1 \|\boldsymbol{P_0}\| + l_4 \|\boldsymbol{C}\| \|\boldsymbol{K}\|) \quad \text{5-53}$$

then the inequality (5-52) takes the form

$$\dot{W}_3 \leq -\bar{l}_0\|\tilde{\boldsymbol{z}}\|^2 - \frac{l_1}{2}\bar{\alpha}_1(\tilde{\boldsymbol{x}}_{\boldsymbol{a}}) - \frac{l_2}{2}\bar{\alpha}_2(\boldsymbol{\chi}) - \bar{l}_3\|\boldsymbol{\theta}\|^2 - \bar{l}_4(\|\boldsymbol{\theta}\| - \|\tilde{\boldsymbol{z}}\|)^2$$

In fact, $\boldsymbol{P_0}$ can be chosen in such a way that $\boldsymbol{K^T P_0 + P_0 K = -\beta l_3 I}$ where β is a constant number. Therefore, the condition (5-53) is observed under either of the following conditions.

1. The gradient $\frac{\partial \tilde{\boldsymbol{f}}_{\boldsymbol{0}}(\tilde{\boldsymbol{z}},\boldsymbol{0},\boldsymbol{w},\boldsymbol{\mu})}{\partial \tilde{\boldsymbol{z}}}\Big|_{\tilde{\boldsymbol{z}}=\boldsymbol{0}}$ admits much greater norm value than l_3,
2. The gradients $\frac{\partial \boldsymbol{\phi}}{\partial \tilde{\boldsymbol{z}}}\Big|_{(\tilde{\boldsymbol{z}}_{\boldsymbol{a}},\boldsymbol{\chi},\boldsymbol{\theta})=\boldsymbol{0}}$ and $\frac{\partial \boldsymbol{\phi}}{\partial \boldsymbol{\theta}}\Big|_{(\tilde{\boldsymbol{z}}_{\boldsymbol{a}},\boldsymbol{\chi},\boldsymbol{\theta})=\boldsymbol{0}}$ admits ignorable norm values.

All in all, the stability of the closed loop system is proven, and the following theorem summarizes the result of this subsection.

Theorem 5.1: Suppose the parameter σ of the exosystem is known. Denote the errors and their j^{th} derivatives with $e_i^{(j)}$, $j = 1, \dots, r_i$. There exist the vectors of positive real values $\boldsymbol{k}_*$ and $\boldsymbol{K}_*$ and a Hurwitz matrix $\overline{\boldsymbol{F}}$ such that, for $\boldsymbol{k} > \boldsymbol{k}_*$ and $\boldsymbol{K} > \boldsymbol{K}_*$, the dynamic controller

$$\begin{cases} \dot{\boldsymbol{\xi}}^{\boldsymbol{1}} = \left(\boldsymbol{F^1} + \boldsymbol{G^1}\boldsymbol{\Psi}_{\boldsymbol{\sigma}}^{\boldsymbol{1}}\right)\boldsymbol{\xi^1} - K^1\boldsymbol{G^1}\left(e_1^{(r_1-1)} + (k^1)^{r_1-1}b_0^1 e_1 + \cdots + k^1 b_{r_1-2}^1 e_1^{r_1-2}\right) \\ \vdots \\ \dot{\boldsymbol{\xi}}^{\boldsymbol{m}} = (\boldsymbol{F^m} + \boldsymbol{G^m}\boldsymbol{\Psi}_{\boldsymbol{\sigma}}^{\boldsymbol{m}})\boldsymbol{\xi^m} - K^m\boldsymbol{G^m}\left(e_m^{(r_m-1)} + (k^m)^{r_m-1}b_0^m e_m + \cdots + k^m b_{r_m-2}^m e_m^{r_m-2}\right) \end{cases}$$

$$\boldsymbol{v} = \begin{pmatrix} \boldsymbol{\Psi}_{\boldsymbol{\sigma}}^{\boldsymbol{1}}\boldsymbol{\xi^1} - K^1\left(e_1^{(r_1-1)} + (k^1)^{r_1-1}b_0^1 e_1 + \cdots + k^1 b_{r_1-2}^1 e_1^{r_1-2}\right) \\ \vdots \\ \boldsymbol{\Psi}_{\boldsymbol{\sigma}}^{\boldsymbol{m}}\boldsymbol{\xi^m} - K^m\left(e_1^{(r_m-1)} + (k^m)^{r_m-1}b_0^m e_m + \cdots + k^m b_{r_m-2}^m e_m^{r_m-2}\right) \end{pmatrix}$$

solves the problem of local robust output regulation for the class of system considered before.

In general, the parameters $\boldsymbol{k}_*$, $\boldsymbol{K}_*$, and $\overline{\boldsymbol{F}}$ are set depending on the compact set chosen for the initial conditions of the plant and exosystem as well as the compact sets initiated for the uncertainties. As the sizes of these compact sets are increased, the required values for these parameters are also amplified. Although a closed formula relating these parameters to the defined compact sets cannot be found, the theorem 5.1 shows the infinite margins for the closed loop system with respect to the gain parameters $\boldsymbol{k}$ and $\boldsymbol{K}$.

5.3.4 Tuning the internal model

In the previous section, the regulation controller is designed with the assumption that the parameters of the exosystem are exactly known. This is the case when exogenous inputs are constant or sinusoidal signals of known frequency and unknown either amplitude or phase. On the other hand, if the frequencies are unknown, asymptotic estimate of the frequencies of the exogenous signal is required. The adaptive version of the previous section controller is shown to effectively solve the robust regulation problem.

The parameters of the exosystem is assumed to be unknown, and are supposed to be estimated with the assumption that $q_i, 1 \leq i \leq m$ (addressed in assumption 5.2) are even. Moreover, $\boldsymbol{\Phi^i}(\boldsymbol{\sigma})$ should

admit nonzero complex eigenvalues. It is also assumed that the exosystem is stimulated with an initial condition exiting all the mode of $\left(\boldsymbol{F^i}+\boldsymbol{\Psi_\sigma^i G^i}\right)$. With respect to the principle of uncertainty equivalence, the $\boldsymbol{\Psi_\sigma^i}$ can be replaced with its estimate $\boldsymbol{\hat{\Psi}^i}$ governed by the adaptation law of the form

$$\frac{d}{dt}\boldsymbol{\hat{\Psi}^i}=\boldsymbol{\varphi^i}\left(\boldsymbol{\xi^i},\theta^i\right)$$

for $1\le i\le m$. The internal model is then takes the form

$$\boldsymbol{\dot{\xi}}=\left(\boldsymbol{\bar{F}}+\boldsymbol{\bar{G}\hat{\Psi}}\right)\boldsymbol{\xi}+\boldsymbol{\bar{N}\theta}$$
$$\boldsymbol{v_{im}}=\boldsymbol{\hat{\Psi}\xi}$$

By considering $\boldsymbol{\bar{\Psi}}=\boldsymbol{\hat{\Psi}}-\boldsymbol{\Psi_\sigma}$, the closed loop system converts to the form

$$\begin{cases}\dot{\boldsymbol{\chi}}=\boldsymbol{\bar{F}\chi}+\boldsymbol{\bar{F}\bar{G}B(\mu)\theta}-\boldsymbol{\bar{G}B(\mu)\phi}(\boldsymbol{\tilde{z}_a},\boldsymbol{\theta},\boldsymbol{w},\boldsymbol{\rho},\boldsymbol{k})-\boldsymbol{\bar{G}}\left(\boldsymbol{\hat{\Psi}}-\boldsymbol{\bar{\Psi}}\right)(sat(\boldsymbol{\xi})-\boldsymbol{\xi})\\ \dot{\boldsymbol{\tilde{z}}}_{\boldsymbol{a}}=\boldsymbol{f_a}(\boldsymbol{\tilde{z}_a},\boldsymbol{\theta},\boldsymbol{w},\boldsymbol{\rho},\boldsymbol{k})+\boldsymbol{G_a\theta}+\boldsymbol{\bar{C}}(\boldsymbol{\tilde{z}},\boldsymbol{\tilde{x}},\boldsymbol{w},\boldsymbol{\mu})\left(\boldsymbol{\Psi_\sigma}sat(\boldsymbol{\xi})-\boldsymbol{K\theta}-\boldsymbol{\Psi_\sigma\bar{\tau}_\sigma}(\boldsymbol{w},\boldsymbol{\mu})+\boldsymbol{\bar{\Psi}sat}(\boldsymbol{\xi})\right)\\ \dot{\boldsymbol{\theta}}=\boldsymbol{\phi}(\boldsymbol{\tilde{z}_a},\boldsymbol{\theta},\boldsymbol{w},\boldsymbol{\rho},\boldsymbol{k})+\boldsymbol{b}(\boldsymbol{\mu})\left(\boldsymbol{\Psi_\sigma}sat(\boldsymbol{\xi})-\boldsymbol{K\theta}-\boldsymbol{\Psi_\sigma\bar{\tau}_\sigma}(\boldsymbol{w},\boldsymbol{\mu})+\boldsymbol{\bar{\Psi}sat}(\boldsymbol{\xi})\right)\\ \dot{\bar{\boldsymbol{\Psi}}}=\boldsymbol{\varphi}(\boldsymbol{\xi},\boldsymbol{\theta})\end{cases} \quad 5\text{-}54$$

where $\boldsymbol{\bar{\Psi}}$ and $\boldsymbol{\varphi}(\boldsymbol{\xi},\boldsymbol{\theta})$ are the matrices constructed in the same way as $\boldsymbol{\Psi_\sigma}$. Since the parameters of exosystem change within a compact set, the initial values for $\boldsymbol{\bar{\Psi}}$ are also chosen from a compact set. In the closed loop system (5-54) the state vector $\boldsymbol{\xi}$ is left unchanged to help find a proper adaptation law.

The smooth Lyapunov function employed to construct the adaptation law has the form, the letter γ is borrowed to define the constant numbers.

$$W(\boldsymbol{\chi},\boldsymbol{\tilde{z}_a},\boldsymbol{\theta},\boldsymbol{\bar{\Psi}})=W_3(\boldsymbol{\chi},\boldsymbol{\tilde{z}_a},\boldsymbol{\theta})+\frac{1}{2\gamma_0}trace(\boldsymbol{b}(\boldsymbol{\mu})\boldsymbol{\bar{\Psi}\bar{\Psi}^T})$$

Let function W be defined on the open set $\mathcal{B}_{\bar{r}}$. Then, the time derivative of this function can be written as

$$\dot{W}\le-\bar{\alpha}(\boldsymbol{\chi},\boldsymbol{\tilde{z}_a},\boldsymbol{\theta})+\sum_{i=1}^{m}b^i\boldsymbol{\bar{\Psi}^i}\left[\gamma_i\theta^i sat\left(\boldsymbol{\xi^i}\right)+\frac{1}{\gamma_0}\left(\boldsymbol{\varphi^i}\left(\boldsymbol{\xi^i},\theta^i\right)\right)^T\right]+\gamma_{m+1}\left(\boldsymbol{C\bar{\Psi}}sat(\boldsymbol{\xi})\right)^T\frac{\partial V_0}{\partial\boldsymbol{\tilde{z}}} \quad 5\text{-}55$$

where $\bar{\alpha}(.)$ is positive definite on $\mathcal{B}_{\bar{r}}$. Provided that $\boldsymbol{C\bar{\Psi}}sat(\boldsymbol{\xi})=\sum_{i=1}^{m}\boldsymbol{C_i\bar{\Psi}^i}sat\left(\boldsymbol{\xi^i}\right)$ in which $\boldsymbol{C_i}$ represents the i^{th} column of the matrix $\boldsymbol{C}$, one can set

$$\boldsymbol{\varphi^i}\left(\boldsymbol{\xi^i},\theta^i\right)=-\left(\bar{\gamma}_i\theta^i+\bar{\gamma}_{m+1}\boldsymbol{C_i}^T\frac{\partial V_0}{\partial\boldsymbol{\tilde{z}}}\right)sat\left(\left(\boldsymbol{\xi^i}\right)^T\right) \quad 5\text{-}56$$

As a result, the trajectory $\left(\boldsymbol{\chi}(\boldsymbol{t}),\boldsymbol{\tilde{z}_a}(\boldsymbol{t}),\boldsymbol{\theta}(\boldsymbol{t})\right)$ goes to zero by the La Salle theorem [54]. The results of this section can be summarized as the following theorem.

Theorem 5.2: Suppose the parameter σ of the exosystem is unknown. There exist the vectors of positive real values $\boldsymbol{k}_*$ and $\boldsymbol{K}_*$ and a Hurwitz matrix $\boldsymbol{\bar{F}}$ such that, for $\boldsymbol{k}>\boldsymbol{k}_*$ and $\boldsymbol{K}>\boldsymbol{K}_*$, the dynamic controller

$$
\begin{cases}
\dot{\boldsymbol{\xi}}^{\boldsymbol{1}} = \left(\boldsymbol{F^1} + \boldsymbol{G^1}\widehat{\boldsymbol{\Psi}}^{\boldsymbol{1}}\right)\boldsymbol{\xi^1} - K^1\boldsymbol{G^1}\left(e_1^{(r_1-1)} + (k^1)^{r_1-1}b_0^1 e_1 + \cdots + k^1 b_{r_1-2}^1 e_1^{r_1-2}\right) \\
\dfrac{d}{dt}\widehat{\boldsymbol{\Psi}}^{\boldsymbol{1}} = -\left(\bar{\gamma}_1\theta^1 + \bar{\gamma}_{m+1}\boldsymbol{C_1}^{\boldsymbol{T}}\dfrac{\partial V_0}{\partial \tilde{\boldsymbol{z}}}\right) sat\left(\left(\boldsymbol{\xi}^{\boldsymbol{1}}\right)^{\boldsymbol{T}}\right) \\
\vdots \\
\dot{\boldsymbol{\xi}}^{\boldsymbol{m}} = \left(\boldsymbol{F^m} + \boldsymbol{G^m}\widehat{\boldsymbol{\Psi}}^{\boldsymbol{m}}\right)\boldsymbol{\xi^m} - K^m\boldsymbol{G^m}\left(e_m^{(r_m-1)} + (k^m)^{r_m-1}b_0^m e_m + \cdots + k^m b_{r_m-2}^m e_m^{r_m-2}\right) \\
\dfrac{d}{dt}\widehat{\boldsymbol{\Psi}}^{\boldsymbol{m}} = -\left(\bar{\gamma}_m\theta^m + \bar{\gamma}_{m+1}\boldsymbol{C_m}^{\boldsymbol{T}}\dfrac{\partial V_0}{\partial \tilde{\boldsymbol{z}}}\right) sat\left((\boldsymbol{\xi}^{\boldsymbol{m}})^{\boldsymbol{T}}\right)
\end{cases}
$$

$$
v = \begin{pmatrix}
\widehat{\boldsymbol{\Psi}}^{\boldsymbol{1}}\boldsymbol{\xi^1} - K^1\left(e_1^{(r_1-1)} + (k^1)^{r_1-1}b_0^1 e_1 + \cdots + k^1 b_{r_1-2}^1 e_1^{r_1-2}\right) \\
\vdots \\
\widehat{\boldsymbol{\Psi}}^{\boldsymbol{m}}\boldsymbol{\xi^m} - K^m\left(e_1^{(r_m-1)} + (k^m)^{r_m-1}b_0^m e_m + \cdots + k^m b_{r_m-2}^m e_m^{r_m-2}\right)
\end{pmatrix}
$$

solves the problem of local robust output regulation for the class of system considered before.

At this point, the regulation control design is completed around a neighborhood of the reference trajectory. However, this control stabilizes the closed loop system semi-globally around the required trajectory when the zero dynamics is unforced. In this case, the second term is omitted from the right hand side of the adaptation equation. In fact, the control is applicable if the states of the zero dynamics states are measurable; otherwise, the zero dynamics must be unforced. While the zero dynamics is measurable, the coefficient $\bar{\gamma}_{m+1}$ in (5-56) can be chosen small enough to eliminate the effect of unobservable states in adaptation law. In the next section the simulation results are shown for the electromagnetic system illustrated in section 5.2.

5.4 Simulation results

In the previous sections, the problem of robust output regulation is addressed for a special class of multi-input multi-output systems when the exosystem parameters are unknown. In this section, the control design for the electromagnetic system defined in section 5.2 is illustrated. Since it is not easy to solve the equation (5-22) analytically, it is solved numerically for an estimated reference trajectory. Next, the solution is used to find the initial condition for the exosystem parameters. Two sets of experiments are accomplished, one without any noise and one with an augmented white noise to the output vector, to study the robustness of the designed control.

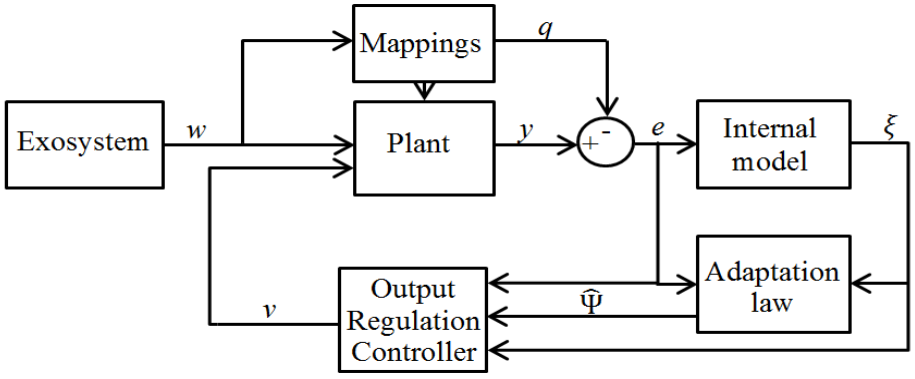

Figure 5-1: The block diagram of robust output regulation controller with adaptive internal model

The main concern of the control design is forcing a ferromagnetic particle to follow a path in a fluidic environment with constant velocity. The fluidic environment has the same characteristic as the example illustrated in chapter 3. Before advancing the regulation control operation, a saturated high-speed observer is introduced to estimates the error and its derivatives [55]. This observer is required since the derivatives are not measureable and has the form

$$\dot{\hat{\boldsymbol{e}}}^{\boldsymbol{i}} = \boldsymbol{M_g}\hat{\boldsymbol{e}}^{\boldsymbol{i}} + \boldsymbol{L_g}\boldsymbol{e}^{\boldsymbol{i}}$$

where

$$\boldsymbol{M_g} = \begin{pmatrix} -gc_1 & 1 \\ -g^2c_0 & 0 \end{pmatrix} \quad \boldsymbol{L_g} = \begin{pmatrix} gc_1 \\ g^2c_0 \end{pmatrix}$$

for $1 \leq i \leq 3$.

In order to proceed, the stability of the zero dynamics has to be investigated. As mentioned in the previous section, the zero dynamics should be asymptotically and locally exponentially stable around the mappings derived from (5-22); however, these mappings cannot be found analytically. Since this dynamics is set to minimize the energy, it is assumed to satisfy the requirement. In the next step, the order of exosystem should be defined, which is not analytically possible. By assuming a small value for the velocity vector, the derivatives of reference control mappings c_σ^i get smaller as the order of differentiation is increased. For the path studied in this section, the exosystem is obtained to be a second order ordinary differential equation.

First, the simulation is initiated for a third degree polynomial curve. The initial value for the matrices $\widehat{\boldsymbol{\Psi}}^{\boldsymbol{i}}$, for $1 \leq i \leq 3$, are chosen to be the same. The matrices $\boldsymbol{F}^{\boldsymbol{i}}$, for $1 \leq i \leq 3$, are chosen to have the set of eigenvalues $\{-6, -4\}$. The initial values

$$\boldsymbol{\Phi}^{\boldsymbol{i}}(\boldsymbol{\sigma}) = \begin{pmatrix} 0 & 1 \\ -0.018 & -0.018 \end{pmatrix}$$

for $1 \leq i \leq 3$, are chosen for the exosystem parameter to construct the triples $\left(\boldsymbol{F}^{\boldsymbol{i}}, \boldsymbol{G}^{\boldsymbol{i}}, \boldsymbol{\Psi}^{\boldsymbol{i}}_{\boldsymbol{\sigma_0}}\right)$ in the controllability canonical form. However, the elements of the row vectors $\boldsymbol{\Psi}^{\boldsymbol{i}}_{\boldsymbol{\sigma_0}}$ variation for different parameter σ values are large. In order to improve the numerical stability of the robust adaptive algorithm, a balanced realization is calculated from the canonical form [56]. In fact, the balanced realization employs a linear transformation to convert the controllability and observability Gramians of the system into the same diagonal matrices. Having defined this transformation, one can calculate the matrices $\boldsymbol{\Psi}^{\boldsymbol{i}}_{\boldsymbol{\sigma_0}}$ for the different exosystem parameter in the same coordinates system. For the set initial value these matrices are calculated as

$$\boldsymbol{\Psi}^{\boldsymbol{i}}_{\boldsymbol{\sigma_0}} = (-3.2 \quad -0.53)$$

It is assumed that an iron particle with permeability follows the path in a fluidic environment whose viscosity has the value of $0.0576\ Kg/(m\ s)$. The particle has a radius of $0.001\ mm$, and the augmented structure is employed to stimulate the particle movement with the velocity of magnitude $0.04\ {}^{cm}/_{S}$. Table 5-1 shows the system parameters used in this experiment. The controller gains and the observer parameter are chosen during the simulation process with no information about their exact value.

Table 5-1: The system parameters

k^i	K^i	$\bar{\gamma}_i$	$\bar{\gamma}_4$	g	b_0^i	c_0	c_1
1	100	2	0.001	100	1	2	3

In this example, the output neither is a sinusoidal function nor admits discrete major frequencies in the operating time period. Therefore, the convergence of exosystem parameters $\boldsymbol{\Psi}^{\boldsymbol{i}}_{\boldsymbol{\sigma_0}}$ is not the concern of this section. The simulation result for the deviation from a reference path of formula $x_1^2 = (x_1^1)^3$ on the plane $x_1^3 = 0$ is shown in Figure 5-2 as well as the control vector elements in Figure 5-3. Since the real inputs to the electromagnetic system are the currents, the states of zero dynamics, the second norm of current vector is depicted in Figure 5-4.The initial condition is $X_1 = (-1.05, -0.8, 0)\ cm, X_2 = (0.01, 0.02, 0)\ cm/s$. It is observed that the magnitude of each control signal vanish after a period of steep variations, and a low frequency oscillation is initiated. In fact, the frequency is not required to be a fixed value, since the exosystem parameters are updating as time passes. More importantly, the errors converge to zero with bounded current vector.

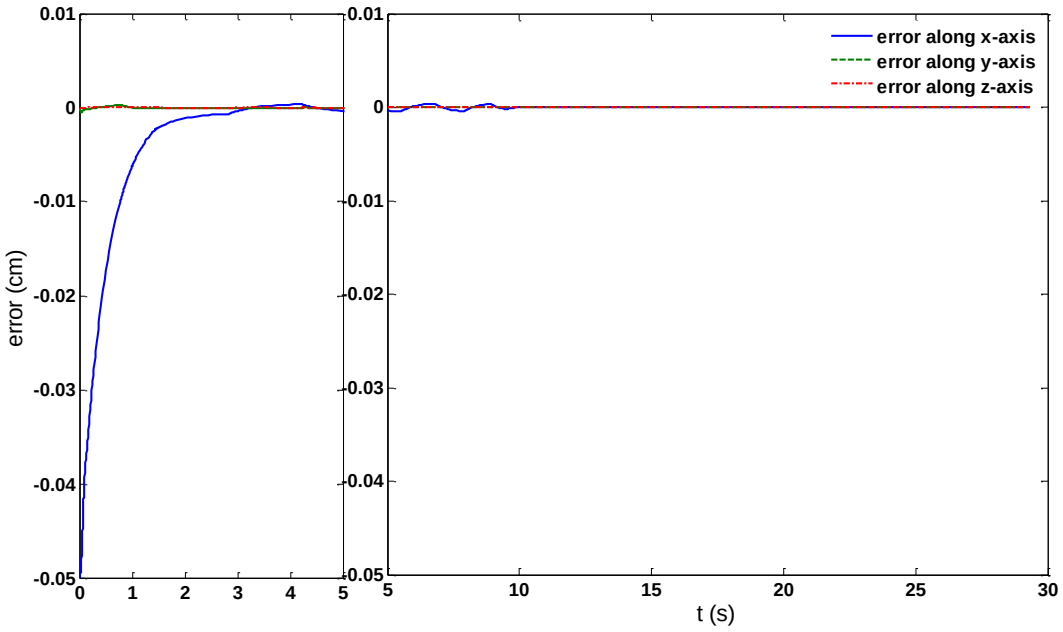

Figure 5-2: The error variation by time when the particle is following a noncircular path in a 2D plane.

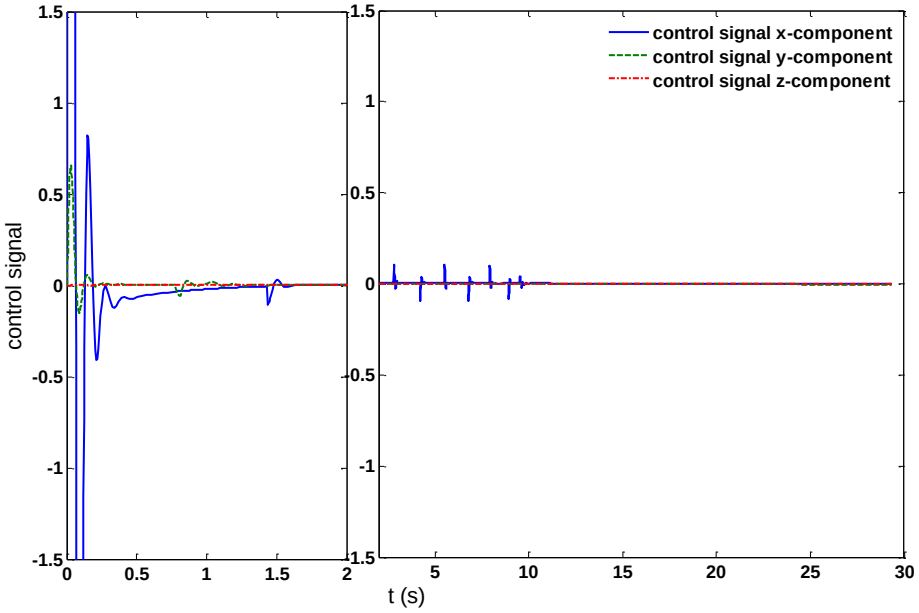

Figure 5-3: The control signal variation by time when the particle is following a noncircular path in a 2D plane.

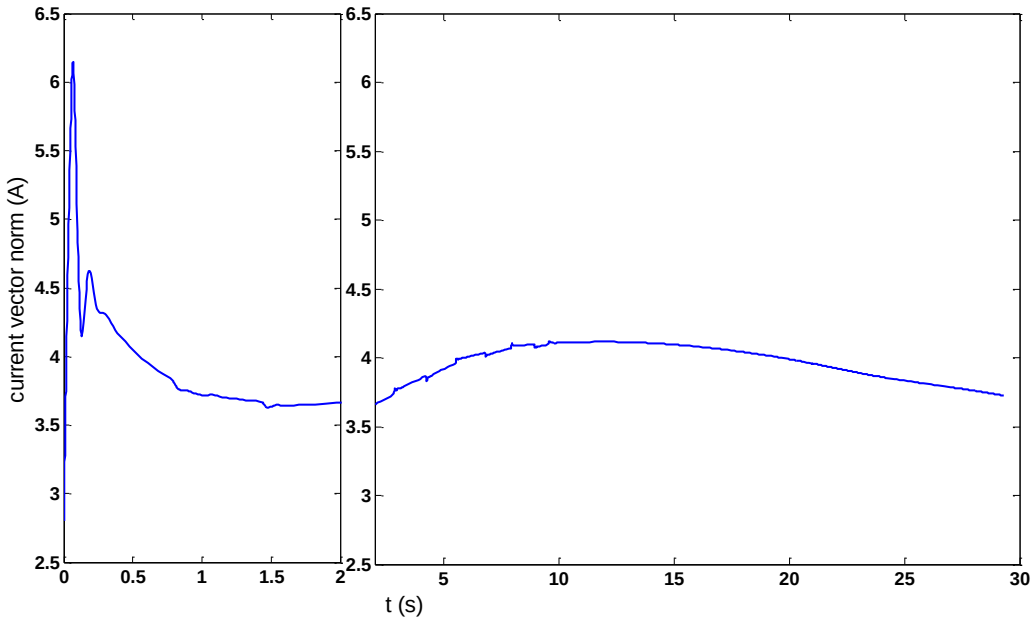

Figure 5-4: The current vector norm variation when the particle is following a noncircular path in a 2D plane.

Next, the same simulation is done for a circular path with radius 1 cm on the plane $x_1^3 = 0$ with the same velocity as the previous experiment. The initial condition is $X_1 = (1.05,0,0)\ \text{cm}, X_2 = (0,0.03,0)\ \text{cm/s}$. The simulation results, both errors and control signals, are depicted in Figure 5-5 and Figure 5-6 as well Figure 5-7 depicting the current norm. As it is observable, the errors die after a short period of time while the control signals also approach zero. Moreover, like the previous case, it can also be detected that there is no pattern of periodic changes in control signal. In fact, the coefficients in (5-23) can be updated by adaptation law, and the necessity of fixed frequencies is eliminated. Figure 5-7 shows the boundedness of current vector through the navigation process.

At this point, the simulation is repeated for the circular path of the same radius when the outputs are augmented with a white noise with the power spectral density of magnitude 0.0004. The simulation results show the fast drop in output errors as well as the bounded current vector (Figure 5-8, Figure 5-9). In other words, the system is robust to the measurement noises. On the other hand, the movement of the ferromagnetic particle near the working space center, the singularity region, is studied by decreasing the radius of the circular path. In this case the initial condition is $X_1 = (1,0,0)\ \text{cm}, X_2 = (0,0.03,0)\ \text{cm/s}$. The results are shown in Figure 5-10 and Figure 5-11. Similarly, the errors go to zero via bounded control signals.

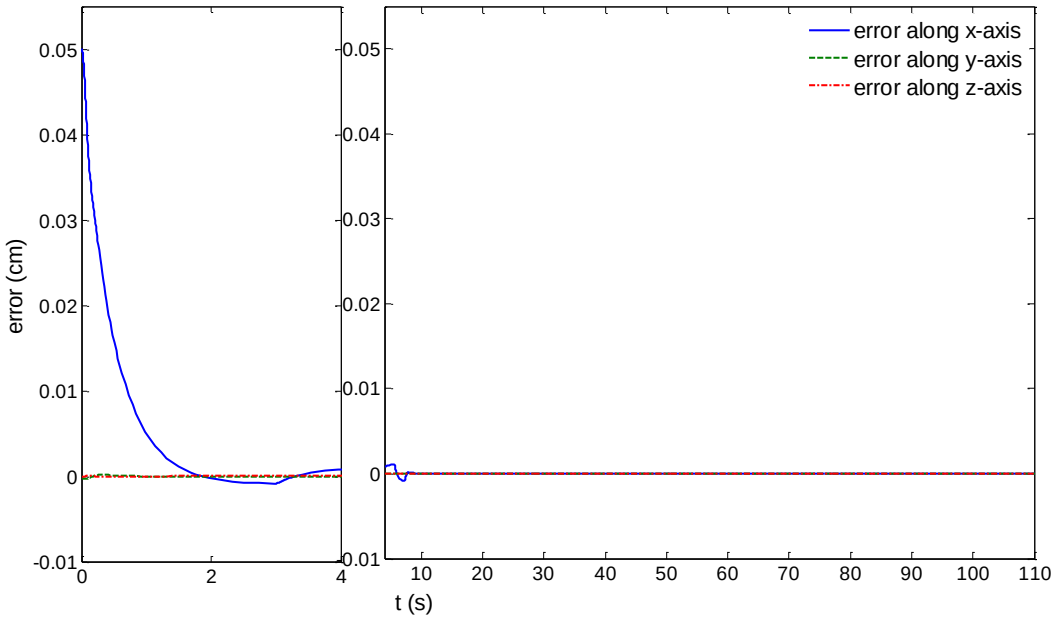

Figure 5-5: The error variation by time when the particle is following a circular path of radius 1 *cm* in a 2D plane.

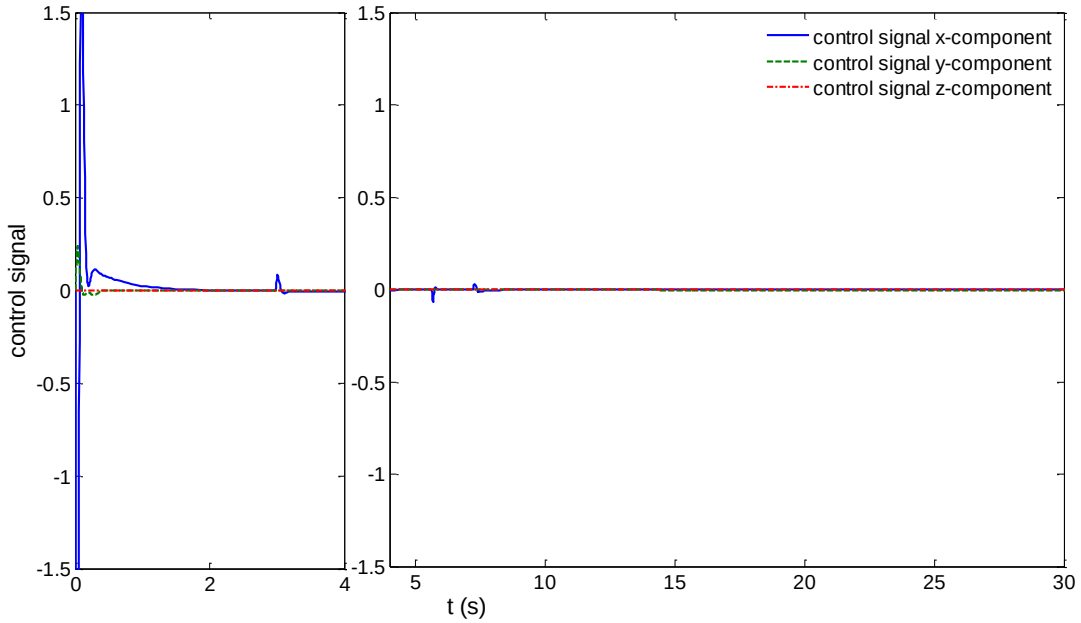

Figure 5-6: The control signal variation by time when the particle is following a circular path of radius 1 *cm* in a 2D plane.

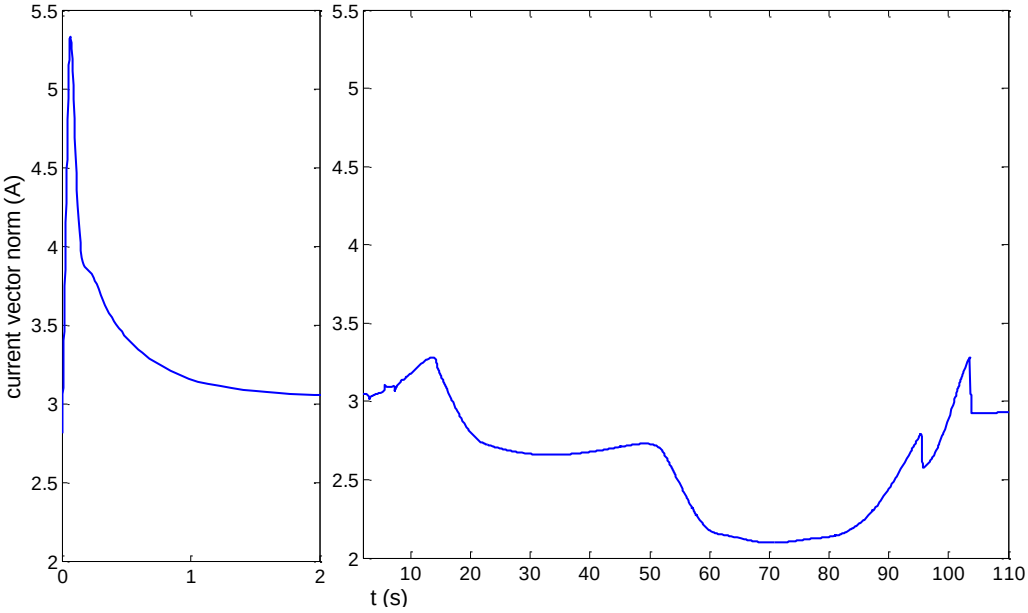

Figure 5-7: The current vector norm variation when the particle is following a circular path of radius 1 *cm* in a 2D plane.

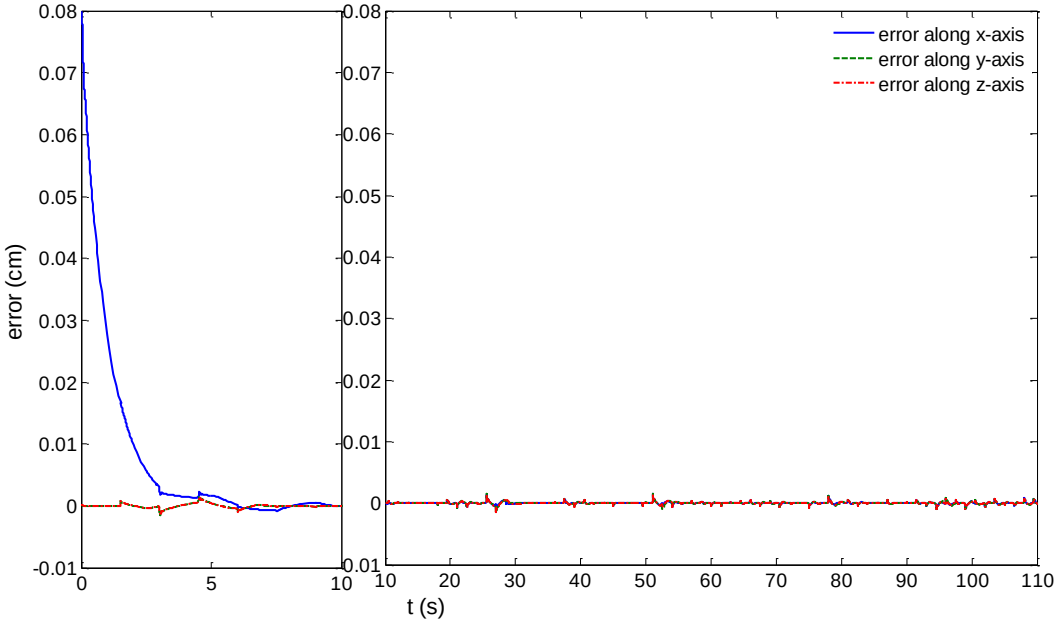

Figure 5-8: The control signal variation by time when the particle is following a circular path of radius 1 *cm* in a 2D plane and the system output is augmented with noise.

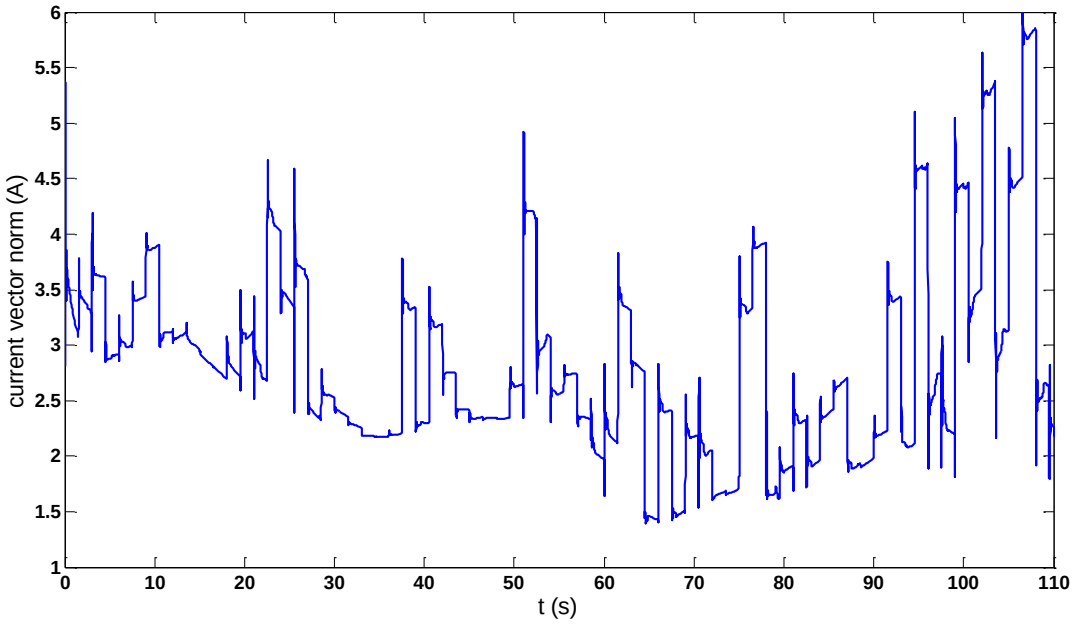

Figure 5-9: The current vector norm variation when the particle is following a circular path of radius 1 *cm* in a 2D plane and the system output is augmented with noise.

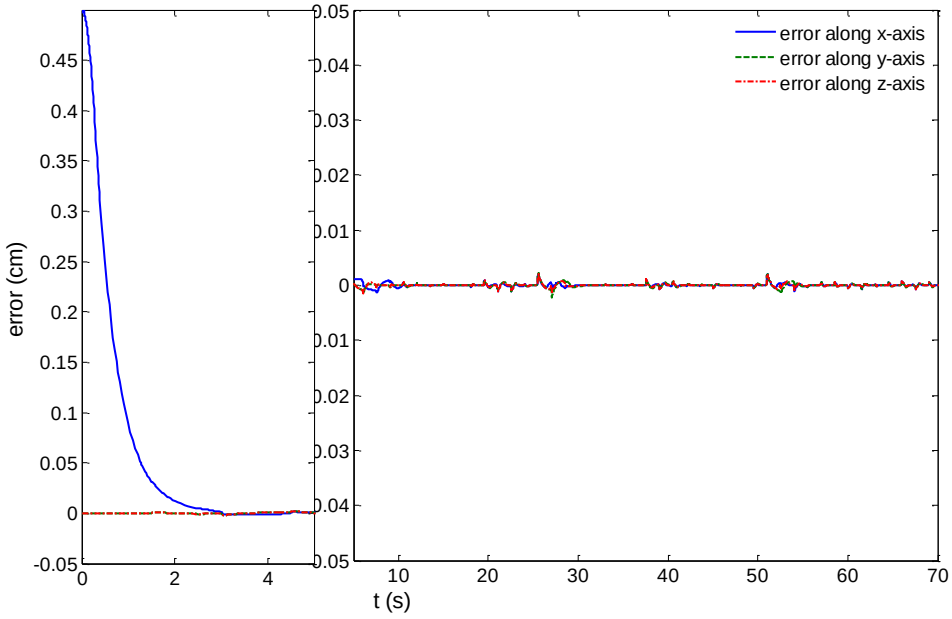

Figure 5-10: The control signal variation by time when the particle is following a circular path of radius 0. 5 *cm* in a 2D plane and the system output is augmented with noise.

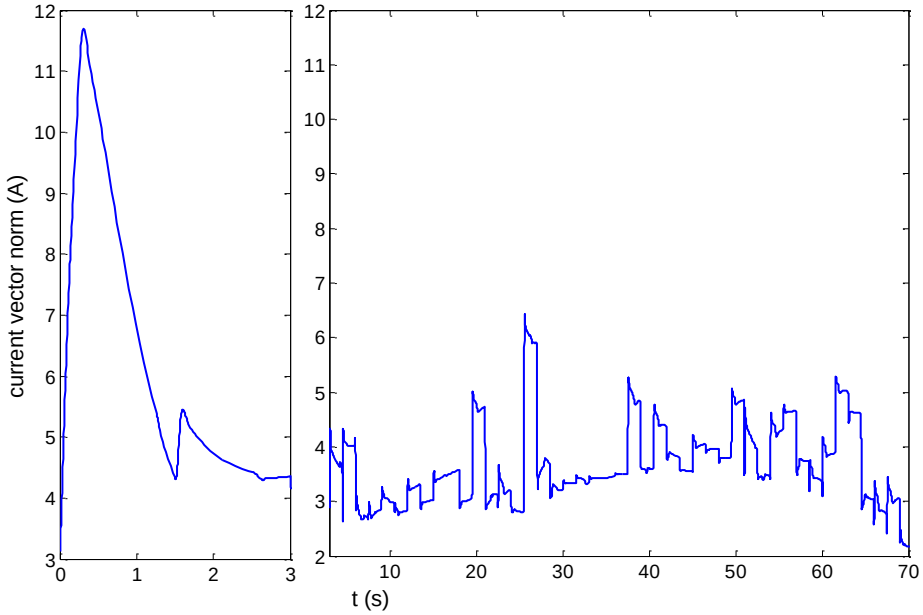

Figure 5-11: The current vector norm variation when the particle is following a circular path of radius $0.5\ cm$ in a 2D plane and the system output is augmented with noise.

In this chapter, the problem of robust output regulation without the requirement of complete knowledge of the exosystem frequencies was addressed. This limitation was overcome by utilizing the internal model-based controller augmented with an adaptation law. The proposed approach is then used to solve the trajectory tracking problem of a ferromagnetic particle via the electromagnetic setup. The basic assumption is that the zero dynamics of the system is asymptotically and locally exponentially stable around the reference trajectory. This assumption is not unreasonable due to the optimization effort on current vector norm. Nevertheless, the exponential stability of the system confirms the assumption on this dynamics.

Two different reference paths were examined, on which the movement is stimulated with a constant velocity. Additionally, the output vector is augmented with a white noise vector to investigate the regulation control robustness. In general, the designed regulation control provides robust tracking performance even if the reference control signals admit no periodicity. This can be explained by the fact that the exosystem does not have to be time invariant, and its parameters are updated through the adaptation law. On the other hand, the change of current vector norm, consumed energy, by time reveals the boundedness but not exponential convergence to zero. It is suggested that a wider period of time is required to detect the true convergence of zero dynamics states.

Chapter 6
Future Work

In the previous chapters, the modeling and control of micro-device navigation along a predefined path was introduced and the magnetic actuation utilized to produce micro-device movement. Subsequently, the magnetic actuation was divided into two general categories: actuation initiated by an MRI scanner and actuation initiated by a combination of electromagnets and coils. In this project, the latter structure was selected. The preliminary studies on 2D navigation of ferromagnetic particle were considered to introduce the general form of automatic navigation via an electromagnetic actuator and show the effect of the actuator structure. Accordingly, an augmented structure was proposed to improve the actuator operation, which was equipped with uniform coils. As well, the arrangement and number of electromagnets were optimized in the same chapter. In addition, the 3D movement of a ferromagnetic particle is efficiently controlled by a robust internal model based control scheme. Further studies, both experimentally and mathematically, on automatic navigation is required to improve the performance.

6.1 Design and workspace optimization

According to the simulation results, the axial magnetic field is the major component of a field vector induced by a single coil. As it moves from the coil's axis in either a parallel or transverse direction, the axial component loses its efficiency at the distance equal to coil's radius. As a result, the maximum working space dimension is constrained by the coils' radius. Moreover, the current values are limited because of the heat dissipation issue. To address this, an optimization algorithm was proposed in Chapter 4 to efficiently define the arrangement of the coils. It was observed that, while the augmented structure with uniform coils admits better performance on the concerned area, the working space should be expanded. In general, an elliptical surface is suggested to enclose the coils' top planes without any overlap between the two coils. The next step is to find an optimal value for the ellipsoid's parameters and the number of coils which provide the maximum working space.

In general, the real working space is a set of points defined as:

$$W = \{(\boldsymbol{X_1}, \boldsymbol{P}) : rank(\boldsymbol{M_W}) = r\} \quad 6\text{-}1$$

where r is the dimension of the magnetization vector augmented with the magnetic force vector. It is observed that, at some points, $\boldsymbol{X_1}$, there exist a number of magnetization vectors for which the matrix $\boldsymbol{M_W}$ is singular. Additionally, the condition of non-singularity is equivalent to the first condition of weak controllability of the system; thus, the system's reachable states are eliminated at the singular points. At this step, the structure is supposed to maximize the real working space while providing the second condition of controllability.

As well, fabrication constraints limit the optimization of working space since the coil dimensions are not exactly defined. The feasibility of the proposed structure also enters the calculation of maximum working space. In this project, three pairs of Helmholtz coils are added to the elliptical

structure, but the minimum available area is constrained by the Helmholtz coils' installation method. The alternative solution is to revise the optimization process when the minimum area is defined. In order to improve the structural design, some prototypes will be considered for the uniform coils' installation, followed by the introduced optimization algorithm. The final structure maximizes the working space and satisfies all constraints.

6.2 Control design

Forcing a micro-particle to move along a pre-defined path in a fluidic environment and utilizing the magnetic actuation is the main goal of this project. For control purposes, the first method that comes to mind is dividing the path into several operating points and transferring the system equilibrium point to these points. Then, the problem is finding a stabilizing control input around the new points. First, the state space equations are extended to achieve the following familiar form:

$$\dot{\boldsymbol{x}} = \boldsymbol{f}(\boldsymbol{x}) + \sum_{\boldsymbol{i}=\boldsymbol{1}}^{\boldsymbol{m}} \boldsymbol{g_i}(\boldsymbol{x})\boldsymbol{u_i}$$
$$\boldsymbol{y_i} = \boldsymbol{h_i}(\boldsymbol{x}) \quad \boldsymbol{1} \leq \boldsymbol{i} \leq \boldsymbol{p} \qquad \text{6-2}$$

wherein $\boldsymbol{x}$ is the state vector, $\boldsymbol{f}$, $\boldsymbol{g_i}$, $\boldsymbol{h_i}$ are continuous functions, $\boldsymbol{m}$ is number of inputs and $\boldsymbol{p}$ is number of outputs. At this level, if the control vector is designed to be zero at origin, the equation center, the equilibrium point, can be set by function $\boldsymbol{f}$ at the origin. Moreover, the new form is proved to be controllable some conditions; these conditions can be provided by optimizing the actuator design. The key problem is that the system is assumed to be minimum phase. The next step is to answer the question as to how this property can be assured, or whether or not it can be relaxed.

In practice, the automatic navigation can be performed by two different approaches: the path following control and the trajectory tracking control. These control methods are discriminated with respect to the assigned timing rule. In other words, the path following controller is addressed when no timing rule is regarded for the defined path, while the trajectory tracking controller deals with a timed path. In contrast to a trajectory tracking problem, being minimum phase is not a critical issue in the path following problem. In this project, the automatic navigation is converted to the form of a trajectory tracking problem in which the particle is assumed to follow a specific path with a constant velocity. Although the simulation results exhibit a good tracking performance, the method encounters some limitations.

First, the zero dynamics of electromagnetic system is not guaranteed to satisfy the minimum phase condition; however, the simulation results shows boundedness of the current vector, the state vector of zero dynamics. Since the zero dynamics is arranged to minimize the energy consumption, rather than linear constrain in control signal, a different constraint can be defined to provide required condition on zero dynamics. Therefore, new form of zero dynamics is not in control affine form necessitating different control design process. Moreover, the zero dynamics states are appeared in adaptation law but usually not measurable. Besides, the reference signals are not explicit for the states of zero dynamics. An estimate is obtained when the coefficient of this term is chosen relatively small enough. In fact, path following method may resolve these shortcomings.

One familiar method for designing a path following controller is to consider it as a set of stabilization problems. The set stabilization problem is a generalization form of the system stabilization around the equilibrium point. Like many methods in nonlinear control theory, the system is suggested to be transformed to a normal linear form by coordinate and state transformation. In this case, the system is decomposed into two cascade subsystems – driving and driven subsystems. In this context, the restriction of the driven subsystem to the invariant submanifold is called the tangential subsystem, while the driving subsystem is referred to as transversal subsystem. In normal form, the driving subsystem takes the linear controllable form and the set points are stabilized, which are transformed to be the origin of this subsystem.

At this level, the uncertainties are not considered in a mathematical equation when the nonlinear dynamics cancellation is applied. Furthermore, the sufficient and necessary conditions for the linearization process are locally defined. Subsequently, the sliding mode control is tried as the next step. In fact, this method deals with finding a co-dimension one hyper surface and is robust to the system uncertainties. After the required hyper-surface is figured out, the control problem task is to force the particle to move towards the surface, bringing around a discrete control commands. The sliding mode control is also a connection between the path-following and trajectory-tracking controllers.

6.3 Prototyping and experimental test set up

When the designed controller passes the simulation step, its applicability has to be tested through experimental results. The suggested 3D set up with the final improvement is considered to be prototyped. The set of appropriate electromagnets and coils matching the simulated environment have to be selected. Moreover, a structure is required on which the electromagnets and coils are mounted according to the configured arrangement. Measuring sensors are of great importance, since they define system observability and have to provide enough information. Indeed, a platform is required to transform the measurement data and control commands between the processor and the coils. Finally, a ferromagnetic sphere will be controlled to travel a predefined path. The comparison between experimental and simulation results presents the efficiency of a designed controller.

Bibliography

[1] C. Hu, M. Gao, Z. Chen, H. Zhang and S. Liu. "Magnetic analysis and simulations of a self-propelled capsule endoscope," *11th International Conference on Thermal, Mechanical & Multi-Physics Simulation, and Experiments in Microelectronics and Microsystems (EuroSimE),* pp. 1-5, 2010.

[2] A. Moglia, A. Menciassi, M. O. Schurr and P. Dario, "Wireless capsule endoscopy: from diagnostic devices to multipurpose robotic systems," *Biomedical Microdevices,* vol. 9, pp. 235-243, 2007.

[3] A. Uehara and K. Hoshina, "Capsule endoscope NORIKA system," *Minimally Invasive Therapy & Allied Technologies,* vol. 12, pp. 227-234, 2003.

[4] P. Dario, C. Stefanini and A. Menciassi, "Modeling and experiments on a legged microrobot locomoting in a tubular, compliant and slippery environment," *Experimental Robotics IX,* vol. 21, pp. 165-174, 2006.

[5] S. Park, J. Park, H. Park, S. Park, C. Jee, S. Park and B. Kim, "Multi-functional capsule endoscope for gastro-intestinal tract," *International Joint Conference, SICE-ICASE,* pp. 2090-2093, 2006.

[6] W. Zhang, Y. Chen and P. Huang, "Study on a spiral-type robot magnetically controlled in biotic tracts," *International Technology and Innovation Conference, ITIC,* pp. 2110-2115, 2006.

[7] N. Lee, N. Kamamichi, H. Li and K. Furuta, "Control system design and experimental verification of Capsubot," *International Conference on Intelligent Robots and Systems, IROS,* pp. 1927-1932, 2008.

[8] Y. Liu, H. Yu and T. Yang. "Analysis and Control of a Capsubot," *Proceedings of the 17th World Congress,* pp. 756-761, 2008.

[9] Y. Liu, H. Yu and L. Vladareanu, "An Iterative Learning Control Scheme for the Capsubot," *International Conference on Control, Proceedings of the UKACC,* 2008.

[10] N. Lee, N. Kamamichi, J. Ishikawa and K. Furuta, "Positioning control of a capsule robot using sliding mode control," *International Conference on Robotics and Biomimetics (ROBIO),* pp. 995-1000, 2009.

[11] D. Chen, C. Hu, L. Wang and M.Q.H. Meng, "The force model of wireless active actuation for capsule endoscope in the GI tract," *International Conference on Robotics and Biomimetics, ROBIO,* pp. 93-98, 2007.

[12] C. Hu, D. Chen, L. Wang and M.Q.H. Meng, "Control Strategy of Active Actuation System of Wireless Capsule Endoscope," *IEEE International Conference on Integration Technology ICIT'07.* pp. 1-6, 2007.

[13] G. Ciuti, P. Valdastri, A. Menciassi and P. Dario, "Robotic magnetic steering and locomotion of capsule endoscope for diagnostic and surgical endoluminal procedures," *Robotica,* vol. 28, pp. 199-207, 2010.

[14] F. Carpi and C. Pappone, "Magnetic maneuvering of endoscopic capsules by means of a robotic navigation system," *IEEE Transactions on Biomedical Engineering,* vol. 56, pp. 1482-1490, 2009.

[15] N. Baek, I. Sung and D. Kim, "Frictional resistance characteristics of a capsule inside the intestine for microendoscope design,' *Proceedings of the Institution of Mechanical Engineers, Part H: Journal of Engineering in Medicine,* vol. 218, pp. 193-201, 2004.

[16] X. Wang and M. Q. H. Meng, "An experimental study of resistant properties of the small intestine for an active capsule endoscope," *Proceedings of the Institution of Mechanical Engineers, Part H: Journal of Engineering in Medicine,* vol. 224, pp. 107-118, 2010.

[17] T. Mei, Y. Chen, G. Fu AND D. Kong, "Wireless drive and control of a swimming microrobot," *IEEE International Conference on Robotics and Automation, ICRA'02,* pp. 1131-1136, 2002.

[18] S. Guo, J. Sawamoto and Q. Pan, "A novel type of microrobot for biomedical application," *IEEE/RSJ International Conference on Intelligent Robots and Systems, IROS.* pp. 1047-1052, 2005.

[19] Q. Pan and S. Guo, "Development of the novel types of biomimetic microrobots driven by external magnetic field," *IEEE International Conference on Robotics and Biomimetics, ROBIO,* pp. 256-261, 2008.

[20] Y. Zhang and G. Liu, "Wireless swimming microrobot: Design, analysis, and experiments," *Journal of Dynamic Systems, Measurement, and Control,* vol. 131, pp. 011004, 2009.

[21] H. Li, J. Tan and M. Zhang, "Dynamics modeling and analysis of a swimming microrobot for controlled drug delivery," *IEEE Transactions on Automation Science and Engineering,* vol.6, pp. 220-227, 2009.

[22] B. Behkam and M. Sitti, "E. coli inspired propulsion for swimming microrobots," *Proceedings of IMECE International Mechanical Engineering Conference,* pp. 13-19, 2004.

[23] B. Behkam and M. Sitti, "Modeling and testing of a biomimetic flagellar propulsion method for microscale biomedical swimming robots," *IEEE/ASME International Conference on Advanced Intelligent Mechatronics,* pp. 37-42, 2005.

[24] M. Zhang, T.J. Tarn and N. Xi, "Micro/nano-devices for controlled drug delivery," *IEEE International Conference on Robotics and Automation ICRA'04,* pp. 2068-2073, 2004.

[25] J. B. Mathieu, G. Beaudoin and S. Martel, "Method of propulsion of a ferromagnetic core in the cardiovascular system through magnetic gradients generated by an MRI system," *IEEE Transactions on Biomedical Engineering,* vol. 53, pp. 292-299, 2006.

[26] S. Martel, M. Mohammadi and O. Felfoul, "Flagellated magnetotactic bacteria as controlled MRI-trackable propulsion and steering systems for medical nanorobots operating in the human microvasculature," *The International journal of robotics research,* vol. 28, pp. 571, 2009.

[27] J.B. Mathieu and S. Martel, "In vivo validation of a propulsion method for untethered medical microrobots using a clinical magnetic resonance imaging system," *IEEE/RSJ International Conference on Intelligent Robots and Systems, IROS,* pp. 502-508, 2007.

[28] S. Martel, J. B. Mathieu, O. Felfoul, A. Chanu, E. Aboussouan, S. Tamaz, P. Pouponneau, G. Beaudoin, G. Soulez and M. Mankiewicz, "Automatic navigation of an untethered device in the artery of a living animal using a conventional clinical magnetic resonance imaging system," *Applied Physics Letters,* vol. 90, pp. 114105-114107, 2007.

[29] S. Tamaz and S. Martel, "Impact of the MRI-based navigation system constraints on the step response using a PID controller," *IEEE 27th Annual International Conference of the Engineering in Medicine and Biology Society, EMBS'05,* pp. 5073-5076, 2005.

[30] S. Tamaz, R. Gourdeau and S. Martel, "Bidimensional MRI-based navigation system using a PID controller," *IEEE 28th Annual International Conference of the Engineering in Medicine and Biology Society, EMBS'06,* pp. 4424-4427, 2008.

[31] S. Tamaz, R. Gourdeau, A. Chanu, J. B. Mathieu and S. Martel, 'Real-time MRI-based control of a ferromagnetic core for endovascular navigation," *IEEE Transactions on Biomedical Engineering.* vol. 55, pp. 1854-1863, 2008.

[32] L. Arcese, M. Fruchard and A. Ferreira, "Nonlinear modeling and robust controller-observer for a magnetic microrobot in a fluidic environment using MRI gradients," *IEEE/RSJ International Conference on Intelligent Robots and Systems, IROS.* pp. 534-539, 2009.

[33] A. Komaee and B. Shapiro, "Steering a ferromagnetic particle by magnetic feedback control: Algorithm design and validation," *American Control Conference, ACC,* pp. 6543-6548, 2010.

[34] A. Chanu, O. Felfoul, G. Beaudoin and S. Martel, "Adapting the clinical MRI software environment for real-time navigation of an endovascular untethered ferromagnetic bead for future endovascular interventions," *Magnetic Resonance in Medicine,* vol. 59, pp. 1287-1297, 2008.

[35] E. Shameli, M. B. Khamesee and J. P. Huissoon, "Real-time control of a magnetic levitation device based on instantaneous modeling of magnetic field," *Mechatronics,* vol.18, pp. 536-544, 2008.

[36] V. Labinac, N. Erceg and D. Kotnik-Karuza, "Magnetic field of a cylindrical coil," *American* Journal of Physics, vol.74, pp. 621-627, 2006.

[37] E. du Tremolet de Lacheisserie, D. Gignoux, M. Schlenker, Magnetism: Fundamentals. United States of America: Springer Verlag, 2005, pp. 32-36.

[38] R. Probst, J. Lin, A. Komaee, A. Nacev, Z. Cummins, B. Shapiro, "Planar steering of a single ferrofluid drop by optimal minimum power dynamic feedback control of four electromagnets at a distance," *Journal of Magnetism and Magnetic Material,* vol. 323, pp. 885-896, 2010.

[39] R. G. McNeil, R. C. Ritter, B. Wang, M. A. Lawson, G. T. Gillies, et al. "Functional design features and initial performance characteristics of a magnetic-implant guidance system for stereotactic neurosurgery", *IEEE transactions on biomedical engineering,* vol. 42, pp. 793-801, 1995.

[40] R. G. McNeil, R. C. Ritter, B. Wang, M. A. Lawson, G. T. Gillies, et al. "Characteristics of an improved magnetic-implant guidance system," *IEEE transactions on biomedical engineering,* vol.42, pp. 802-808, 1995.

[41] D. C. Meeker, E. H. Maslen, R. C. Ritter, and F. M. Creighton, "Optimal realization of arbitrary forces in a magnetic stereotaxis system," *IEEE transactions on magnetics*, vol. 32, pp. 320-328, 1996.

[42] A. Serrani, A. Isidori, and A. Marconi, "Semiglobal nonlinear output regulation with adaptive internal model", *IEEE Transaction on Automatic Control,* vol. 46, pp.1178 - 1194, 2001.

[43] Davison, E.J., "The robust control of a servomechanism problem for linear time-invariant multivariable systems", *IEEE Transaction on Automatic Control,* vol. 21, no. 1, pp. 25-34, 1976.

[44] B. A. Francis, "The linear multivariable regulator problem," *IEEE Conference on Decision and Control including the 15th Symposium on Adaptive Processes*, vol.15, pp.873-878, 1976.

[45] B. A. Francis and W. M. Wonham," The internal model principle of control theory," *Automatica,* vol. 12, pp. 457–465, 1976.

[46] B. A. Francis and W. M. Wonham, "The internal model principle for linear multivariable regulators," *Journal of Applied Mathematics and Optimization*, vol. 2, pp. 170-194, 1975.

[47] J. S. A. Hepburn and W. M. Wonham, "Error feedback and internal models on differentiable manifolds," *IEEE Transaction on Automatic Control,* vol. 29, pp. 397-403, 1984.

[48] V. Anantharam and C. A. Desoer, "Tracking and disturbance rejection of MIMO nonlinear systems with a PI or PS controller," *IEEE Transactions on Automatic Control*, vol. 24, pp. 1367–1468, 1985.

[49] J. Huang and W. J. Rugh, "On a nonlinear multivariable servomechanism problem," *Automatica*, vol. 26, no.6, pp. 963 -972, 1990.

[50] A. Isidori, C. Byrnes, "Output regulation of nonlinear systems," *IEEE Transaction on Automatic Control*, vol. 35, pp. 131–140, 1990.

[51] C. I. Byrnes, F. Delli Priscoli, A. Isidori, and W. Kang, "Structurally stable output regulation of nonlinear systems," *Automatica*, vol. 33, pp.369 - 385, 1997.

[52] C. I. Byrnes and A. Isidori, "Limit sets, zero dynamics and internal models in the problem of nonlinear output regulation", *IEEE Transaction on Automatic Control*, vol. 48, pp. 1712 - 1723, 2003.

[53] A. R. Teel and L. Praly, "Tools for semi-global stabilization by partial state and output feedback," *SIAM Journal of Control and Optimization*, vol. 33, no. 5, pp.1443 -1488, 1995.

[54] W. M. Haddad and V. Chellaboina, Nonlinear dynamical system and control: a Lyapunov-based approach, Princeton University Press, 2008.

[55] F. Esfandiari and H. K. Khalil, "Output feedback stabilization of fully linearizable systems," *International Journal of Control*, vol. 56, pp. 1007–1037, 1992.

[56] A. J. Laub, M. T. Heath, C. C. Paige, and R. C. Ward, "Computation of system balancing transformations and other applications of simultaneous diagonalization algorithms," *IEEE Transaction on Automatic Control*, vol. 32, pp. 115–122, 1987.

[57] E. P. Furlani, S. Reznik, and W. Jansen, "A three-dimensional field solution for bipolar cylinders," *IEEE transaction on Magnetism*, vol.30, no. 5, pp. 2916-2919, 1994.

[58] S. Fenster, "Torus topology of the static current loop field", *American Journal of Physics*, vol. 43, no. 8, pp. 683-688, 1975.

[59] M. W. Coffey, "Theory for coil impedance of a conducting half space: Analytical results for eddy current analysis," Journal of Applied Physics, vol. 89, no. 4, pp. 2473-2481, 2001.

[60] C. Snow, "Magnetic fields of cylindrical coils and annular coils," Natl. Bur. Stand., ser. Applied Mathematics, vol. 38, pp. 1-29, 1953.

[61] H. S. Cohl, J. E. Tohline, and A. R. P. Rau, “Developments in determining the gravitational potential using toroidal functions,” *Astronomische Nachrichten,* vol. 321, pp. 363-372, 2000.

[62] M. Andrews, “Alternative separation of Laplace’s equation in toroidal coordinates and its application to electrostatics,” *Journal of Electrostatics*, vol. 64, pp. 664-672, 2006.

[63] H. S. Cohl, A. R. P. Rau, J. E. Tohline, D. A. Browne, J. E. Cazes, and E. I. Barnes, “Useful alternative to the multipole expansion of 1/r potentials,” *Physical Review A,* vol. 64, pp. 052509-1-5, 2001.

[64] H. S. Cohl, J. E. Tohline, “ A compact cylindrical green’s function expansion for the solution of potential problems,” *Astrophysical Journal*, vol. 572, pp. 86-101, Dec. 1999.

[65] J. Selvaggi, S. Salon, O. Kwon, and M. V. K. Chari, “Calculating the external magnetic field from permanent magnets in permanent magnet motors,” *IEEE Transaction on Magnetism*, vol. 40, no. 5, pp. 3278-3285, 2004.

[66] J. Selvaggi, “Multipole analysis of circular cylindrical magnetic system,” *Ph.D. dissertation, Rensseler Polytechnic*, Troy, NY, 2005.

[67] J. Selvaggi, S. Salon, O. Kwon, and M. V. K. Chari, “A general method for calculating the external magnetic field from a cylindrical magnetic source using toroidal functions,” presented at the Electric Machines Technology Symposium, Philadelphia, PA, May 22-24, 2006.

[68] Selvaggi, J. P., S. Salon, O. M. Kwon, and M. V. K. Chari, "Computation of the three-dimensional magnetic field from solid permanent-magnet bipolar cylinders by employing toroidal harmonics," *IEEE Transaction on Magnetism*, vol. 43, no. 10, pp. 3833-3839, 2007.

[69] A. Isidori, Nonlinear control systems I. London: Springer Verlag, 1999.

[70] R. Hermann and A. J. Krener, “Nonlinear controllability and observability”, *IEEE Transaction on Automatic Control*, vol.22, no. 5, pp. 728-740, 1977.

Appendix

In the calculation process of a magnetic field, it is assumed that the superposition law is applicable. In the existence of soft material, the magnetic field equation can be written as the following form:

$$\boldsymbol{B} = \frac{\mu_0}{4\pi}\boldsymbol{\nabla} \times \left(\iiint \frac{\boldsymbol{rot}(\boldsymbol{M}) + \boldsymbol{i}}{r} dv - \iint \frac{\hat{\boldsymbol{n}} \times \boldsymbol{M}}{r} ds \right) \quad \text{A-1}$$

$$\boldsymbol{B} = \boldsymbol{\mu_0 \mu}(\boldsymbol{H})\boldsymbol{H}$$

$$\boldsymbol{M} = \frac{\chi(\boldsymbol{H})}{\mu_0 \mu(\boldsymbol{H})}\boldsymbol{B} \quad \text{A-2}$$

Equation (A-1) reveals that the magnetic field equation is an integral equation and is nonlinear if (A-2) represents $\boldsymbol{M}$ as a nonlinear function of $\boldsymbol{B}$. In special cases, the magnetization vector is a linear function of a magnetic vector field, making (A-1) a linear integral equation. Therefore, the condition of the superposition law is satisfied. Although the magnetization vector of ferromagnetic material is a nonlinear function of ampere turn density vector, $\boldsymbol{H}$, it is estimated by a linear function. This estimation is valid when the magnetic field is less than the saturation value of the ferromagnetic material.

In this project, the electromagnets are equipped with iron core with saturation magnetic field between 1.5 T to 2T. The superposition law is shown experimentally for a horizontal structure. The structure is composed of four horizontal electromagnets whose centers are located around a circle of radius 2.5 cm. The electromagnets' dimensions are: inner radius, a_1=1 cm; outer radius, a_2=2 cm; and length 4 cm. In this experiment, the field x-component is measured along the x-axis for two different current values. In each experiment, all of the active electromagnets carry the same currents. The experimental set up is shown in Figure A- 1and the results are depicted in Figure A- 2 - Figure A-7.

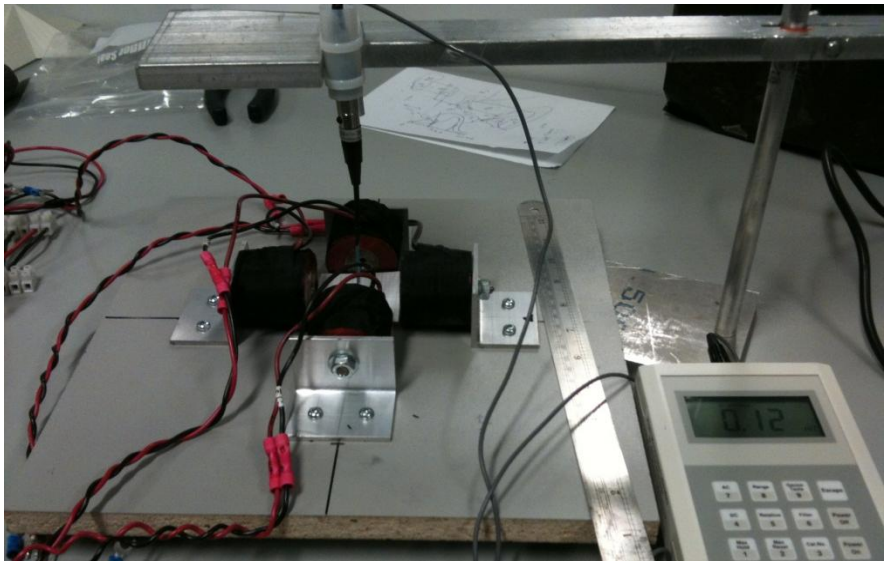

Figure A- 1: Experimental set of magnetic field measurement.

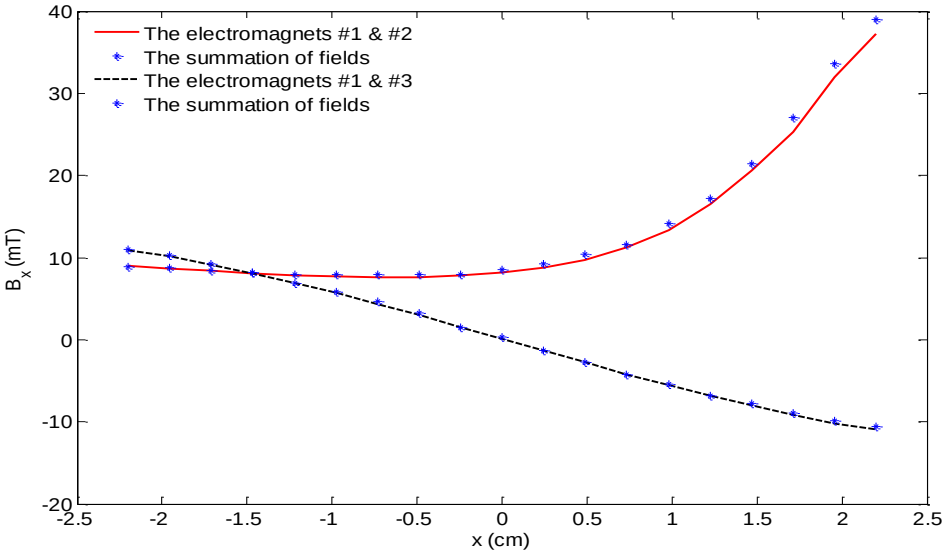

Figure A- 2: Magnetic field of a horizontal structure for two active electromagnets carrying current 1 (*A*) along the x-axis.

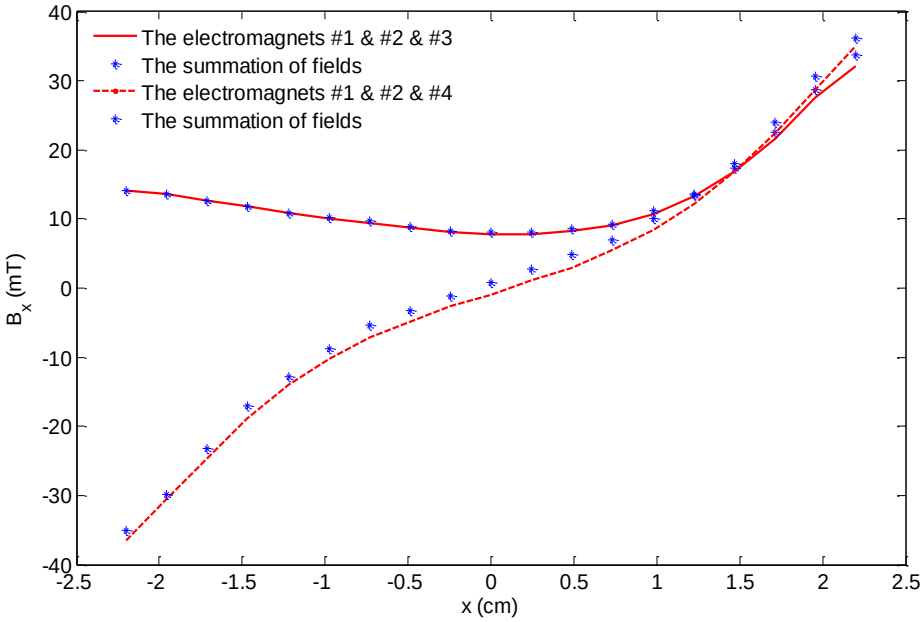

Figure A- 3: Magnetic field of a horizontal structure for three active electromagnets carrying current 1 (*A*) along the x-axis.

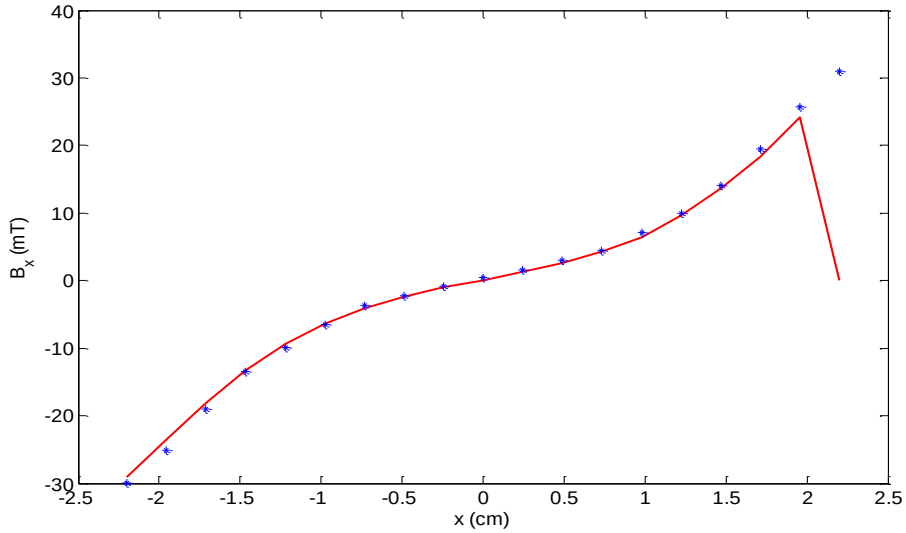

Figure A- 4 : Magnetic field of a horizontal structure for four active electromagnets carrying current 1 (*A*) along the x-axis.

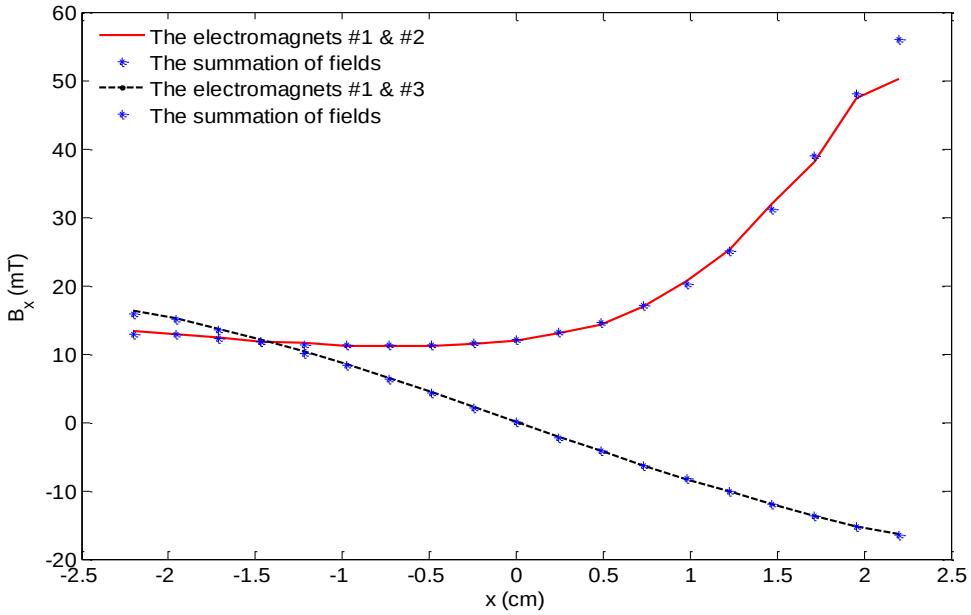

Figure A- 5: Magnetic field of a horizontal structure for two active electromagnets carrying current 1.5 (*A*) along the x-axis.

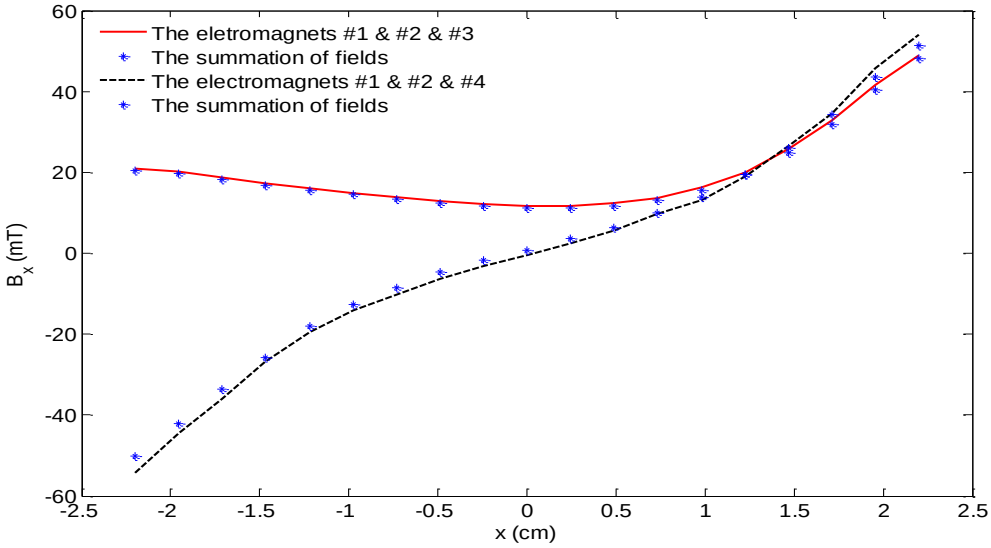

Figure A- 6: Magnetic field of a horizontal structure for three active electromagnets carrying current 1.5 (*A*) along the x-axis.

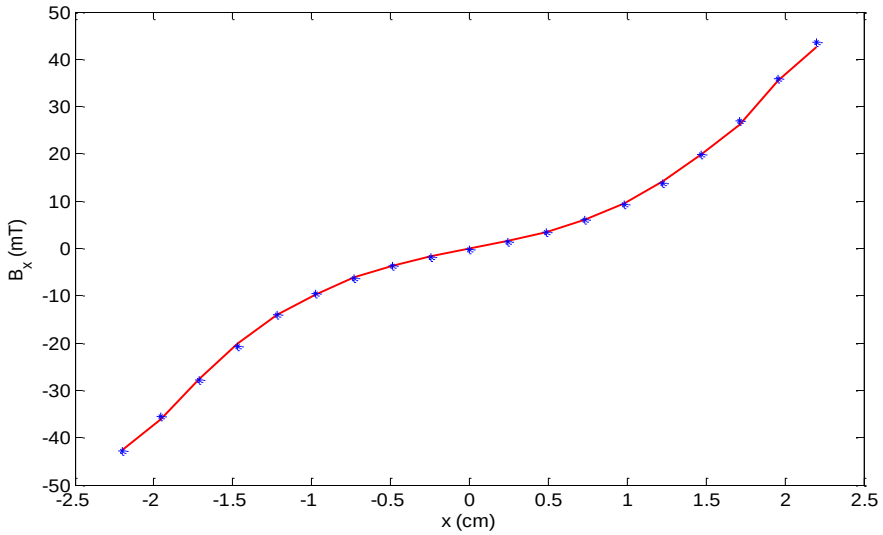

Figure A-7: Magnetic field of a horizontal structure for four active electromagnets carrying current 1.5 (*A*) along the x-axis.

The experimental results confirm the validity of the superposition law when the current has not surpassed the saturation level. However, the magnetic field of an electromagnet drops and loses its effectiveness at distances greater than the electromagnet's outer radius. When the effect of each electromagnet's field on the other cores is ignored, each integral term in (A-1) can be divided into four integral terms. In other words, the integral over the whole area is characterized as the summation

of four integrals over each electromagnet area. Thus, the total field can be calculated by superposing the field of active electromagnets.